AFRL-AFOSR-UK-TR-2014-0051

Total Internal Reflection Ultrasonic Sensor for Detection of Subsurface Flaws: Research into Underlying Physics

Oleksandr Yurchenko

SCIENCE AND TECHNOLOGY CENTER IN UKRAINE
METALISTIV 7A
KYIV, 03057 UKRAINE

Taras Shevchenko National University of Kyiv
Department of Quantum Radiophysics
64, Volodymyrska Street
Kyiv, 01033 Ukraine

EOARD STCU-P475/Grant 12-2018

Report Date: November 2014

Final Report from 1 September 2012 to 31 August 2014

Air Force Research Laboratory
Air Force Office of Scientific Research
European Office of Aerospace Research and Development
Unit 4515, APO AE 09421-4515

REPORT DOCUMENTATION PAGE

Form Approved OMB No. 0704-0188

1. REPORT DATE *(DD-MM-YYYY)*
24 November 2014

2. REPORT TYPE
Final Report

3. DATES COVERED *(From – To)*
1 September 2012 – 31 August 2014

4. TITLE AND SUBTITLE

Total Internal Reflection Ultrasonic Sensor for Detection of Subsurface Flaws: Research into Underlying Physics

5a. CONTRACT NUMBER
STCU-P475

5b. GRANT NUMBER
Grant 12-2018

5c. PROGRAM ELEMENT NUMBER
61102F

6. AUTHOR(S)

Oleksandr Yurchenko

5d. PROJECT NUMBER

5d. TASK NUMBER

5e. WORK UNIT NUMBER

7. PERFORMING ORGANIZATION NAME(S) AND ADDRESS(ES)
SCIENCE AND TECHNOLOGY CENTER IN UKRAINE
METALISTIV 7A
KYIV, 03057 UKRAINE

Taras Shevchenko National University of Kyiv
Department of Quantum Radiophysics
64, Volodymyrska Street
Kyiv, 01033 Ukraine

8. PERFORMING ORGANIZATION REPORT NUMBER

N/A

9. SPONSORING/MONITORING AGENCY NAME(S) AND ADDRESS(ES)

EOARD
Unit 4515
APO AE 09421-4515

10. SPONSOR/MONITOR'S ACRONYM(S)

AFRL/AFOSR/IOE (EOARD)

11. SPONSOR/MONITOR'S REPORT NUMBER(S)

AFRL-AFOSR-UK-TR-2014-0051

12. DISTRIBUTION/AVAILABILITY STATEMENT

Distribution A: Approved for public release; distribution is unlimited.

13. SUPPLEMENTARY NOTES

14. ABSTRACT

The report presents results of the research aimed at advancing the understanding of underlying physics and operational functionality of the Total Internal Reflection Ultrasonic Sensor (TIRUS). Propagation and reflection of ultrasonic beams in its body, which is a strongly anisotropic TeO_2 crystal, were studied theoretically and experimentally. Its insertion losses that are operational characteristics of the sensor were measured using continuous wave and time-gated (pulse) techniques. It has been shown that a probable reason for their high value is the transduction loss of the transducer but not conversion of a probing shear wave into other acoustic modes. The sensor capability of sensing subsurface flaws has been proved when the sensor was in direct contact with a tested specimen. In the case of a couplant between those, its operational capability has to be proved yet. In optical experiments, the structure of ultrasonic beams has been observed for the first time from the direction forbidden for acousto-optic interaction. Two effects were discovered that have apparently never been observed before, conversion of the shear horizontal wave into a longitudinal one on its normal reflection from a free flat surface and a displacement of an ultrasonic beam on its oblique reflection from such one.

15. SUBJECT TERMS

EOARD, non-destructive evaluation, total internal reflection, ultrasonics, NDE, non-destructive testing

16. SECURITY CLASSIFICATION OF:			**17. LIMITATION OF ABSTRACT**	**18, NUMBER OF PAGES**	**19a. NAME OF RESPONSIBLE PERSON**
a. REPORT	**b. ABSTRACT**	**c. THIS PAGE**			Matthew Snyder
UNCLAS	UNCLAS	UNCLAS	SAR	109	**19b. TELEPHONE NUMBER** *(Include area code)* +44 (0)1895 616420

Partner Project STCU_P475-EOARD_12RSW018

Total Internal Reflection Ultrasonic Sensor for Detection of Subsurface Flaws: Research into Underlying Physics

Operative commencement date: Sept. 01, 2012

Year End Date: August 31, 2014

FINAL TECHNICAL REPORT

Research Institution: Taras Shevchenko National University of Kyiv

Project Manager: Oleksandr (Alexander) Yurchenko

Department of Quantum Radiophysics

Kyiv 2014

Authors

(sections written are given in parentheses)

Alexander Yurchenko (1, 2.1, 2.2, 3, 5, 6.1, 6.2, 7.1, 7.2, 8, 11, Summary, Introduction, Conclusions)

Sergiy Kolyenov (8.2.1, 10, Appendix A)

Yuriy Pilgun (8.2.1, 9, Appendix A)

Galyna Pogorielova (2.3, 2.4)

Oleksandr Polishko (8)

Eugene Smirnov (4, 6.3, 7.3, 8.2, Appendix A)

s

Table of Contents

List of Abbreviations and Acronyms

AOM	acousto-optic modulator
BNC	a type of RF bayonet connector
CCD	charge-coupled device
CW	continuous wave
DFT	discrete Fourier transform
EDC	energy deviation coefficient
FDTD	finite-difference time-domain
FEM	finite element method
NDE	nondestructive evaluation
NDT	nondestructive testing
PC	personal computer
PCA	Principal Component Analysis
QL	quasi-longitudinal (wave)
QS	quasi-shear (wave)
QSF	quasi-shear fast (wave)
RF	radio frequency
RSSI	received signal strength indicator
SH	shear horizontal (wave)
SSW	slow shear wave
TG	time-gated
TIRUS	Total Internal Reflection Ultrasonic Sensor
UDL	ultrasonic delay line
UUT	unit under test
VSWR	Voltage Standing Wave Ratio

List of the Most Common Symbols

f	frequency
IL	insertion loss
IL_{TG}	time gated measured insertion losses
p_{31}, p_{32}, p_{34}, p_{35}	photoelastic constants
T	transfer function
T_{TG}	time-gated transfer function
Uj1, Uj2	Loss samples
Uj3, Uj4, Ug2, Ug2_2	TIRUS samples
ϕ	phase of the transfer function
ϕ_{TG}	phase of the time-gated transfer function
σ	standard deviation

List of Figures

Summary

The report presents results of the research aimed at advancing the understanding of underlying physics and operational functionality of the Total Internal Reflection Ultrasonic Sensor (TIRUS), a novel device for detection of subsurface flaws. Because of the complex character of the research, a few groups of results are reported obtained with different techniques and approaches. One group includes experimental results of visualization of ultrasonic beams in the sensor body, the TeO_2 crystal, and results of studies of the sensor functional features. Another group is presented by a calculation technique developed to simulate 3D distribution of the sound field in the crystal and by a novel approach developed for processing data obtained from an unstable output of the sensor.

In the experiments, the TIRUS capability of sensing *subsurface* flaws has been proved when it is in direct contact with a tested specimen. Its operational capability in the case of a couplant between those has to be proved yet. The TIRUS insertion losses that are its operational characteristics were measured using continuous wave and time-gated (pulse) techniques. It has been shown that a probable reason for their high value is the transduction loss of the transducer but not conversion of a probing shear wave into other acoustic modes in the sensor body. It has also been established that imperfection of the TIRUS design leads to appearance of spurious signals at the TIRUS output and spurious longitudinal waves in its body. Temperature controllable studies of the TIRUS have proved that instability of its output is connected exclusively with temperature influences.

The developed optical setup and experimental technique has allowed ultrasonic beams to be *visualized for the first time while observed from the direction forbidden for acousto-optic interaction*. As a result, reflection in the plane $(1\bar{1}0)$ of the slow shear waves *polarized along the illuminating light beam* was observed and studied. No conversion of these waves, which are of the shear horizontal wave type, into other acoustic modes on their reflection from an inclined surface of the crystal was observed. At the same time, two effects were discovered that have apparently never been observed before, *conversion of the shear horizontal wave into a longitudinal one on its normal reflection from the free flat surface* of the crystal and a *displacement of an ultrasonic beam on its oblique reflection from the free flat surface*. For the time being, both these effects are inexplicable and require further studies.

The calculation technique developed for simulation of 3D structure of ultrasonic beams radiated by a rectangular shear wave transducer into an anisotropic medium has been of help in the study of propagation and reflection of shear waves in the sensor body. It was used for computation of diffraction losses of a probing wave across its polygonal path in the crystal. In further researches, it is to be a useful instrument in the study of inexplicable effects discovered in the optical visualization experiments.

A digital signal processing technique based on the combined use of the principal component analysis and the discrete Fourier transform has been developed for extraction of essential features of the sensor from its unstable output. An estimator built using the developed technique has shown rather high probability of accurate estimation of the presence of subsurface defects in the tested specimens.

Summarizing, it is worth noting that two above mentioned findings, conversion of the shear horizontal wave into a longitudinal one and the displacement of an ultrasonic beam are of great importance and their further studies should result in broadening our knowledge of reflection of ultrasonic waves in strongly anisotropic

media. Experiments on detecting subsurface defects using couplants should be continued too to resolve a contradiction in the results obtained.

Main results of the research were presented at four international conferences numbered [2, 15, 16, 17] in the list of references.

Introduction

This report is a result of a two-year study of the Total Internal Reflection Ultrasonic Sensor (TIRUS), a device specially aimed at detecting subsurface flaws in a tested specimen based on the frustrated total internal reflection of bulk ultrasonic waves in the sensor body. The study includes (1) investigations of experimental samples of the sensor, (2) building of a model for calculation ultrasonic fields in it and (3) development of a technique for post-processing of its output signals. Thus, this is a complex research using different techniques and approaches, which produce very different types of results. Therefore, the report is organized as a set of numbered virtually independent sections 2-10 that can be read separately but contain interrelated results and cross-references between them. These sections are written by different participants of the project listed in the list of authors, namely by those who mainly dealt with a corresponding task solved. Two sections, section 1 and section 11 are written specially to give an outline of the tasks solved in the project and to discuss results obtained briefly. Reading these two sections is enough to get an idea of what the research is about as a whole and what results are obtained; references given in section 11 to the items of specific sections 2-10 enable the results described in detail in these sections to be found easily.

A short list of the most common symbols used repeatedly across the report is placed in its beginning. Two sections, No. 9 and No.10, dealing with building of theoretical models and development of calculation techniques have their own long lists of symbols used exclusively in these sections.

1 The Project Tasks and Approaches to Their Solution

1.1 Tasks to Be Solved

In the previous research [1], a Total Internal Reflection Ultrasonic Sensor (TIRUS), a novel device for detection of subsurface flaws, was developed and its feasibility was proved. The sensor was designed on the premise that ultrasonic waves propagating and reflecting in the sensor body made of a TeO_2 single crystal behave in a simple manner of plane waves.

In the fabricated experimental sample of the TIRUS a transducer of the sensor emitted a slow shear wave (SSW) into the [110] direction of the TeO_2 crystal. The sensor design was such that the displacement vector of the SSW lay in the planes of reflecting surfaces of the crystal, that is, it was a shear horizontal (SH) wave with respect to these planes. It was assumed that with such a design no other waves should exist in the crystal except those polarized as the SSW.

Optical visualization of acoustic modes in the crystal showed, however, that not only the assumed waves existed but also waves of other types, quasi-longitudinal (QL) and quasi shear fast (QSF) did exist. This fact is illustrated in Fig. 1.1.1 taken from [1].

There was also discovered that the insertion loss of the TIRUS, which was an operational characteristic of

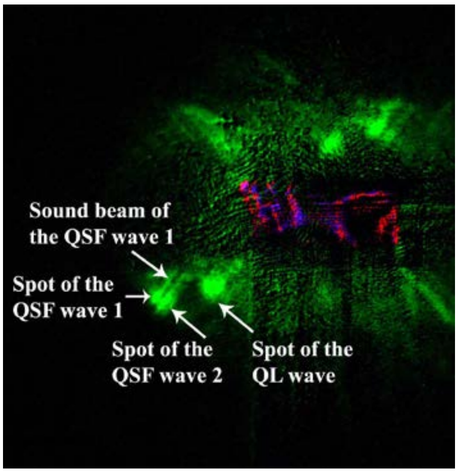

Fig. 1.1.1. Light diffraction pattern caused by acoustic waves in the TIRUS. “Optical respons-es” from different acoustic modes, quasi-longitudinal (QL) and quasi-shear fast (QSF) are observed despite the fact that only a slow shear wave (SSW) was excited in the crystal. The image is taken from [1].

its output, proved to be significantly greater than expected from an estimate. One more result obtained in [1] that required an explanation was strong instability of the TIRUS output observed in the experiments. All these experimental facts have led to the conclusion that in reality ultrasonic beams in a strongly anisotropic crystal, which is TeO_2, behave in a more complicated way.

The aim of the current project is to find actual reasons for the observed phenomena through a thorough study of physical mechanisms governing behavior of ultrasonic beams in the sensor body and to produce a vision for future develop-ments of the sensor. It can be achieved by a complex research including thorough experimental investigations of the TIRUS samples as well as building a more adequate theoretical model describing behavior of ultrasonic beams in the crystal. Apart from that, a special objective of the project is to prove the TIRUS capability to sense *subsurface* flaws because its feasibility has been proved only in experiments with the specimens having *surface* defects.

Thus, the tasks to be solved in the project are as follows:

- to get quantitative experimental data on spatial and temporal structure of acoustic fields in the sensor body by means of optical visualization of ultrasonic beams and pulses;
- to build an adequate theoretical model and calculate the field of radiated and reflected ultrasonic beams in the TeO_2 crystal of a limited size;
- to study instability of the TIRUS characteristics by means of temperature-controllable experiments;
- to prove the TIRUS capability to detect *subsurface* flaws testing specially fabricated specimens with artificial *subsurface* defects;
- to try the TIRUS in testing procedures using a “sliding technique” in which the sensor moves across a tested surface with a couplant between it and this surface;
- one more task to be solved is to develop an approach to reliable extraction of reference data from an unstable TIRUS output to be used in testing procedures.

1.2 Methods, Assumptions and Procedures

Solving the tasks formulated in section 1.1 involves a number of research activities independent on each other in their methods but producing interrelated results. They include visualization of an ultrasonic beam struc-ture using optical techniques, investigation of the TIRUS samples as a two port-network, numerical simulation of the sound field and post-processing of the TIRUS output using digital signal processing techniques.

Optical visualization is a part of research that provides an essentially valuable set of data because it reveals intrinsic features of ultrasonic beams in the TIRUS that cannot be uncovered any other way. Essentials of the technique applied in this research and described in section 8 are as follows. A light beam incident on a TeO_2

crystal, which is the TIRUS body, is diffracted by an ultrasonic wave propagating in the crystal. As a result, a diffracted beam appears behind the crystal and a diffraction pattern (a spot) corresponding to this wave can be watched in a plane of observation.

Thus, each light spot in the entire diffraction pattern observed behind the crystal can be related to a corresponding ultrasonic wave propagating in it. Because its intensity is in a certain way connected with the intensity of an ultrasonic wave that caused this spot, it is an indicator of the sound field intensity in the domain illuminated by the incident light beam. If an incident light beam illuminates the entire input face of the crystal, the light intensity distribution in the diffraction pattern will map the intensity distribution of the sound field in the crystal. In which case, however, additional optical elements will be needed to discriminate the diffracted and direct light beams because they will not be spatially resolved. Spatial filtration of the light beam mapping an acoustic wave of interest can be performed with an aperture in the focal plane of the lens placed behind the crystal.

A computer simulation of a 3D structure of ultrasonic beams in the crystal is a useful tool to guide a proper treatment of experimental results obtained from optical visualization. As such, in the current research a mathematical model is built and simulated based on the plane wave decomposition technique in an assumption that a radiated ultrasonic beam is excited by a pure tangential displacement existing only within a limited rectangular area at the boundary of the crystal. Details of the model and simulation results are presented in section 9.

Investigations of experimental samples as two port-networks presented in sections 3, 4, 6 and 7 are carried out in a conventional way of measuring the transfer function of the TIRUS with no specific preliminary assumptions about measurement procedures made. The only specific feature of measurements taken is that some of them were made using a phase meter specially developed in the frame of the project for time-gated measurements of the TIRUS transfer function. Its principle of operation, design and specific features are described in detail in Appendix A. Results presented in section 6 are obtained in the temperature controllable environment. Specific investigations of testing procedures using a couplant between the sensor and a tested specimen to enable the sensor to move across the specimen are carried out in section 7. The TIRUS capability to detect a subsurface flaw is studied in section 5 where a defective specimen is tested using the same conventional procedure for measurement of the insertion loss.

Research into possible ways to apply digital signal processing techniques to an unstable TIRUS output is accomplished in an assumption of no preliminary knowledge exists about the data analyzed except that they are the TIRUS output signals got in experiments. Their results are given in section 10.

2 The TIRUS Design and Fabrication of Experimental Samples

2.1 The TIRUS Concept

The concept of the total internal reflection ultrasonic sensor (TIRUS) as it was introduced and developed in [1] is as follows. Total internal reflection of a probing ultrasonic wave incident at the interface between the sensor and a tested object is frustrated if there is a subsurface flaw in the evanescent field under the interface (Fig. 2.1.1, a). As a result, the reflected wave is affected and the sensor output changes.

To provide total internal reflection at the interface with a large variety of tested materials the smaller velocity of the probing wave is better. Therefore, the slow shear wave (SSW) with the velocity ~600 m/s propagating along the [110] direction in the TeO_2 single crystal was chosen as a probing one. Polarization of the SSW is normal to the plane of the picture in Fig. 2.1.1. That is, with respect to the interface, it is a shear horizontal (SH) wave.

The simplest geometry of the crystal providing pure shear modes of the incident probing and reflected waves is shown in Fig. 2.1.1, b [2]. It is chosen in such a way that the incident and reflected waves propagate along the crystallographic directions [110] and [001] of the crystal respectively. In this case, the angle of incidence θ_0 can be found from the ratio of the velocities along directions [110] and [001]. In terms of the elastic stiffness constants, it yields [3]

$$\theta_0 = \arctan\sqrt{(c_{11} - c_{12})/2c_{44}}\ . \tag{2.1.1}$$

With taken from [4] values of stiffness constants c_{11}=5.57×10^{10}, c_{12}=5.12×10^{10} and c_{44}=2.65×10^{10} of N/m^2 the angle of incidence θ_0=16.25°.

According to a conventional procedure [5], a slowness vector of any refracted wave in the tested material can be found as a vector starting from the origin point O and ending at the intersection point B of a corresponding slowness surface with a normal to the interface *n* passing through the end of the slowness vector of the re-

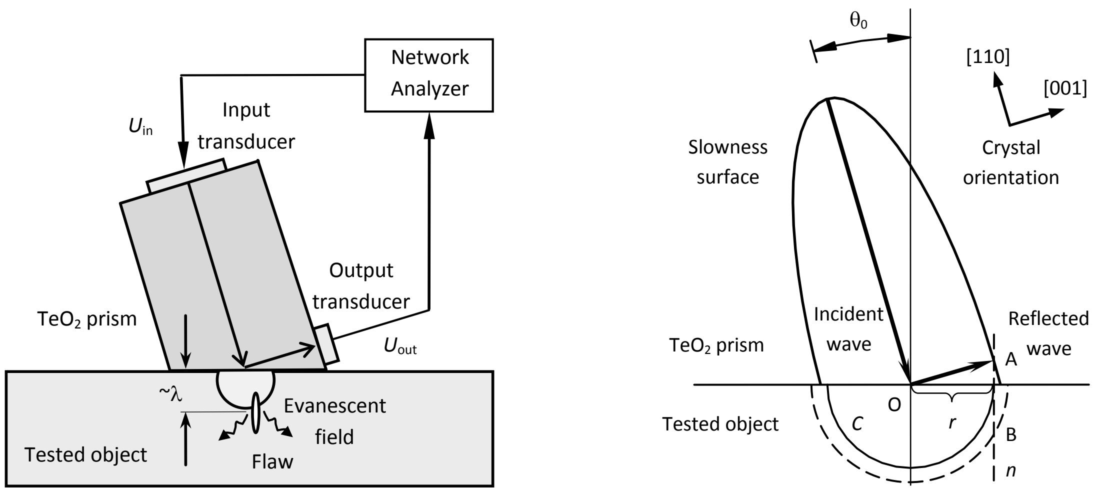

a b

Fig. 2.1.1. The TIRUS concept. a – configuration of the sensor-tested object "assembly"; b – geometry of the total internal reflection of the probing slow shear wave in the TeO_2 prism.

flected wave (point A) in the crystal. As seen from Fig. 2.1.1 (b), no such vectors can be found within the semicircle *C* because the normal *n* lies beyond its area. As a result, for all slowness values less than that defined by the radius *r* of the semicircle *C*, total internal reflection will take place. In other words, it will take place for all materials with velocities greater than a minimum boundary value v_{min}. For the case considered, a simple geometrical calculation gives the minimum velocity $v_{min}=v^I/\sin\theta_0=613/0.279=2190$ m/s, where v^I is the phase velocity of the incident SSW. Thus, the chosen geometry of the TIRUS provides its operational functionality while being applied to testing isotropic specimens with shear wave velocities greater than 2190 m/s.

An operational characteristic of the TIRUS can be defined in different ways but in any case it has to represent a change in its output U_{out} caused by the presence of a defect in the tested object. For the simplicity of experimental techniques in the study of the TIRUS functionality, it is preferable to make relative measurements of the TIRUS output instead of absolute ones, which require much more accurate procedures. Therefore in the current project, in all experiments where the TIRUS is studied as a sensor it is treated as a two-port network whose transfer function $T(f)$ is used as operational characteristic of the sensor. As usual, it is defined as

$$T(f)=U_{out}(f)/U_{in}(f)=|T(f)|\exp(i\phi(f)), \quad IL(f)=20\log|T(f)| \tag{2.1.2}$$

where f is a frequency, U_{out} and U_{in} are complex output and input of the sensor (see Fig. 2.1.1, a); ϕ is the phase of its transfer function, i is the imaginary unit. The logarithmic measure of the transfer function magnitude $|T|$ is the insertion loss $IL(f)$ of the TIRUS.

In the case of a pulse input of the TIRUS the above defined characteristic is modified into a time-gated transfer function T_{TG} whose "time gated insertion loss IL_{TG}" and "time-gated phase" ϕ_{TG} are

$$IL_{TG}=20\log U_{carr}/U_{in}, \quad \phi_{TG}=\phi_{carr}-\phi_{ref}. \tag{2.1.3}$$

Here U_{carr} and ϕ_{carr} are amplitude and phase of the output pulse carrier, ϕ_{ref} is the phase of a reference sinusoidal signal.

2.2 The TIRUS Design

The TIRUS was designed as a prism of a TeO_2 crystal cut and oriented according to the geometry presented in Fig. 2.1.1, b. The size of the prism is 23(L)×12(H)×10(D) mm along the [110], [001] and [1$\bar{1}$0] directions respectively. The 23 mm length of the crystal was chosen to enable the far field zone of the emitting side transducer to begin just at the distance of the inclined face of the crystal, in which case the cross-section of the probing wave field distribution on the reflecting surface is even enough [1]. Two identical 163º rotated Y-cut $LiNbO_3$ plates are bonded to the relevant faces of the TeO_2 crystal and ground down to a necessary thickness ~80 µm to serve as transducers operating at the frequency of 27 MHz. The inclined face of the prism is mirror-polished to be used as a sensitive surface of the sensor enabling application of an optical contact technique to put the sensor in contact with a tested speci-

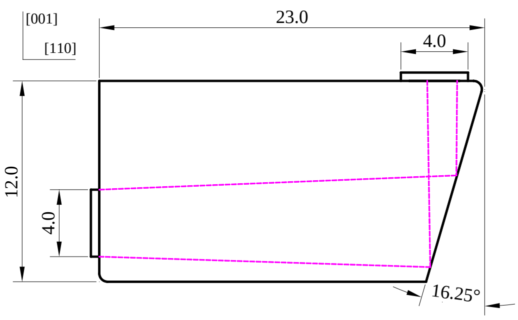

Fig. 2.2.1. The TIRUS design.

men.

Unlike the sample fabricated in [1] where the size of the receiving top transducer was 2.5 mm, in the current project its size was 4 mm (Fig. 2.2.1). The idea behind the increased size of the receiving transducer was to provide “reliable collection of all energy” of the reflected ultrasonic beam and in such a way to decrease insertion loss of the TIRUS that seemed to be unexpectedly large [1]. To what side effects it has led is described in sections 4.2 and 8.4.3.

2.3 Fabrication of Experimental TIRUS and Loss Samples

Two types of experimental samples were fabricated to experiment with, “Loss Samples” and “TIRUS Samples”. The TIRUS samples were actual sensors to be investigated, their design is described in the previous section. The loss samples had no inclined reflecting surface changing a propagation direction of an ultrasonic wave in the crystal. They were meant specially for finding a reason for a high value of losses in the TIRUS samples investigated as a two-port network [1] and were designed as a simple ultrasonic delay line made of the TeO_2 crystal with two transducers located exactly opposite to each other.

Both the TIRUS and the loss samples were fabricated from identical rectangular bars of the TeO_2 crystals of 23×12×10 mm in size; two opposite (L×H) surfaces of every bar were covered with antireflection coatings for wavelength of 532 nm with the reflection coefficient ≤0.1%. At the first stage of fabrication, piezoelectric plates of $LiNbO_3$ were welded to corresponding surfaces of original bars. In the case of the lost samples, those were on opposite (H×D) surfaces; at the next stage, the plates were ground and then polished down to a necessary thickness. After deposition of electrodes the loss samples were ready for mounting into a crystal holder. In the case of the TIRUS, piezoelectric plates were welded separately to (L×D) and to (H×D) surfaces of the crystal. After welding, grinding the plates down to necessary thicknesses and deposition of electrodes, the intermediate experimental samples were obtained not having yet an inclined surface but with two shear wave transducers, one on the (110) and another on the (001) surfaces of the crystal. Some results obtained with such an intermediate sample are described in section 8.4.2, Fig. 8.4.4, (*a*). The final operations in the TIRUS body fabrication were cutting a part of the crystal with a diamond saw to get a properly oriented inclined face and subsequent grinding

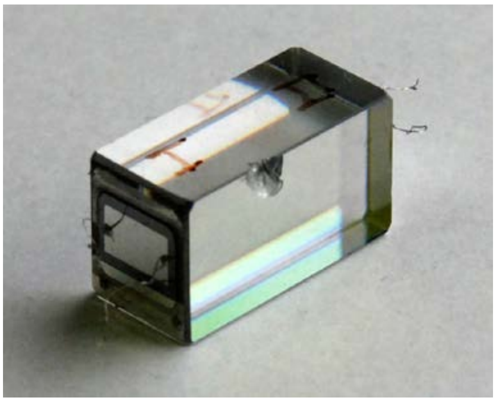

a, sample Uj1

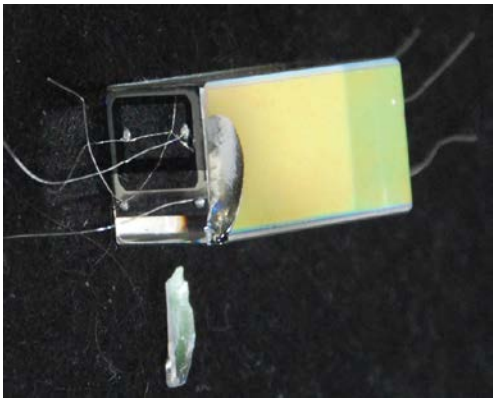

b, sample Uj2

Fig. 2.3.1. “Loss samples” fabricated from the TeO_2 crystals. Uj1 and Uj2 are the identifiers of the fabricated samples. a – the transducers are bonded in the center of the crystal; b – the transducers are bonded close to a side surface of the crystal, *exactly as in the TIRUS samples*. Both fabricated cells were damaged while mounting into the housings.

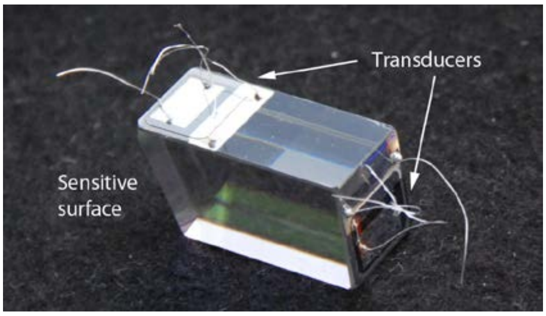

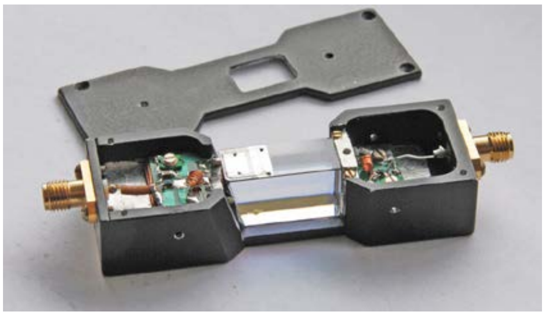

a b

Fig. 2.3.2. The fabricated TIRUS sample Uj4. a – the crystal itself (a sensor); b – the crystal mounted in the housing designed for optical investigations. The crystal can be illuminated from two directions, [110] and [001] (partly). The sensitive surface of the crystal is free and does not touch the housing but in experiments, it is unavailable for any mechanical contact. Matching circuits provide 50 Ohm input impedance with the VSWR not worse than 1.1 at 27 MHz.

and polishing of its sensitive surface. In the course of the project, two loss samples and two TIRUS samples were fabricated and studied that will further be identified as Uj1, Uj2 and Uj3, Uj4 respectively.

The fabricated loss samples are presented in Fig. 2.3.1. They have essentially different designs: in the Uj1 sample the transducers are bonded in the center of the (H×D) sides of the crystal. On the contrary, in the Uj2 sample they are bonded close to the (L×D) side of the crystal, exactly in the same way as it is done in the TIRUS design (Fig. 2.2.1). It was done to study in experiments whether a close location of the emitting transducer in the loss sample affects the sample features, particularly if it does increase its insertion loss, and consequently such a design can affect the TIRUS features as well.

As seen in Fig. 2.3.1, both fabricated loss samples have minor damages, which were a result of extreme fragility of the crystals used. Nevertheless, the fabricated samples proved to be suitable for examination, especially in measurements of their insertion losses as two-port networks, in which case the damages did not affect the results. In optical experiments, they certainly did so because of their screening effect, however main features of visualized acoustic fields in the samples could be observed in these experiments too.

An appearance of the fabricated TIRUS sample Uj4 is presented in Fig. 2.3.2 (a). In optical experiments, it was mounted in a specially designed housing providing illumination of the entire transparent (L×D) area of the crystal but screening side stray light. Figure 2.3.3 demonstrates the same crystal mounted into the “sensor housing” which was used in all experiments with the TIRUS as a two-port network.

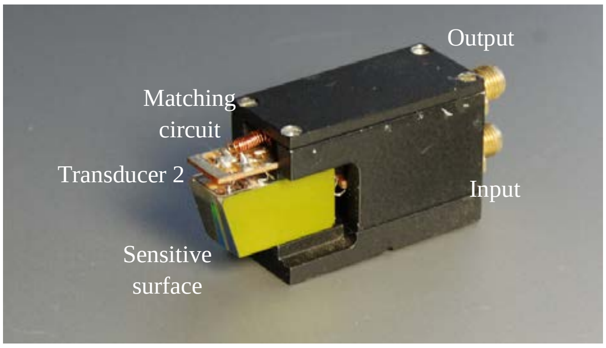

Fig. 2.3.3. The TIRUS sample Uj4 mounted into the “sensor housing”. The (L×H) face of the crystal is coated with protective lacquer.

In addition to two TIRUS samples Uj3 and Uj4 fabricated in the current project, one more TIRUS sample fabricated in the previous project was used in experiments. It was identified as the Ug2 sample and differed from samples Uj3 and Uj4 in its design. Its side transducer was exactly the same but the top transducer was of 2.5 mm in size instead of 4 mm (see Fig. 2.2.1). In the course of experiments, its sensitive surface was damaged but then the sample was refurbished and used again. This refurbished one had slightly different characteristics and was identified as the Ug2_2 sample. Therefore in the description of experimental results obtained in further sections all four TIRUS samples Uj3, Uj4, Ug2 and Ug2_2 are mentioned.

2.4 Fabrication of Specimens with Subsurface Defects

One of the tasks solved in the current research is verification of the TIRUS as a sensor capable of detecting *subsurface flaws* because in the previous research [1] its feasibility was proved only in experiments with specimens having *surface* defects. A necessary means for such verification is a specimen with a subsurface flaw located immediately under the surface at a depth of the order of the acoustic wavelength in a tested material.

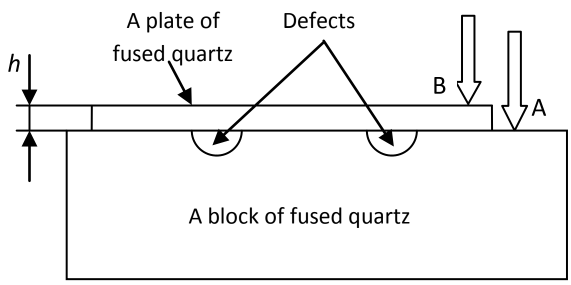

Fig. 2.4.1. Technique for manufacturing a specimen with an artificial subsurface defect. The plate thick *h* determines a depth of the defect.

With the operating frequency of the TIRUS equal to 27 MHz and a minimum sound velocity acceptable to provide total internal reflection at the interface (see section 2.4) of 2190 m/s, the distance to the flaw should be as short as 81 μm. It is very difficult to fabricate an artificial defect within this range in a flawless block of a material. The use of a material with a higher acoustic wave velocity slightly improves the situation: in fused quartz, e.g., the shear wave velocity is ~3750 m/s that makes the wavelength be equal to 139 μm. Therefore, fused quartz was chosen as a material for making specimens with artificial defects.

Manufacturing a defect at a depth of 50-100 μm using conventional procedures [6] such as side-drilled or flat-bottomed holes is extremely difficult if not impossible because it has to be located and aligned with precision not worse than 10-20 microns with respect to the specimen surface. For this reason, a different technique was developed based on the use of an artificial layered structure with a defect located under a surface layere, which was a thin plate bonded to a solid block of fused quartz. The plate was also made of fused quartz so the entire “assembly” may be considered a specimen with a subsurface defect if it is located underneath the plate (Fig. 2.4.1) and the plate thickness is less than the wavelength in fused quartz.

The idea behind the fabrication of a specimen is as follows. All horizontal surfaces of the assembly parts including a *thick* plate and a block of quartz can be made parallel and aligned perfectly at a first preparation stage. After bonding the plate to the block, the plate is ground to a given thickness and polished. Its thickness *h* determines a “depth of the defect” and is controlled easily in the grinding process as a difference between readings A and B of an optimeter.

In the course of the project, a few designs of defected specimens with a “void type” or discontinuity defects were tried; none of them, however, proved to be usable as a defected specimen in experiments with the TIRUS. One of the designs tried is shown in Fig. 2.4.2. At an intermediate stage of the fabrication process, a thick plane parallel plate of fused quartz was bonded to a block of the same material with epoxy resin. A thickness of an epoxy resin layer was determined by a thickness of Teflon strips under the plate that was 50 μm. Af-

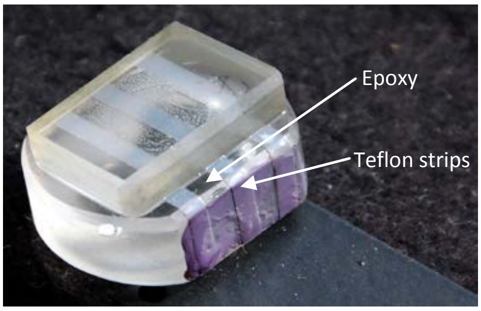

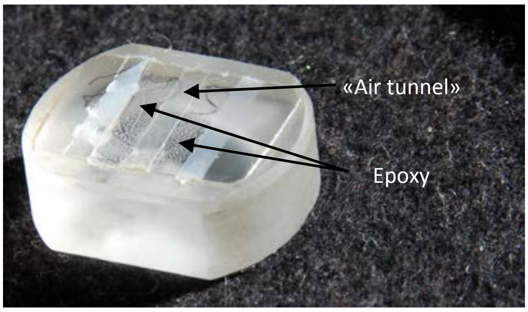

a b

Fig. 2.4.2. Fabrication of a defected specimen with an "air tunnel" type of a defect. a – the plate of fused quartz is bonded to a block of the same material with epoxy resin; its thickness is 50 μm and is determined by the thickness of Teflon strips. b – the plate is ground and polished down to the thickness of 90 μm and the strips are pulled out.

ter grinding and polishing down the top plate the strips were pulled out from the epoxy layer making an "air tunnel" of 50 μm height in the epoxy layer that was supposed to be a defect. After processing, the thickness of the plate was 90 μm. Thus, the defected specimen of interest had been produced but further it did not pass a test with the TIRUS using an optical contact technique because a too large area (~3×12 mm) of the thin (90 μm) "ceiling" of the air tunnel was damaged in a testing procedure.

Another design is presented in Fig. 2.4.3 (b). The plate is bonded to a block of quartz using the technology of vacuum diffusion welding therefore the thickness of the bonding layer is less than 1 μm. The well-type holes of 2 mm in diameter drilled in the block are completely isolated and buried under the plate forming actual *vacuum* voids. As a result, after grinding and polishing the plate down to the thickness of 110 μm the plate areas above the surfaces of the voids started to deform due to atmospheric pressure and one of them was even damaged. This made the specimen unusable for further experiments.

Because the attempts to fabricate the specimens with the void-type defects failed, specimens with a "foreign inclusion" type were fabricated [2]. They were made in the same way, with the plate of fused quartz bonded to the top surface of its solid block. In this case, however, the intermediate bonding layer of cured epoxy res-

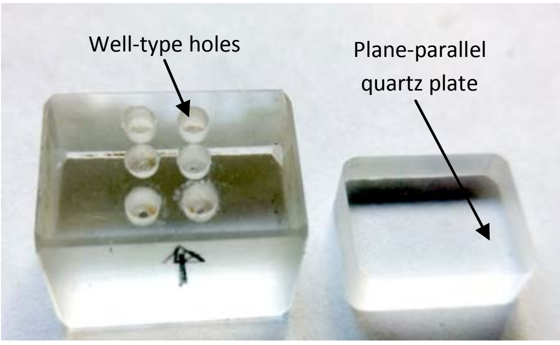

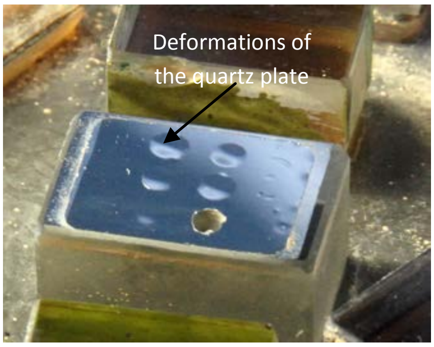

a b

Fig. 2.4.3. Fabrication of a defected specimen with a "well-type" defect. a – the well-type holes are drilled in a block of fused quartz. b – the plate of the same material is bonded to it, then ground and polished down to the thickness of 110 μm; the plate areas above the wells are deformed due to atmospheric pressure, one of them is damaged.

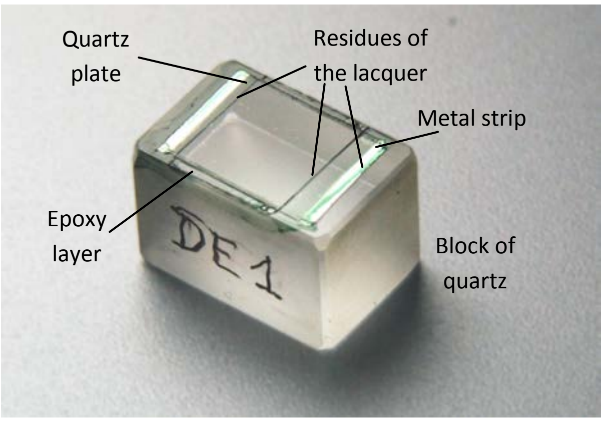

Fig. 2.4.4. Specimen with a subsurface defect of a “foreign inclusion” type. A quartz plate of 60 μm in thickness is bonded to the block of quartz with epoxy resin. The epoxy layer thickness is 53 μm.

in was by itself a subsurface defect of a foreign inclusion or inhomogeneity type.

Figure 2.4.4 demonstrates a similar specimen. In the fabrication process, a thick quartz plate was aligned on metal strips of 50 μm in thickness and the liquid epoxy resin was pressed out from under it. After curing the epoxy layer, the plate was ground to a necessary thickness and polished. In the case presented in the figure it was 60 μm. (The picture in the figure was taken immediately after demounting the specimen from the TIRUS sensitive surface after carrying out experiments using the optical contact technique therefore the residues of protective lacquer are still seen on the surface of the bonded quartz plate). The fabricated specimens were used in the experiments meant to examine the TIRUS capability to detect subsurface defects, which in these cases were an epoxy layer between a thin plate and a block of fused quartz.

3 Examination of Experimental Samples As Two-Port Networks: Continuous Wave Measurements

In the current project, an approach used to simplify experimental techniques in the study of the TIRUS as a sensor implies treating it as a two-port network whose transfer function *T*(*f*) is the sensor output; in which case relative measurements can be done instead of absolute ones that are much more difficult to do. The same holds for the loss samples described in section 2.3. Measurements of operational characteristics of fabricated experimental samples were carried out in two different ways, using a continues wave (CW) or a time-gated (TG) technique. In the first, conventional measurement instruments were used enabling measurements to be made in an arbitrary frequency range. In the second, a specially developed device operating at 27 MHz was used. It is described in detail in Appendix A. Details of the measurement techniques are described in the corresponding sections of the report.

3.1 Examination of Loss Samples

An essential step in experimental investigations of the "Loss samples" was measurement of their complex transfer function *T*(*f*) defined in section 2.1. Both its parts, magnitude and phase were measured. Results reported here concern only to its magnitude part, the insertion loss $IL(f) = 20\log|T(f)|$.

Measurement of the insertion loss in the continuous wave mode was carried out with a network analyzer. The measurement setup used in the experiments is shown in Fig. 3.1.1. The experiments were conducted as series of measurements made on two different days. Each series consisted of six measurements made in the frequency band of 10 kHz around 27 MHz taken at different moments of time within one day. Measurement results of the first series for the loss sample Uj2 are presented in Fig. 3.1.2.

An analysis of the results obtained shows that the insertion loss of Uj2 is obviously unstable in time. The characteristics *IL*(*f*) look as if they shift along the frequency scale in an arbitrary manner depending on time of measurement. Similar results were obtained in experiments with the sample Uj1. The observed instability is very similar to that observed in [1] in experiments with the TIRUS sample Ug2 (see section 2.3).

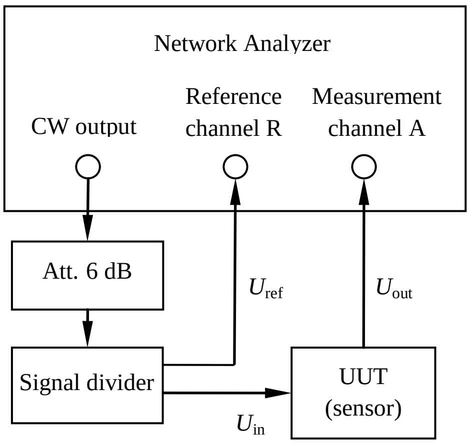

Fig. 3.1.1. Measurement setup used in the continuous wave experiments. UUT stands for unit under test. (The picture is taken from [1]).

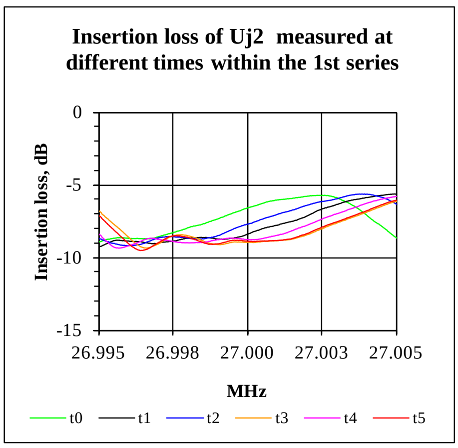

Fig. 3.1.2. Insertion loss of sample Uj2 measured at different times within one day. Time points t0-t5 are taken at 12:05, 12:31, 13:30, 14:07, 14:42 and 15:20.

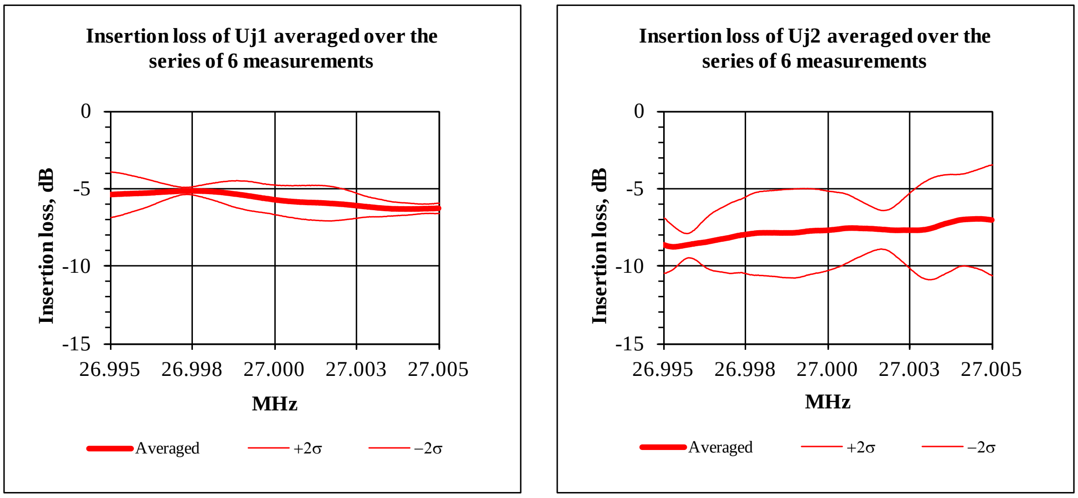

a *b*

Fig. 3.1.3. Averaged CW insertion losses (thick lines) of samples Uj1 and Uj2; the ±2σ bands (thin lines) determine the 95% confidence intervals.

At the same time, there is a significant difference between measured values of insertion losses of the TIRUS [1] and those of the loss samples. For the TIRUS sample, the averaged value of *IL*(*f*) measured in the 50 kHz band lay within the range of 13.2-17.6 dB. For the measurement series of the loss sample Uj2 presented in Fig. 3.1.2, it is within the range of 6.4-9.1 dB. That is, there is a distinctive difference of the order of 6 dB. Thus, since in the loss samples the crystals have no tilted surfaces, one might infer that a high value of the insertion loss of the TIRUS is probably connected with reflection of the ultrasonic beam from the inclined surface of the crystal.

A comparative analysis of the results obtained for samples Uj1 and Uj2 can be done on the base of graphs displayed in Fig. 3.1.3. These graphs can also be used to compare CW and time-gated data presented in the corresponding sections. To make the difference more vivid, the series of measurements having maximum measurement errors at frequency of 27 MHz were selected for the analysis. The averaged values of insertion losses proved to be -5.7±1.0 dB for sample Uj1 and -7.7±2.6 dB for sample Uj2, i.e., a distinctive difference between them was observed. As seen from Fig. 3.1.3, a 95% confidence interval (±2σ) is also significantly greater for sample Uj2 than that for Uj1.

A possible reason for that may be the difference between the samples designs: transducers of sample Uj1 are placed in the center of the crystal whereas those of sample Uj2 are shifted from the center towards one of the crystal side surface. That might probably lead to additional losses if the radiated sound field “touches” this surface. Results of optical visualization of ultrasonic fields in the loss samples made in section 8.4.1 show that not only this “touch” but also imperfection of the crystal itself might well be the reason.

3.2 Examination of TIRUS Samples

3.2.1 Testing of Fabricated TIRUS Samples

Measurements of the transfer function of two fabricated samples Uj3 and Uj4 were made with the same technique as in the previous section. Despite the fact that both samples had exactly the same design and were fabricated in the same manner, their transfer functions proved to be drastically different.

An experimental TIRUS sample assembly consists of the TeO_2 crystal with two bonded shear wave transducers placed into a metal housing. Matching circuits for the transducers are also mounted in the housing. In the conducted experiments two types of housings were used. The “optical housing”, (see Fig. 2.3.2 in section 2.3) was specially designed for screening stray light in optical visualization of ultrasonic beams in the crystal. Another one was designed to use in experiments with the TIRUS as a sensor. In it, a sensitive surface of the crystal was left open (Fig. 2.3.3 in section 2.3). In both cases, the TIRUS samples could be studied as two-port networks having two connectors, input and output.

Frequency responses of the studied samples in the optical housings are presented in Fig. 3.2.1. The obtained results proved to be absolutely unexpected because the insertion loss of the Uj3 sample was at least by 20 dB greater than that of Uj4. To find a reason for such a difference, matching circuits were removed from both samples and insertion losses of the TIRUS bodies themselves were measured. Measurements were made with ultrasonic waves propagating in two opposite directions sequentially. In the first case, the ultrasonic wave was emitted into the [110] direction of the crystal by the side transducer; in the second case, it was emitted into the [001] direction by the top transducer, i.e., the sensor operated in a reverse manner. Naturally, the receiving transducers were altered respectively.

The frequency responses measured are shown in Fig. 3.2.2. The notes [110]>[001] and [001]>[110] in the legend denote “direct operational mode” and the “reverse operational mode” respectively. As seen from the figure, in the direct mode the insertion loss of Uj3 (red line) is by approximately 10 dB greater than that of Uj4 (blue line). It means that at least a half of the observed difference of 20 dB in the entire loss of Uj3 is caused exclusively by “events in the crystal itself”, which is completely inexplicable. A similar difference is observed between insertion losses measured in the reversed mode. In both cases, there is no visible reason for such a high loss value of Uj3 compared to Uj4, therefore answering the question why this phenomenon is observed requires further thorough investigations that should include fabrication of additional TIRUS samples.

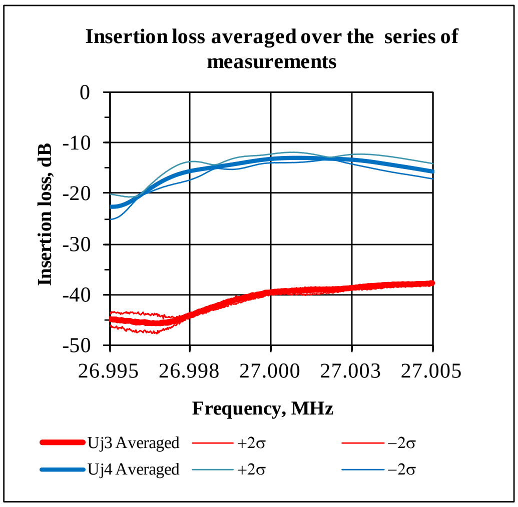

Fig. 3.2.1. Insertion losses of the fabricated TIRUS samples mounted in the optical housings. An ultrasonic wave is radiated into the [110] direction. ±2σ (thin lines) determine 95% confidence intervals.

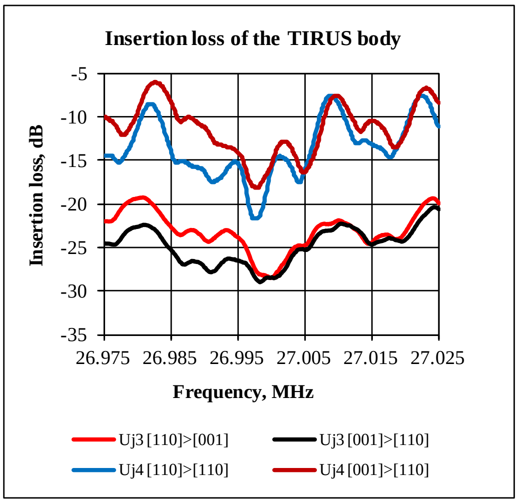

Fig. 3.2.2. Insertion losses of the fabricated TIRUS samples with matching circuits removed. The direction of the sound propagation from the emitting to the receiving transducer is denoted by symbol ‘>’.

A noticeable difference is also observed between insertion losses measured in the direct and opposite directions for each of both samples examined, particularly in the low frequency range of the frequency responses. Which is not, though, very surprising taking into account the fact that the design of the fabricated samples is not symmetrical. What is surprising is that this difference manifests itself mainly in the low frequency part of the frequency response because the maximum frequency change does not exceed 0.15% within the entire frequency range of measurement, i.e., it is too small to cause such a noticeable change in the response.

Because of such a great value (~40 dB) of the insertion loss of Uj3 there was no sense to use it as a sensor and it was excluded from further studies as a two-port network. However, it was investigated using optical techniques. Results of these investigations are presented in sections 8.4.3 and 8.4.4.

3.2.2 Examination of the Uj4 Sample

The measured value of the insertion loss *IL* of the TIRUS expressed in decibels is a sum of a few different types of losses resulted from different physical phenomena. Some of them are connected with propagation and reflection of ultrasonic waves in the crystal, others with electro-acoustic transduction. Estimates of values of the different types were made in [1] but neither propagation losses nor transduction losses *TL* were measured. It is connected with significant experimental difficulties in differentiating between them when a ready TIRUS sample is studied. There is also no way to reduce the transduction losses *TL* when transducers are already bonded to the crystal except match them to external electronics.

If the transducers are bonded to the crystal with small acoustic attenuation, which is the case of the fabricated TIRUS samples, results of matching can be rather unexpected because of acoustic resonances of the crystal. Figure 3.2.3 shows a Voltage Standing Wave Ratio (VSWR) of the emitting (red line) and the receiving (black line) transducers measured in the bandwidth of 8 MHz with frequency resolution of 20 kHz. Measurements were made at the TIRUS terminals after completion of an initial matching procedure.

As seen from Fig. 3.2.3, VSWR of the TIRUS input (transducer 1) in the vicinity of the operating frequency 27 MHz is about 2 that corresponds to the reflection loss RL=0.5 dB. Here $RL=-10\cdot\log(1-|\Gamma|^2)$ [7, p. 465] is a part of transduction losses *TL* and Γ is an electrical reflection coefficient. At the same time, the TIRUS output (transducer 2) demonstrates much greater range of the VSWR values change near 27 MHz. It supposes that the VSWR measured with much greater resolution might well be unpredictably large.

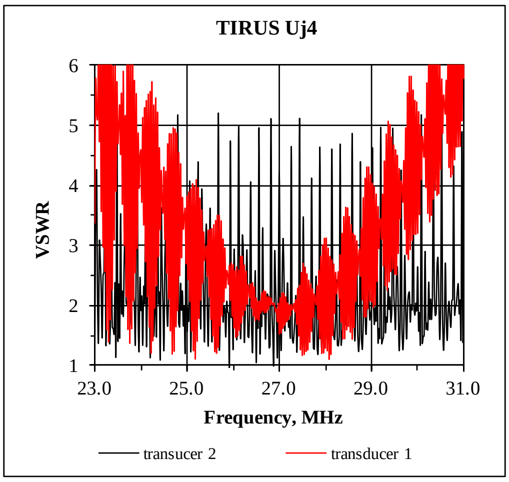

Fig. 3.2.3. VSWR of the TIRUS input and output measured in the bandwidth of 8 MHz. (Transducers 1 and 2 respectively).

As a matter of fact, it happened to be so. Results of measurements taken in the 40 kHz bandwidth (resolution of 100 Hz) are presented in Fig. 3.2.4. Measured on two different days, the VSWR at 27 MHz gave two different values of 4.2 and 1.7 and, as seen from the VSWR value in the vicinity of 26.99 MHz, might have occurred to be much greater than 6. This shows how a change in the resonance frequency of the crystal can

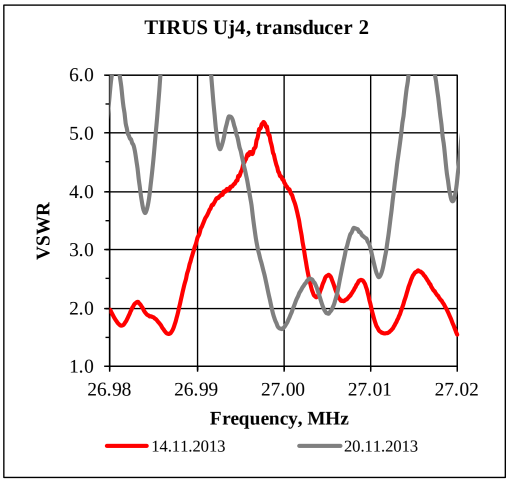

Fig. 3.2.4. VSWR of the TIRUS output measured in the bandwidth of 40 kHz. Measurements are taken on two different days.

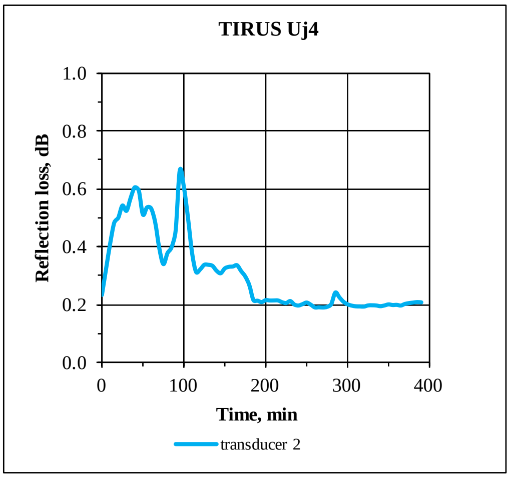

Fig. 3.2.5. Change of the reflection loss *RL* of the TIRUS output in time. Sample Uj4, operating frequency 27 MHz.

mismatch the TIRUS output in time.

To check how this phenomenon affects TIRUS characteristics, the reflection coefficient of the Uj4 output was measured through 400 min within one day with 5 min intervals between taken measurements. The reflection loss *RL* calculated from the measured reflection coefficient Γ is presented in Fig. 3.2.5. As seen from the figure, the maximum measured value does not exceed 0.7 dB. This is too small a value to really affect results of measurements of total insertion losses, which are of the order of 15 dB. Thus, the effect of electrical mismatch of the transducer due to resonances of the crystal cannot be a reason for observed instability of the TIRUS frequency responses and an actual reason is connected only with phenomena of propagation and reflection of ultrasonic beams in the TIRUS body but not with a change in values of transduction losses *TL*.

Experiments with the Uj4 sample included not only measurements of its characteristics but also collection of raw data meant for the use in the development of a technique for extraction of reference data from an unstable TIRUS output. For this purpose, a special raw data set of frequency responses *IL*(*f*) was formed. A frequency range chosen for measurements had to be large enough to contain “key features” of the analyzed TIRUS output, e.g. the waves on the frequency response, to be extracted with the technique developed. Two frequency ranges in the vicinity of the operating frequency of 27 MHz were tried. As seen in Figs. 3.2.1 and 3.2.2, frequency responses measured in the bandwidth of 10 and 50 kHz differ essentially: in the 50 kHz bandwidth the “waves” on the responses cased by acoustic resonances of the crystal are well noticeable whereas in the 10 kHz bandwidth they are smooth. Therefore, the latter is unsuitable as an input for a sinusoidal model developed in section 10 for post processing of experimentally obtained data. For this reason, the 50 kHz range was chosen as a suitable one.

An averaged characteristic of a typical raw data set is illustrated in Fig. 3.2.6. The set consists of 120 frequency responses taken across an hour period of time with intervals of 30 seconds. From the entire data set, six single measured frequency responses taken over 10 min intervals were selected and averaged to represent the acquired data in the diagram. A 95% (±2σ) confidence interval was calculated using these six selected responses. The data presented in Fig. 3.2.6 were taken in the CW experiments with the Uj4 sample placed into the opti-

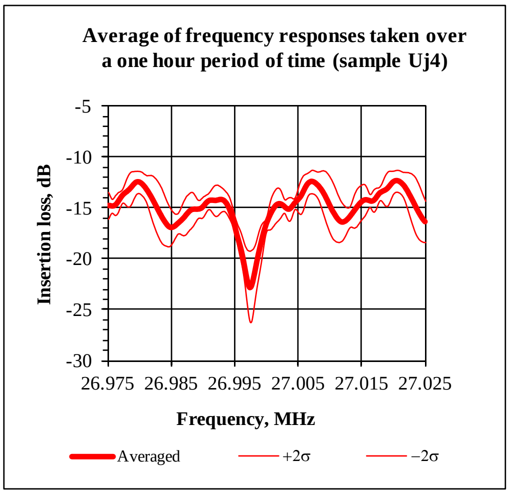

Fig. 3.2.6. Frequency responses of the TIRUS sample averaged over a one-hour period. Sample Uj4 is placed in the optical housing. ±2σ (thin lines) determine a 95% confidence interval.

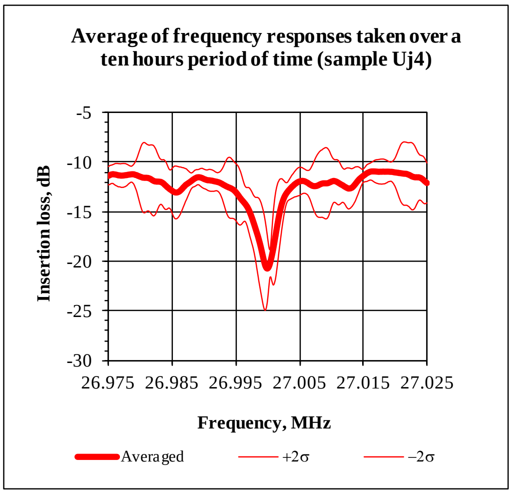

Fig. 3.2.7. Frequency responses of the TIRUS sample averaged over a ten-hours period. Sample Uj4 is placed in the sensor housing. ±2σ (thin lines) determine a 95% confidence interval.

cal housing (see Fig. 2.3.2 in section 2.3). Similar raw data presented in Fig. 3.2.7 but obtained across a ten hours period were acquired with the Uj4 sample placed into the sensor housing. One can see that both characteristics look similar, however the ±2σ interval is noticeably wider in the case of the ten hours measurement period.

3.3 Conclusions

Main conclusions that can be inferred from data acquired in this section are that:

– the high value of the insertion loss of the TIRUS is connected first of all with its specific design, namely with the polygonal path of propagation of an ultrasonic beam in its body;

– propagation of the ultrasonic beam near a boundary of the crystal contributes additional losses to the total insertion loss of the TIRUS;

– more experimental samples of the TIRUS should be fabricated and investigated to find an unequivocal reason for the high value of the TIRUS insertion loss;

4 Examination of Experimental Samples As Two-Port Networks: Time-Gated Measurements

In the previous project [1], conventional measurement instruments such as an oscilloscope and signal generators were used to measure the time-gated transmission coefficient T_{TG} defined in section 3.1, equation (3.1.3). However, data obtained did not contain any information on the phase shift of the carrier of the output RF pulse with respect to the phase of the input. Since in the TIRUS a phase shift of the reflected wave received by the output transducer can carry information on a change in the boundary conditions on its sensitive surface, it is worth measuring this shift. Time gated measurements enable also to mitigate an effect of instability of the TIRUS transfer functions $T(f)$ that should be referred to an influence of temperature that affects a resonance frequency of the TeO_2 crystal. In the current project, time gated measurements were carried out using a specially developed phase meter that is described in detail in Appendix A. All measurements were done with the carrier frequency of 27 MHz.

4.1 Examination of Loss Samples

In time gated measurements, a RF pulse from the driving part of the meter was applied to the input of a tested loss or TIRUS sample and in a calibration procedure its amplitude U_{in} was established to be 0 dB, which provided values of the sample output IL_{TG} to be measured in dB too.

In the experiments described here, duration of the driving pulse was 5-10 µs that was much less than the propagation time of the slow shear wave in the crystal equal approximately to 37 µs. To reduce influence of transient effects on the measured values, the time point for sampling the phase difference ϕ_{TG} was chosen by 3-4 µs later than starting points of the output pulses. Since the frequency of the carrier was 27 MHz, that provided ~80 periods of the carrier to come to normal before sampling. Measurements were also done for triple-transit signals [8] that passed the whole length of the crystal three times.

The procedure for the time-gated measurements is closely connected with specific features of the phase meter developed and reliability of data obtained is determined by its schematic and accuracy of a pre-measurement calibration procedure. Therefore, some measurements made with the phase meter then were repeated with an oscilloscope as a recording device of the measurement system.

Measurements of IL_{TG} and ϕ_{TG} were carried out for both loss samples fabricated, Uj1 and Uj2. Taking into account that the phase characteristic of the phase meter was linear only within the range of 30-150°, for sample Uj2 the measured values were chosen from the 300 s periods in which they lay on the linear part of the calibration graph. Duration of the whole measurement series from which these periods were extracted was ~1 hour. For sample Uj1, practically all values taken within a 1-hour period lay within the linear interval therefore a complete set of taken values is presented. In all experiments parameters of both single-transit and triple-transit pulses were measured.

Measurement results are presented in Fig. 4.1.1. The values of the insertion loss measured at 27 MHz and computed from the data acquired were -7.7 dB ± 0.1 dB for the sample Uj1 and -7.2 dB ± 0.1 dB for the sample Uj2, which are very close to the result obtained in CW measurements for sample Uj2 (-7.7±2.6 dB) but differ significantly from that for sample Uj1 (-5.7±1.0 dB). This difference is inexplicable and more experimental samples and measurement data are needed to come to a satisfactory explanation.

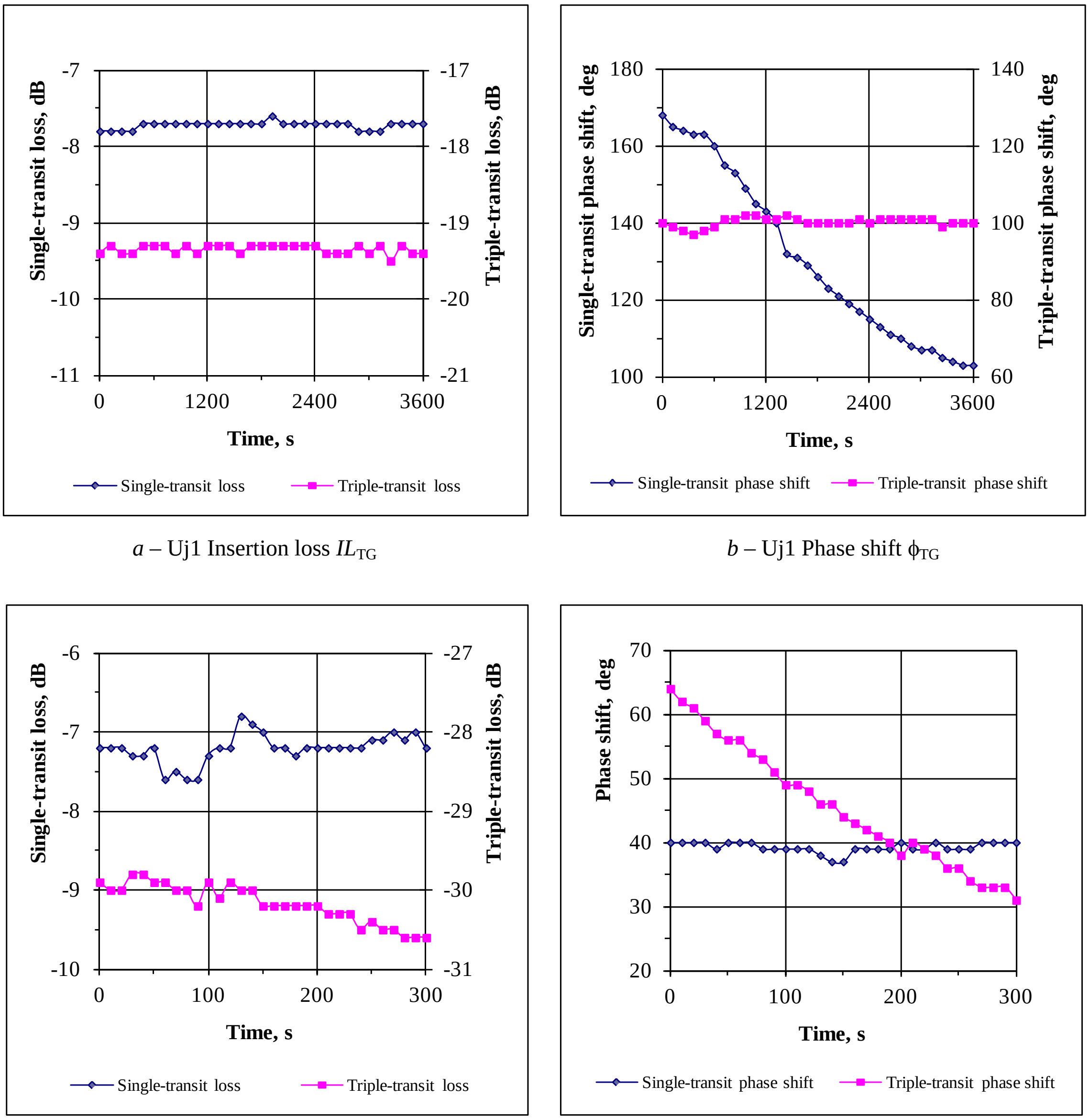

a – Uj1 Insertion loss IL_{TG}

b – Uj1 Phase shift ϕ_{TG}

c – Uj2 Insertion loss IL_{TG}

d – Uj2 Phase shift ϕ_{TG}

Fig. 4.1.1. Results of time-gated measurements carried out with the phase meter developed.

Data of phase measurements for sample Uj1 occurred to be considerably different from those for Uj2. For Uj2, a temporal, probably temperature, instability of the phase shift of the triple-transit pulse was an order of magnitude greater than that of the single-transit pulse (Fig. 4.1.1 *d*). If it was not for the data obtained for Uj1, it could have been explained by influence of a spurious CW signal having a level of -40 dB with respect to the input on the weak triple-transit signal. However, for Uj1 the result was opposite (Fig. 4.1.1 *b*): instability of the single-transit pulse was an order of magnitude greater than that of the triple-transit pulse.

Some measurements made with the phase meter were repeated with an oscilloscope used as a testing device. A block-diagram of the measurement setup with the oscilloscope Tektronix TDS2022 is presented in Fig. 4.1.2. The driving part of the phase meter provides a RF pulse signal (27 MHz, 5 μs) that is divided into two channels, the measurement one and the reference one. The loss sample input U_{in} equal to the signal in the reference channel U_{ref} and its output U_{out} in the measurement channel is measured with the oscilloscope. The

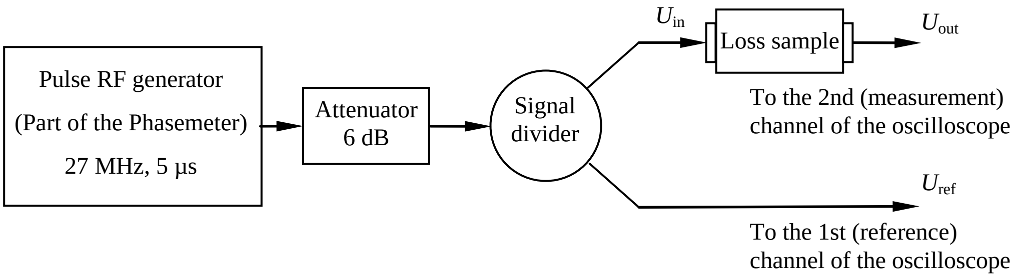

Fig. 4.1.2. A setup for time-gated measurements with the phase meter and an oscilloscope.

oscilloscope inputs are connected to the channels through the BNC "T" connectors shunted with the 50 Ohm terminators that provides accurate division of the input signal by a broadband (0÷12.4 GHz) 50 Ohm signal divider. In this case, the measured insertion loss is calculated simply as

$$IL_{TG}=20\ \log U_{out}/U_{ref}\ . \tag{4.1.1}$$

Conducted measurements resulted in the measured value IL_{TG}=-7.9 dB, which is in a good agreement with the results obtained with the phase meter alone.

4.2 Examination of the TIRUS Samples

Time-gated measurements of insertion loss IL_{TG} of the TIRUS samples were carried out using the phase meter developed and thoroughly studied in Appendix A therefore neither the instrument itself nor a measurement technique are described here. Only results obtained with the sample Uj4 are presented because the insertion loss value of the sample Uj3 occurred to be unreasonably high and were omitted. All measurements were made after warming up the instrument for about ten minutes and performing a calibration procedure that resulted in precision of the overall results obtained not worse than 1 dB for amplitudes of measured pulse signals greater than -30 dB with respect to a probing RF pulse and fell down to 3 dB for amplitudes -40 dB.

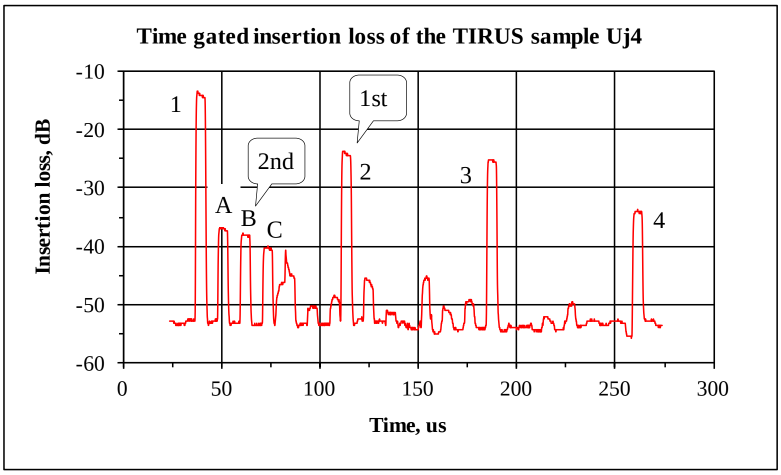

Fig. 4.2.1. Waveform at the RSSI output of the time-gated phase meter. The TIRUS sample Uj4 is studied. Two pulse trains, the first (1st) and the second (2nd) ones are observed. Pulses of the first train are numbered 1 to 4, of the second – A to C.

A typical waveform at the RSSI output of the phase meter recorded with a digital oscilloscope is presented in Fig. 4.2.1. As seen in the figure, it has a rather complicated character and, omitting a noise component, can be treated as two different pulse trains marked as the first and the second ones. The first train is produced by ultrasonic pulses passing through the TIRUS crystal in an ordinary way, which can be concluded from studying the time delay between sequential pulses in the train marked with numbers 1 to 4. They travel from the transmitting to the receiving transducer, reflect from the latter and repeat the entire back and forth path again that results in the 74 μs delay time between them. The delay of the first pulse with respect to a probing RF pulse whose position corresponds to the beginning of the time scale is 37 μs because it travels only in one direction.

Behavior of the pulse sequence of the second train cannot be explained in such a simple way. As will be shown in section 8.4.2, the presence of these pulses is a consequence of the mismatched sizes of the transmitting and receiving transducers that results in generating pulses travelling forth and back along the [001] axis between top and bottom surfaces of the crystal. Actually, the time delay between them (i.e., between pulses A and B) is equal to ~12 μs that corresponds to a passing time of a shear wave through a path of 24 mm length that is equal to the double height of the crystal.

The key feature of the time-gated technique is its independence on acoustic resonances of the crystal. It makes results of measurements repeatable enabling the tests and related measurements at different times to be made. Above that, selecting different pulses from the basic pulse train and comparing their magnitudes one can come to certain conclusions about physical mechanisms contributing to the insertion loss of the TIRUS. Figure 4.2.2 presents measurement results of three first pulses depending on time. A single transit loss value measured is 14.7 ± 0.2 dB for the first pulse, 23.4 ± 0.4 dB for the second and 25.4 ± 0.5 dB for the third pulses respectively. Comparison between these results leads to the conclusion that the sound attenuation is not the main reason for the observed total losses. Most probably, those can be caused by diffraction phenomena and mismatched positions of the transmitting and receiving transducers. From the measurements made however, nothing certain can be concluded about a character of possible losses connected with reflection of the probing pulse from the inclined face of the crystal except the evident fact that this reflection adds almost a half into the total value of measured losses of the TIRUS: actually, the insertion losses of loss samples having no inclined faces are ~8 dB whereas those of the TIRUS are ~15 dB.

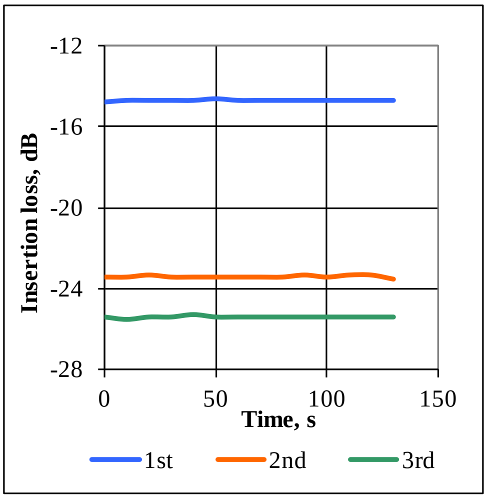

Fig. 4.2.2. Relative values of insertion losses for the 1st, 2nd and 3rd pulses of the basic pulse train.

5 Detection of a Subsurface "Flaw" with the TIRUS

The feasibility of the TIRUS has been proved in [1] in experiments with specimens having *surface* flaws, which were scratches on the surface of the specimens. In this section, the experimental data are presented on the TIRUS response to an artificial *subsurface* "defect" located at the depth of ~90 µm under the surface of a tested specimen. Experimental validation of the TIRUS capability to sense subsurface defects was performed by direct comparison of the sensor responses while being in contact with either a flawless or a defected specimen [2]. In this particular case, the specimen under test made of fused quartz was similar to that described in section 2.4.4, Fig 2.4.4.

The only strict requirement imposed on the design of the defected specimens tested in the current research is that the flaw should be located beneath the surface at the depth of about λ or less, where λ is the wavelength of the shear ultrasonic wave in fused quartz equal to 139 µm at 27 MHz. It does not matter for the testing purpose what kind of a "flaw" it is, a real subsurface discontinuity or inhomogeneity in a specimen of a homogeneous solid, or a simple foreign inclusion with acoustic properties different from those of the basic material. What does matter is its "right position" with respect to the surface of a tested specimen otherwise it will not affect the evanescent field under the incident ultrasonic beam footprint.

As mentioned in section 2.4.4, the technology on hand did not allow to make a defected specimen with a real discontinuity at such a depth therefore it was made as a combination of two pieces of fused quartz, a block and a thin plate, and a foreign inclusion between them. The plate was bonded to the block with epoxy resin that, in fact, has become "an artificial defect" in the experiments conducted.

After fabrication of the defected specimen, the ultimate thickness of the plate was ~90 µm that determined a depth at which the epoxy layer is located with respect to the surface of the specimen. The velocity of the shear wave in fused quartz is 3750 m/s that is far greater than $v_{\min}$=2190 m/s therefore the condition of total internal reflection is satisfied (see section 2.1). At the same time, the shear wave velocity in epoxy resin lies within the range of 1200÷1500 m/s that makes it be "a true defect of a foreign inclusion type" to be detected with the TIRUS.

In the experiments, the TIRUS sample Ug2 fabricated in [1] was used; the contact surfaces of both tested, the flawless and defected specimens, were polished and the specimens were placed in contact with the sensitive face of the sensor using a commonly used technique of optical contact.

A schematic of the sensor being in contact with the defected specimen is presented in Fig. 5.1 (*a*). The tested surface is a surface of the thin plate of fused quartz that is isolated from the block of the same material by the epoxy layer. The thickness of the epoxy layer, the "defect", is about 28 µm that, in a way, determines the thickness of the defect. That is, in this experiment a situation is emulated in which a very thin layer of a foreign material is embedded under the surface of a solid tested material.

Contacting surfaces of the sensor and a tested specimen were put together and a frequency response of the sensor being "in assembly" with the tested specimen was measured. The appearance of a produced "assembly" is presented in Fig. 5.1 (*b*). After fabrication of the specimen the thin quartz plate on its top surface had minor micro-cracks over a part of its area therefore the sensor was shifted to the part free of cracks. A zone of optical contact is located right under the footprint of the incident ultrasonic beam whose position is determined right

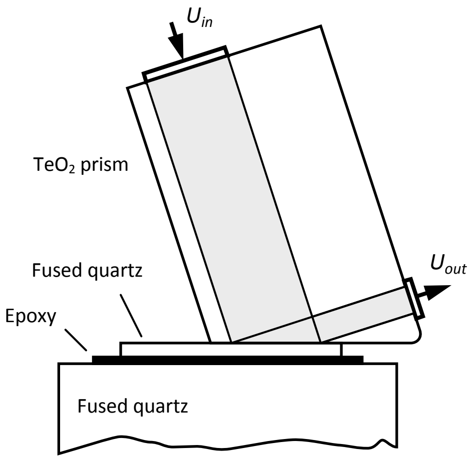

a

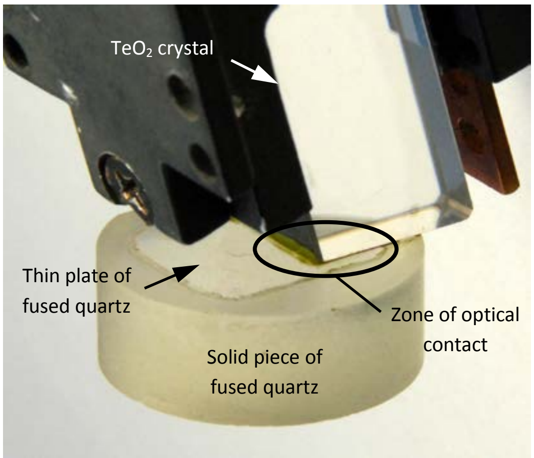

b

Fig. 5.1. Testing a defected specimen with the TIRUS. *a* – Schematic representation of the sensor in contact with a defected specimen (not to scale). A subsurface defect is created by a thin layer of epoxy located between two pieces of fused quartz. *b* – A picture of an experimental assembly. The sensor is placed in contact with the specimen surface using a technique of optical contact.

opposite the input transducer. While testing a flawless specimen, which was a block of fused quartz with a mirror-polished surface, the position of the sensor was chosen arbitrarily.

The insertion loss of the TIRUS was measured using a procedure described in Section 3.1. With a number of samples taken with the network analyzer equal to 401, a narrow 10 kHz frequency range chosen for measurement of the TIRUS response provided a good resolution equal to 25 Hz. At the same time, it was wide enough to observe acoustic resonances of the TeO_2 crystal that manifested itself as a wave on the frequency response (Fig. 5.2). As will be seen in section 6, an unstable position of this wave on the frequency scale observed in the experiments is connected with temperature instability of the acoustic resonator caused mainly by a large temperature coefficient of the slow shear wave velocity.

It is worth noting that the wave observed on the sensor response is particularly noticeable in the left dia-

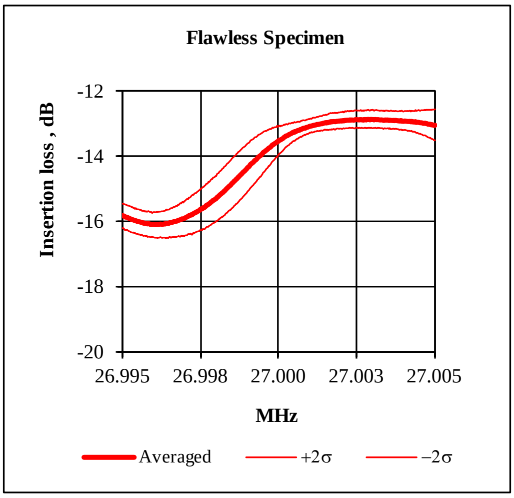

a

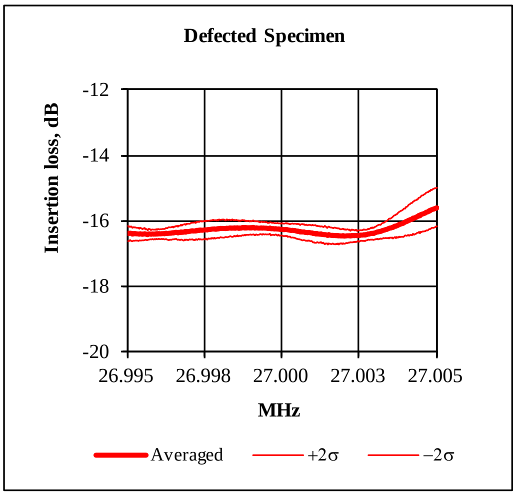

b

Fig. 5.2 Frequency response of the sensor to a flawless and a defected specimen. The response to the defected specimen is more even and manifests the insertion loss by a few decibels greater than that of the flawless one. $\pm 2\sigma$ lines determine a 95% confidence interval, σ stands for standard deviation.

gram depicting a response to the flawless specimen. At the same time, it is smoothed significantly in the right diagram representing a response to the defected one. It means that in the latter case an acoustic resonator formed by the TeO_2 crystal is damped by the specimen because the subsurface defect frustrates total internal reflection of the ultrasonic wave and a part of its energy emits from the crystal. It also leads to increase in an entire value of insertion loss of the sensor that is distinctively noticeable in comparison between the two diagrams: for the defected specimen it is by a few decibels greater than for the flawless one. Taking into account a small, ~28 μm, thickness of the defect one can infer that a potential sensitivity of the sensor might be expected high. Thus, the experimental results obtained show that the examined sensor responds unambiguously to a subsurface defect located within the evanescent field domain.

6 Testing the TIRUS Operational Capabilities in the Temperature Controllable Environment

Temperature instability of the TIRUS connected mainly with strong dependence of the slow shear wave velocity on temperature [1] results in an uncontrollable change in the resonant frequency of an acoustic resonator, which is the sensor body made of the TeO_2 crystal. This leads to significant variations in values of the sensor transfer function measured at different times. The TIRUS responds to the presence of a subsurface defect by a change in either its insertion loss or phase, or both. The temperature instability of the transfer function can mask a response from the tested specimen and make detection of a defect impossible.

Temperature controllable experiments produce data clear of temperature influence and thus easier to interpret. They were made using the TestEquity® temperature chamber TEC1. It is capable of maintaining a constant temperature within its workspace with precision of ±0.1°C and the temperature uniformity across it not worse than ±1°C. The temperature in the described experiments was chosen to be 20±0.1°C. In this section, all experiments regarding testing flawless or defective specimens were conducted using an optical contact technique that provides intimate contact between surfaces of the sensor and a tested object.

Experiments in temperature controllable environment were conducted using two measurement techniques, the continuous wave and time-gated ones, described in sections 3 and 4. In the continues wave measurements were made in the frequency band of 40 kHz with the central frequency of 27 MHz; only the insertion loss of the sensor was measured. In the time-gated measurements both the insertion loss and phase of the transfer function were measured at the frequency 27 MHz.

6.1 The TIRUS Samples Examined and Specimens Tested

The TIRUS samples studied in temperature controllable experiments were Uj4, Ug2 and Ug2_2. The sample Uj4 is the one investigated in the previous sections. As to the Ug2 and Ug2_2 samples, more information on their design is presented in section 2.3. The sample Ug2_2 is a new one fabricated in the course of the current project from the sample Ug2 that was damaged in the experiments with a defective specimen identified in the current report as specimen D1. It was a specimen of the same type as used in [2]: an artificial flaw was an epoxy layer of about 50 µm in thickness that bonded a thin (~60 µm) plate of fused quartz to a block of it. The top surface of the plate was polished thoroughly and optically flat that enabled to provide an optical contact with a sensitive surface of the sensor.

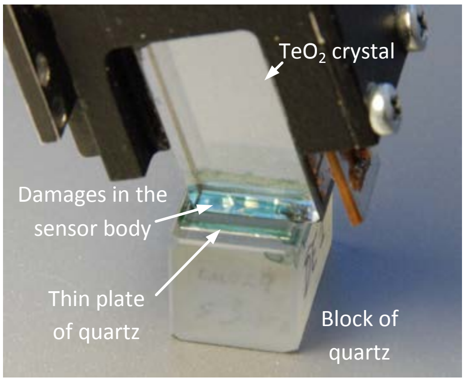

Fig. 6.1.1. The TIRUS sample Ug2 bonded to a defective specimen using an optical contact technique. One can see damages under the sensitive surface of the sensor.

The assembly of the sample Ug2 with the defective specimen D1 is shown in Fig. 6.1.1. The damages under the sensitive surface of the sensor were discovered in the end of measurements of the TIRUS output $IL(f)$ therefore the results of experiments with it cannot be accepted as conclusive. Nevertheless, they can illustrate a common tendency of increase in an insertion loss of the sensor when total internal reflection of the ultrasonic wave is frustrated for whatever reason. The sample Ug2_2 was fabricated by means of grinding the damaged layer of the Ug2 crystal and consequent polishing of the crystal sensitive surface.

6.2 Continuous Wave Technique

The measurement procedure for continuous wave studies is described in section 3.1 therefore only the obtained results are presented here. In the experiments, both insertion losses and phases of transfer functions were measured in the frequency range of 50 kHz. This range was wide enough to observe a few acoustic resonances of the TIRUS crystal. At the same time, the frequency resolution of 125 Hz achieved with 400 frequency samples taken in a single individual measurement was good enough to observe tiny changes in the frequency characteristics of the insertion loss *IL*(*f*) treated as a sensor output.

All measurements in this section were made using the temperature chamber except the one, results of which are presented in Fig. 6.2.4 on the next page. Prior to a measurement, a unit under test was kept in the chamber for 30 minutes, after which time it had a steady-state temperature of 20°C, and at this point measurements were taken. In such a way, all temperature influences on the results of experiments were excluded and results obtained on different days could be compared and interpreted properly. As a result, some facts were established having a direct relation not to the TIRUS samples or to the specimens properties but rather to the nature of an optical contact itself.

This is illustrated in Figs. 6.2.1 and 6.2.2: maximum suppression of acoustic resonances of the TIRUS crystal is observed immediately after setting a tested specimen on an optical contact (red line); the same is with the measured insertion loss that is greater by a few dB. It says that the quality of the optical contact is the best at the beginning, which leads to the greater amount of the ultrasonic beam energy being penetrated through the interface because of frustrated total internal reflection. Then its quality declines going to a steady state in the following days. The similar effects were observed in experiments with samples Uj4 and Ug2_2. The most impressive results were obtained in the case of the Uj4 sample (Fig. 6.2.2). Bearing in mind these effects, further, whenever it is possible, results will be presented of the earliest measurement series taken immediately after set-

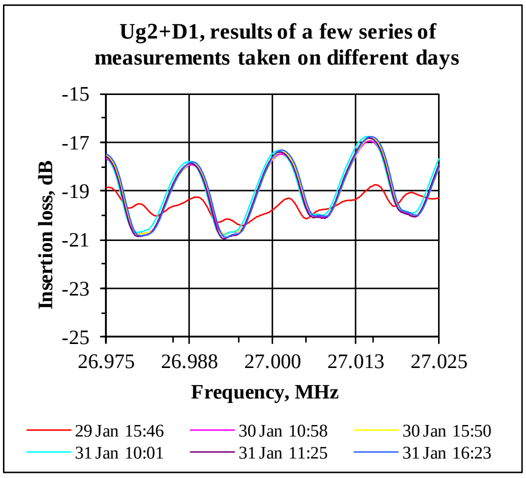

Fig. 6.2.1. Change in characteristics of the assembly Ug2+D1 in time. The greatest suppression of acoustic resonances of the TIRUS crystal is observed at the first measurement taken immediately after making the assembly on Jan 29, 2014.

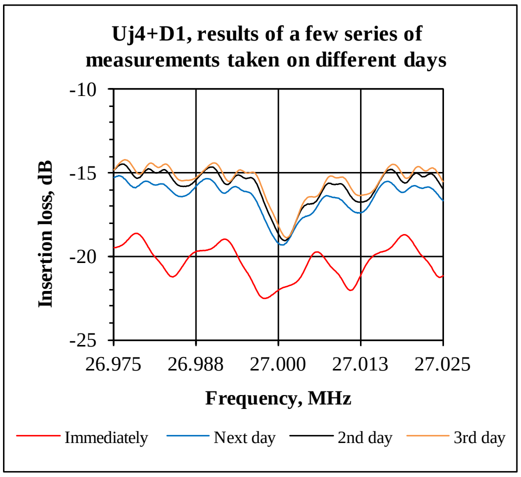

Fig. 6.2.2. Change in characteristics of the assembly Uj4+D1 in time. The greatest suppression of acoustic resonances of the TIRUS crystal is observed at the first measurement taken immediately after setting D1 on an optical contact.

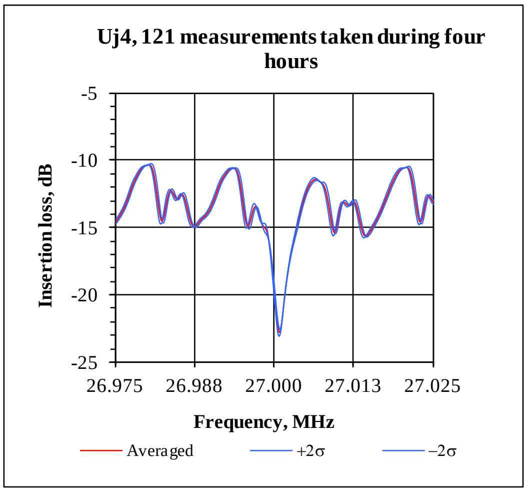

Fig. 6.2.3. Insertion losses of the sample Uj4 measured at 20± 0.1°C. Thin blue lines determine a 95% confidence interval, ±2σ@27 MHz=0.93 dB.

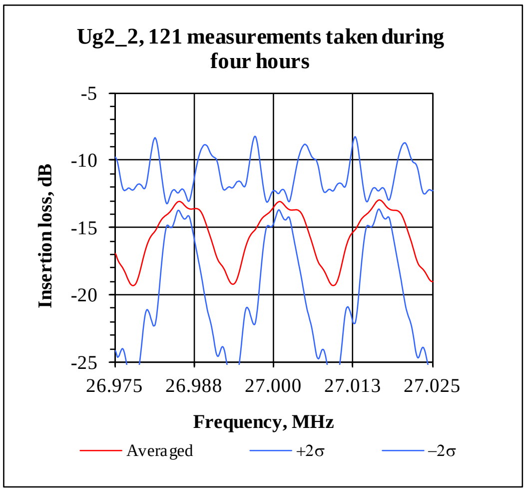

Fig. 6.2.4. Insertion losses of the sample Ug2_2 measured in a temperature uncontrollable environment. Thin blue lines determine a 95% confidence interval, ±2σ@27 MHz=2.35 dB.

ting a tested specimen on an optical contact.

An important advantage of making measurements using the temperature chamber is that there is no necessity in applying a complicated post-processing procedure for data obtained because dispersion of the acquired data proves to be very small (see Fig. 6.2.3). An example of the sample Uj4 shows that the value of the ±2σ interval, where σ is standard deviation, is equal only to 0.93 dB even at the frequency of 27 MHz where the slope of the characteristic *IL*(*f*) is very steep. In the vast majority of cases, it is as small as $0.05 - 0.1$ dB. On the contrary, dispersion of data obtained in the temperature uncontrollable experiments is greater by orders of magnitude (see Fig. 6.2.4).

Sensitive properties of the TIRUS can be estimated by comparison of insertion losses measured in the case of no tested specimens attached to the sensor crystal with the cases when either flawless or defective specimens are attached to it. Because dispersion of the data obtained in all experiments with the temperature chamber is small, hereafter no confidence intervals but only the means of the series of measurement will be presented in the diagrams illustrating effects caused by the tested specimens.

The procedures for getting data on TIRUS capabilities to sense an artificial defect under the surface of the tested specimen were the same for all three sensors studied. At the beginning, a series of insertion loss measurements of the sensor itself was made. As a rule, it was a short series with 6 records of frequency characteristics *IL*(*f*) taken within a 10 min interval. Then the same series of measurements were made with either the defective or flawless specimens attached to the sensitive surface of the sensor using an optical contact technology. The flawless specimen was a block of fused quartz of the same shape and size as the defective specimen D1 but with no thin plate and epoxy layer on its polished surface.

The expected result while testing the defective specimen was an increase in a measured value of the insertion loss (its absolute value) and suppression of acoustic resonances of the crystal. These effects were expected because they should be a manifestation of frustrated total internal reflection of an ultrasonic wave incident at the interface. On the contrary, there should not be any such effects in the experiments with flawless specimens. In

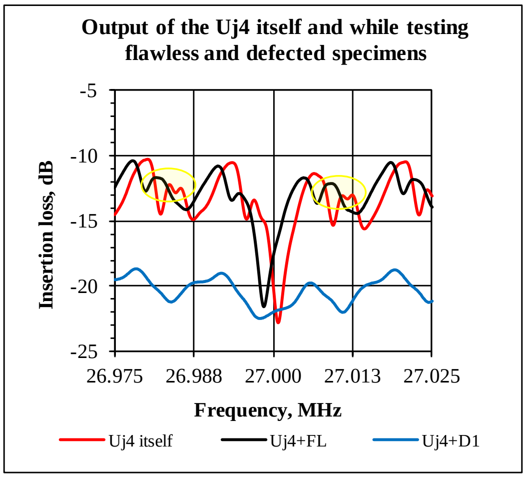

Fig. 6.2.5. Change in the Uj4 output caused by a tested specimen, flawless (FL) or defective (D1). Yellow ovals show zones of tiny differences between shapes of red and black lines.

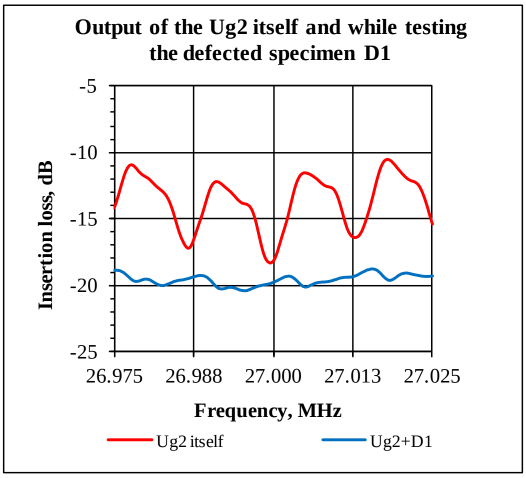

Fig. 6.2.6. Change in the Ug2 output caused by a tested defective specimen D1.

this case, total internal reflection is not frustrated and hence the TIRUS output should not differ from the output of the sensor with a free sensitive surface. As seen from Figs 6.2.5-6.2.7 presenting results of testing using three TIRUS samples, it was not always so.

For the sensors Uj4 and Ug2_2, the presented results were obtained while testing both the flawless (FL) and the defective (D1) specimens. For the sensor Ug2, however, the results were obtained while testing only the defective specimen. This is connected with the fact that sensor Ug2 was damaged in experiments with the defective specimen D1 and no experiments with the flawless one have been carried out.

Analysis of the sensors outputs *IL*(*f*) presented in the figures shows that the presence of a subsurface defect in a tested specimen results in an evident increase in the value of the insertion losses in all cases (blue lines), independently on the shape of the output frequency characteristic. Acoustic resonances are also suppressed. That is, all three sensors respond to the presence of a defect unambiguously in complete accordance with the expected reaction.

In the case of testing flawless specimens, the situation looks different. As to the Uj4 sensor (Fig. 6.2.5), the results obtained are very close to the expected ones. The measured characteristics (red and black lines) almost coincide except tiny differences in their shape and a small shift on the frequency scale. The latter can result from some temperature non-uniformity in the temperature chamber, which according to its specification can reach up to ±1°C.

It is much more difficult to explain clear, although tiny, differences between the shapes of characteristics in zones marked with yellow ellipses: the sensor output looks smoother when the flawless specimen is attached to its sensitive surface than with no specimen. Moreover, in this case, it looks having a bit less, although insignificantly, value of the insertion loss. Similar effects are also observed for the Ug2_2 sensor (Fig. 6.2.7) but in this case, the decrease in the insertion loss is much more evident. For the time being, there is no explanation for these effects but one can assume that they are connected with possible transformations of acoustic modes at the boundaries of the crystal, which can be partly suppressed by an attached flawless specimen. A change in the

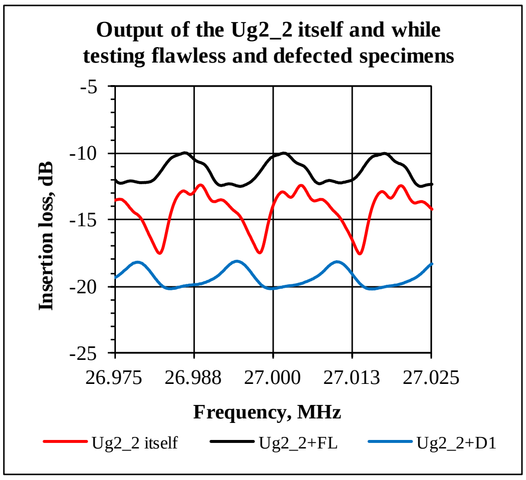

Fig. 6.2.7. Change in the Ug2_2 output caused by a tested specimen, flawless (FL) or defective (D1).

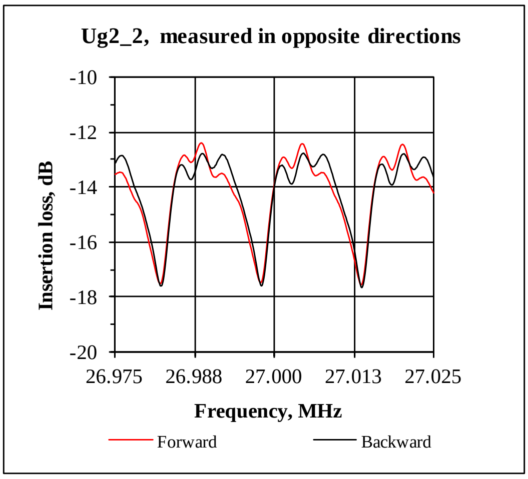

Fig. 6.2.8. Insertion losses of the TIRUS sample Ug2_2 measured in the opposite directions.

stress state of the sensitive surface of the crystal caused by the attached specimen cannot also be excluded from consideration, though. One also need to remember that samples Uj4 and Ug2_2 have different geometry (sizes) of the transducers on the top face of the crystal and the crystal of the latter is shorter by a few millimeters because of being refurbished. This changes the acoustic field distribution on the reflecting surface of the crystal. Anyway, the observed effect requires special investigations.

Another effect revealed in experiments with the temperature chamber is a small but evident difference between the TIRUS frequency characteristics measured in the cases of propagation of an ultrasonic wave in the opposite directions (Fig. 6.2.8). In these experiments, an examined sensor was not even taken off from the chamber; the connecting cables were simply interchanged between the source and the receiving parts of the measurement instrument that ensures the results obtained to be very reliable. The “forward direction” in Fig. 6.2.8 means that an ultrasonic wave is radiated by the side transducer into the [110] direction and is received by the top transducer on the (001) face of the crystal. The “backward direction” means that the emitting and receiving transducers are reversed. In this case, the observed difference is apparently connected with different “wave distances” (distances expressed in wavelengths) between a transmitting transducer and a reflecting inclined face of the crystal. Because the propagation distances in the crystal do not exceed a size of the Fresnel zone, it does matter.

Thus, the continues wave technique being used in the temperature controllable environment proved to be a sensitive instrument capable of revealing tiny changes in the TIRUS characteristics caused by specific features of wave processes in the sensor body.

6.3 Time Gated Technique

Time-gated measurements of insertion losses IL_{TG} were carried out with the phase meter specially developed for this purpose. Previous experience (see Appendix A and section 4) of operation with the phase meter had shown that the length of the pulse trains in the TIRUS crystals had been greater than 255 µs, the value initially chosen as an unalterable parameter of the phase meter. Therefore, the device was improved for it to be 1023 µs. Trial measurements showed that during this time the amplitude of pulses decreased down to the background noise of the measurement system (-60 dB). A schematic of the phase meter was also modified that enabled temperature stability of the amplitude measurement channel to be improved up to 0.1 dB.

As far as in time gated measurements acoustic resonances of the crystal are avoided, experiments in a temperature controllable environment were carried out as a part of the whole set of time gated studies of TIRUS responses to flawless and defective specimens. Tested specimens were set on the sensitive surface of the sensors using an optical contact technology. All measurements were carried out at the frequency of 27 MHz.

Measurements of amplitudes and phases of basic (i.e., first delayed) pulses were made within ten-minute periods of time. Measured basic and subsequent pulses were also observed and analyzed with the oscilloscope Tektronix TDS2022 whose input was connected to the RSSI output of the phase meter proportional to the logarithm of the output pulse amplitude. A measured value of a spurious continuous wave signal in the intervals between pulses was -50 dB with respect to the first pulse amplitude. Assessment of errors caused by this spurious signal gave a measure of measurement inaccuracy not worse than 0.2 dB when amplitudes of small measured pulses were greater than -27 dB.

The basic group of experiments including testing both flawless and defective specimens was carried out with TIRUS samples Uj4 and Ug2_2. The sample Ug2 was damaged while testing a defective specimen therefore in its case no results of experiments with a flawless specimen were obtained. A few series of measurements included initial measurements of the TIRUS itself and successive measurements of its output while testing either flawless or defective specimens. In all cases, the measurements were done with the sensor operating in both the forward and the backward directions. (What does it mean is explained in the previous section. Data obtained in experiments with the sensors themselves were further used as the reference ones.

Table 6.3.1. Results of testing flawless and defective specimens.

TIRUS sample	Direction of signal propagation	Insertion loss with no specimen, dB	Insertion loss with a flawless specimen, dB	Insertion loss with a defective specimen, dB	Insertion loss added by a defect, dB
Uj4 [1)]	forward	13.8	13.8	22.9	9.1
Ug2_2 [2)]		14.1	11.2	19.0	7.8
Uj4 [1)]	backward	16.3	16.6	25.6	9.0
Ug2_2 [2)]		14.3	11.4	19.1	7.7

[1)] Temperature uncontrollable environment; [2)] t°=20±0.1°C.

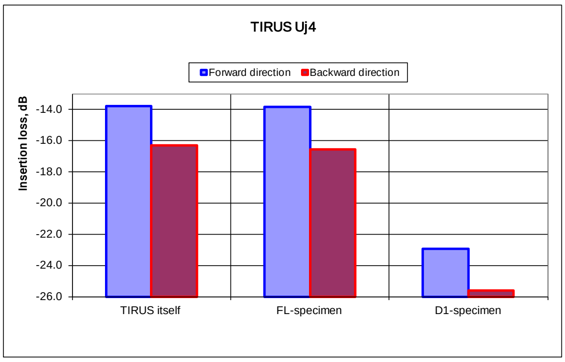

Fig. 6.3.1. Time-gated outputs of sample Uj4 while testing flawless (FL) and defective (D1) specimens. Temperature uncontrollable environment.

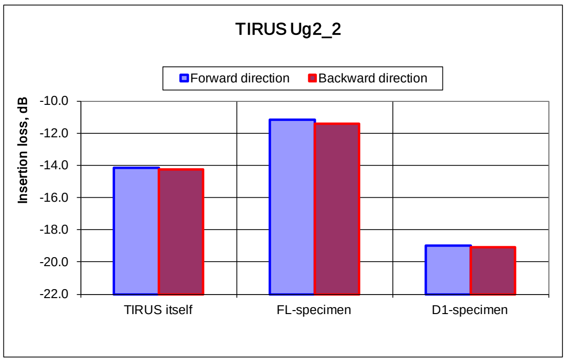

Fig. 6.3.2. Time-gated outputs of sample Ug2_2 while testing flawless (FL) and defective (D1) specimens. Temperature controllable environment, t°=20±0.1°C.

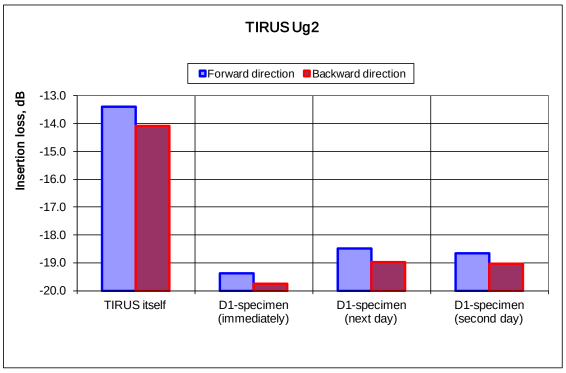

Fig. 6.3.3. Change in time of time-gated outputs of sample Ug2 while testing a defective specimen (D1). Temperature uncontrollable environment.

Results of experiments with samples Uj4 and Ug2_2 are collected in Table 6.3.1 and illustrated in Figs. 6.3.1-6.3.3. Analysis of the presented data shows that responses from the investigated samples to the presence of a subsurface defect are similar: insertion losses increase evidently and significantly, what says unambiguously about frustration of total internal reflection of the probing ultrasonic wave. Thus, these results completely coincide with the expected ones.

On the contrary, results obtained while testing flawless specimens are contradictory. Experiments with Uj4 produced “right” results: measured values of insertion losses of the sensor itself and of that attached to the flawless specimen are very close to each other. The Ug2_2 sample produced a “wrong” result, not very surprising though: insertion losses with the flawless specimen were significantly less than those of the TIRUS itself. This is virtually the same results as obtained in the continuous wave studies. It is also worth noting that similar results were obtained in the earlier research [1]. Some discussion of possible nature of these effects are given in the previous section. They can hardly be connected with the fact that the Ug2_2 sample was tested in the temperature chamber because the sample Ug2_2 is the repaired sample Ug2, for which similar results were obtained in [1] in the temperature uncontrollable environment.

In experiments with sample Ug2 the defective specimen D1 was tested repeatedly during a few successive days in a temperature uncontrollable environment. First measurements were made immediately after setting it on an optical contact and showed a significant (by 6 dB in the forward direction and by 5.7 dB in the backward one) increase in insertion losses. Similar measurements made on the next day gave the insertion loss value less by ~0.8 dB and further stayed the same (see Fig. 6.3.3). That is, the observed effect, which can be called “stabilization of an optical contact”, was very similar to that observed in the continuous wave studies (see Fig. 6.2.2)

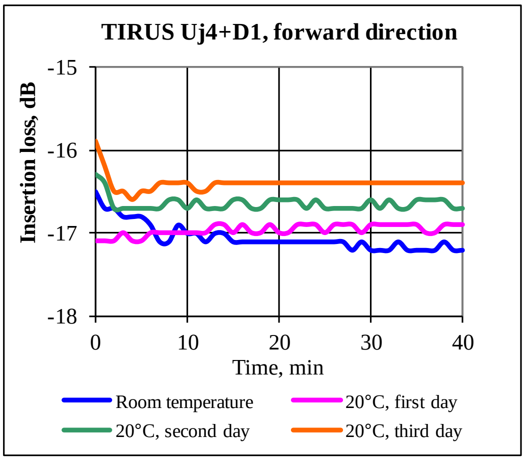

Fig. 6.3.4. Testing of the defective specimen D1 with the Uj4: change in time of the time-gated insertion loss. Temperature controllable and uncontrollable environments.

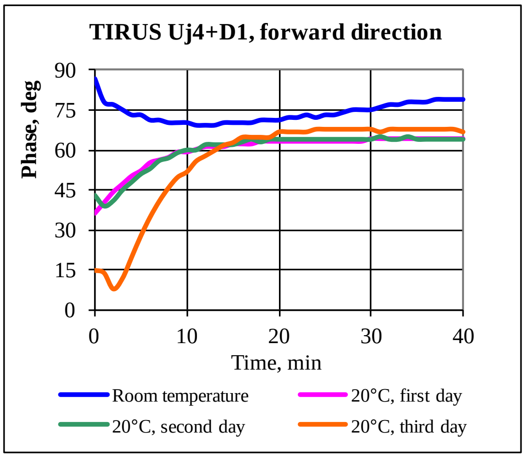

Fig. 6.3.5. Testing of the defective specimen D1 with the Uj4: change in time of the time-gated phase. Temperature controllable and uncontrollable environments.

but with a much less quantitative change in the insertion loss value. Nevertheless, the change caused by the presence of a subsurface defect is large enough (~5-6 dB) to detect it reliably.

Experiments specially aimed at verifying reproducibility of the results of successive individual measurements in a temperature controllable environment were conducted with sample Uj4. Series of measurements were carried out on successive days within 40 min periods with individual measurements taken over 1 min intervals. Both the magnitude ("insertion loss") and the phase of the time gated transfer function T_{TG} were measured in forward and backward directions. The measurements were made at 20°C using the temperature chamber and at a room ("normal") temperature that was an uncontrolled temperature in the laboratory.

Results of measurements made in the forward direction are presented in Figures 6.3.4-6.3.5. Results of measurements made in the backward direction are similar although an absolute value of the insertion loss is by ~3 dB greater than that in the forward direction.

The difference between the steady-state insertion loss values in Fig. 6.3.4 and those presented in Table 6.3.1 is connected with degradation of an optical contact within a first day after mounting of the defective specimen on the sensor. (Data in the Table 6.3.1 were obtained immediately after the mounting). In principle, as seen in Fig. 6.3.4, insignificant degradation of the optical contact continued also within next days that resulted in decrease in the insertion loss value with a speed of about 0.2 dB/day.

Comparative analysis of data presented in Figures 6.3.4-6.3.5 shows that in a short time (less than 15 min) both the insertion loss and the phase values are stabilized and stay constant in different series of measurements. The close values obtained in "normal" and temperature controllable conditions are connected with the fact that the temperature in the laboratory at the moment of measurements was close to 20°C. From this, one can infer that testing specimens with a pulse measurement system (i.e., the phase meter developed) can be carried out in normal laboratory conditions not using a temperature chamber.

7 Testing Specimens with the TIRUS Using a "Sliding Technique"

7.1 Method and a specimen used

In the majority of actual testing procedure ultrasonic sensors are applied to a surface of tested objects through a fluid couplant[1], in which case the sensor can move, or "slide", across the surface of the inspected material. In this section, such a procedure further called a "sliding technique" is described. In the experiments, it was applied to testing a defected specimen of a specific type. The idea behind these experiments was to inspect a defected specimen that had already been examined in sections 3 and 4 using an optical contact technique but in a way enabling to move the sensor sequentially over a flawless part of it, then over its defected part, and then again over its flawless part, but another one, in the end. It was supposed to emulate an actual inspection procedure and to enable to compare the sensor responses from flawless and defected domains of the tested specimen acquired in one experiment.

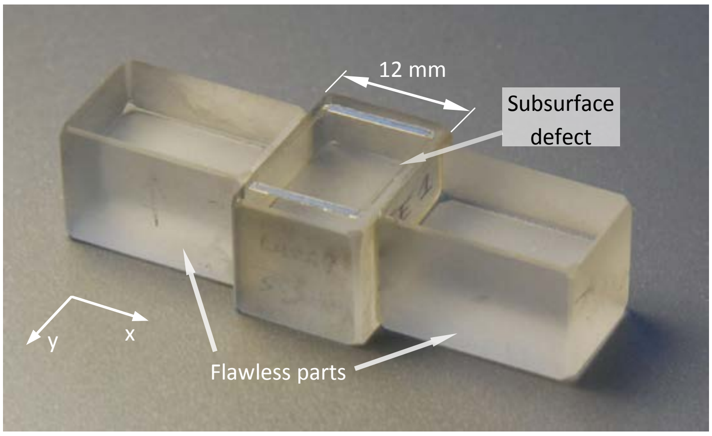

Fig. 7.1.1. The specimen "D1+" tested in the sliding technique experiments. It is an assembly of three specimens of fused quartz, two flawless and one defected.

The specimen fabricated for this purpose was made as an assembly of three specimens (Fig. 7.1.1), a defected one denoted as D1 in section 6.1 and two flawless ones bonded to its side surfaces. (Further it will be denoted as specimen "D1+"). The defected part of the specimen was of a "subsurface foreign layer" type similar to one described in [2]. The tested surface was a surface of a thin plate of fused quartz that was isolated from the block of the same material by an epoxy layer. The thickness of the epoxy layer, the "defect", was about 50 μm that was determined by the thickness of metal strips under the edges of the quartz plate applied in the fabrication process. The ultimate thickness of the quartz plate was ~60 μm. That is, in this experiment a situation was emulated in which a very thin layer (50 μm) of a foreign material is embedded under the surface of a solid tested material.

The flawless specimens were bonded to the side faces of the defected one with a glue. Upper faces of all three specimens were polished thoroughly and made optically flat before assembly and then thoroughly aligned while specimens were bonded. The resulting specimen was then tested by means of a sliding movement of the TIRUS along the *x*-direction (see Fig. 7.1.1) across the entire surface of the fabricated assembly. In such a procedure, an expected TIRUS output was supposed to be a response essentially different in its middle part that might be expressed in a significant increase in insertion losses measured. In the experiments, the insertion losses were measured using the continuous wave (CW) and time-gated (TG) techniques described in sections 3 and 4.

A specific feature of the fabricated combined specimen is that its tested surface is not absolutely even. The *x*-size of its "defective specimen part" is 12 mm (see Fig. 7.1.1) whereas that of the quartz plate bonded to the

[1] A substance used to provide acoustic coupling between surfaces of the sensor and a tested object.

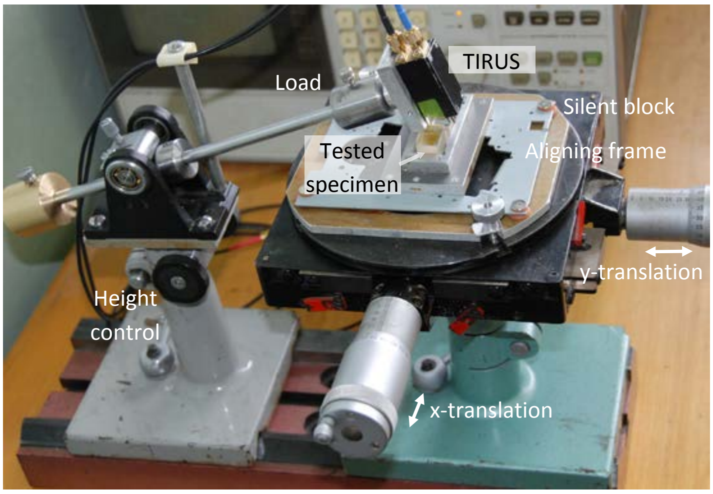

Fig. 7.1.2. The sliding mechanism used in the experiments. It provides smooth movement of the specimen with respect to the TIRUS and alignment of their contacting surfaces. The yellow-brownish substance on the upper surface of the specimen is the Sonotech Shear Gel® couplant.

quartz block with epoxy resin (see section 2.4.4, Fig. 2.4.4) is only 9mm. There are also chamfers on the edges of each of three quartz blocks constituting the specimen imaged in Fig. 7.1.1. Together with 60 µm steps on the edges of the quartz plate they form grooves of ~1.5 mm in width between the defective and flawless parts of the specimen. As will be seen in section 7.3, these grooves can cause responses from the TIRUS in testing the specimen.

A mechanism constructed for experiments is shown in Fig. 7.1.2. It consists of three main parts. A 2-axis translation stage on the right provides not only very smooth movement of a tested specimen along the *x*-direction but also enables the specimen to be positioned accurately with respect to the TIRUS in the *y*-direction.

A height-controlled balance on the left enables to lift the TIRUS and in such a way to align its sensitive surface with respect to the tested surface of the specimen. An ultimate alignment is provided by an aligning frame connected to the translation stage through four soft silent blocks. The TIRUS is pressed to the surface of the tested specimen with two controlled loads on the opposite ends of the balance. All the experiments using the sliding technique were carried out with two couplants, the Sonotech Shear Gel® and glycerin. The TIRUS sample used in the experiments was the refurbished sample Ug2_2 (see section 2.3).

7.2 Continuous Wave Experiments

In the sliding technique experiments, continuous wave measurements were conducted in a slightly different way than in previous experiments using the optical contact technique. Insertion losses of the TIRUS were measured exactly at its operating frequency of 27 MHz and not within the frequency range of 50 kHz around it. The measurements were taken each 10 s at the moments when the sensor was stopped at certain sequential positions on the tested specimen surface that moved in the *x*-direction (Fig. 7.1.1). The translation of the specimen was performed manually with the translation stage, the sequential step lengths were 1 mm; the sensor positions were fixed. The load from the sensor measured on the surface of the specimen was 300 g. This load enabled to get rather good alignment of the sensor and the specimen surfaces that can be seen from behavior of silent blocks attaching the aligning frame to the translation stage (see Fig.7.1.2).

As far as the sliding technique implies the use of a couplant between contacting surfaces of the sensor and a tested specimen, two couplants were used in all the experiments, glycerin and the Sonotech Shear Gel. All the experiments were carried out with the same TIRUS sample, Ug2_2, and specimen D1+ (see Fig.7.1.1). The load applied to the sensor pressed out a couplant from under the sensor rather well but there was no control of its

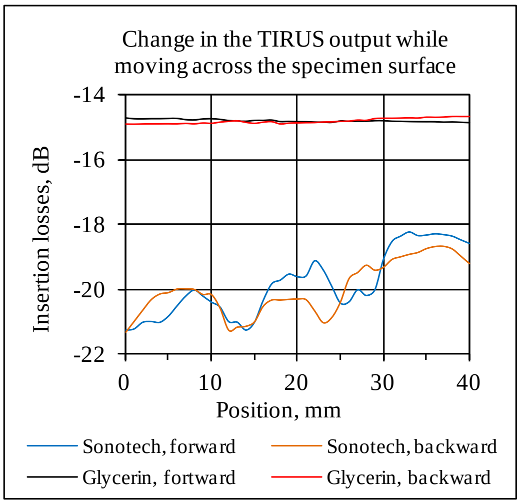

Fig. 7.2.1. Change in the TIRUS output $IL(x)$ while testing a specimen with different couplants, the Sonotech Shear Gel or glycerin. "Forward" and "backward" mean "positive" (0 to 40 mm) or "negative" (40 to 0 mm) directions of movement.

layer thickness. Measurements using each of two couplants were carried out in three series of two pairs of forward and backward passes across the specimen surface along the x-direction. In each series, the surfaces of the TIRUS and the specimen were cleaned up thoroughly and a new portion of the couplant was deposited on them. All the measurements were carried out in normal laboratory conditions. No temperature control was applied but occasional monitoring of the temperature in the room showed that it was in the range of 18-22 °C. In such a manner, six characteristics $IL(x)$ were obtained for each of the couplant, where IL stands for the TIRUS output, the insertion loss.

Each six of the obtained characteristics were averaged and the averaged results are presented in Fig. 7.2.1. The dispersion of the results is illustrated by Table 7.2.1 where standard deviations of data acquired are presented. As seen in the figure and in the table, in both cases there is nothing certain that can be inferred from the averaged $IL(x)$ characteristics about the presence or absence of a subsurface defect. An expected response of the TIRUS with both couplants applied should have been a significant dip in the middle of them that would have indicated frustrated total internal reflection at the interface of the structure sensor-couplant-specimen. It was not observed for both couplants, although both the shapes of the measured characteristics and values of $IL(x)$ were very different.

In the case of glycerin, measurements taken when passing forward and backward across the specimen resulted in practically identical even characteristics with no dip in the middle. The averaged values of the insertion losses were -14.8±1.26 dB for forward and -14.9±1.42 dB for backward directions with the 95% confidence interval defined as ±2σ. They exceed the insertion loss value of the sensor itself measured at 27 MHz at 20° C, which was -13.3±0.13 dB, by 1.5 dB. This difference can be considered small or even insignificant taking into account differences in temperatures at which the measurements were taken. Thus, one can conclude that the sensor, in fact, did not sense the tested specimen at all and the glycerin layer served as an isolating one that did not practically affect the incident ultrasonic wave in the sensor body, or, perhaps, slightly absorbed it at the boundary of the crystal.

Table 7.2.1. Dispersion of the TIRUS output $IL(x)$ while testing the specimen D1+ with different couplants.

Couplant/Movement	**Insertion loss, dB; averaged, x=20 mm**	**Standard deviation σ, dB**	
		$\sigma_{20\ mm}$	σ_{max}
Sensor Ug2_2 itself[1)]	-13.3	0.066	–
Sonotech/Forward	-19.6	1.29	3.43
Sonotech/Backward	-20.3	1.51	2.66
Glycerin/ Forward	-14.8	0.63	0.80
Glycerin/Backward	-14.9	0.71	0.84

[1)]No couplant, no tested specimen, measured at 27 MHz at 20°C

In the case of the Sonotech Shear Gel, the picture was much more complicated. As is seen from Fig. 7.2.1, both characteristics corresponding to forward and backward movements have fairly similar, although a

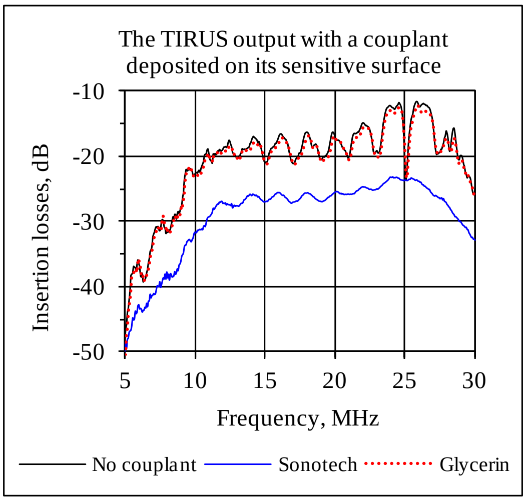

Fig. 7.2.2. Insertion losses vs frequency *IL*(*f*) measured with different couplants, the Sonotech Shear Gel or glycerin, deposited on the TIRUS sensitive surface. Measurements are taken at 20°C within a very wide frequency range.

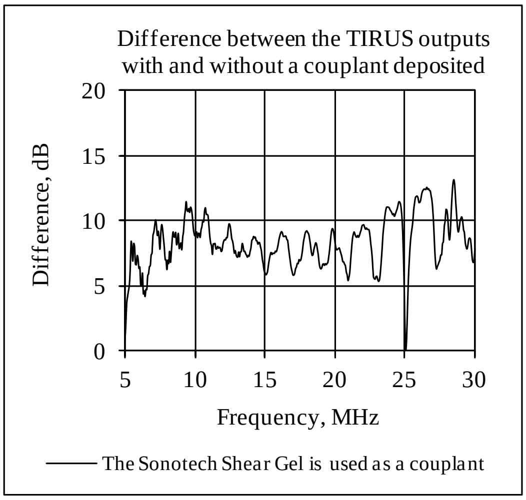

Fig. 7.2.3. The difference between the TIRUS outputs (insertion losses) with and without a couplant deposited on the TIRUS sensitive surface. A clear trend of its decrease at frequencies lower 10 MHz is visible.

little shifted to each other, shapes. This similarity shows that the results obtained are not of a random character and both characteristics have similar trends but there could hardly be a reasonable explanation for these trends in terms of subsurface defects in the specimen. It might rather be connected with extremely large viscosity of the Sonotech Shear Gel that could lead to uneven motion and forming a wavy profile of the gel layer. The only fact that the observed curves evidently indicate is that the ultrasonic wave incident at the crystal-gel interface does penetrate into the gel layer and certainly does not reflect back from the gel-specimen interface, which follows from a significant increase in the insertion loss measured, up to 8 dB compared to that of the sensor itself.

The observed effects raised the question of actual influence of the couplants on the results of experiments. The manufacturer of the Sonotech Shear Gel does not give any information on actual operating characteristics of it in different frequency ranges. Therefore, trial experiments were conducted using sensor Ug2_2 as a testing instrument. The idea behind these experiments was to exploit the sensor in a wide frequency range and study behavior of the couplants within it. The experiments were carried out within the range of 5-30 MHz. Despite the fact that the sensor had been constructed as a narrow-band device with the operating frequency f_0=27 MHz and its efficiency was much worse outside the frequency range of 26-28 MHz, it still operated almost everywhere over the range of interest. All the measurements were done at 20±0.1°C using a temperature chamber to provide a good repeatability of the results.

The results obtained are presented in Fig. 7.2.2. The first one obviously seen from the figure is that the insertion losses *IL*(*f*) of the TIRUS measured with glycerin deposited on its sensitive surface and without it are practically coincide. It does not necessarily mean that the incident ultrasonic wave in the sensor body is completely reflected from the crystal-glycerin interface. It might also mean that the sound attenuation in glycerin is so small that the wave penetrated into the glycerin layer does not decay there at all and returns into the crystal undamped. As was seen above, it was not so in experiments using the sliding technique (see Table 7.2.1) where insertion losses with glycerin as a couplant were by ~1.5 dB greater than those in the sensor itself. From that, one could have concluded erroneously that a scattering by a defect in the specimen of an evanescent ultrasonic wave tunneling through the glycerin layer was a proven fact if exactly the same increase in the insertion losses had not been observed over the whole surface of the specimen (see Fig. 7.2.1), including its flawless parts. That is, the sensor responded to flawless and defected parts of the specimen identically. Thus, a real reason for these greater insertion losses stays unclear. (Although one can try to explain it by different temperature conditions in the sliding technique experiments).

The origin of the observed deep dip (-23.6 dB) on the characteristics in Fig. 7.2.2 is also unclear. Apparently, it is connected with a specific properties of the frequency characteristic of the total system consisting of the transducer, an acoustic resonator, which is the sensor body, and a matching network: together they form an electro-mechanical filter with a notch at the frequency of 25.063 MHz.

The behavior of the Sonotech Shear Gel was essentially different. The presence of the gel suppressed the wave reflected from the crystal-gel interface evidently putting down the measured frequency characteristic $IL(f)$. It means that the probing ultrasonic wave from the sensor body penetrated into the gel layer and decayed there significantly. The path of the smoothed suppressed characteristic over the frequency range was almost parallel to the path of the sensor characteristic with one tiny but important exception: the suppression value, i.e., the difference between values of measured insertion losses of the sensor with and without a couplant (Fig. 7.2.3) tended to decrease at frequencies lower 10 MHz with almost negligible difference near 5 MHz. That is, at 5 MHz the probing ultrasonic wave that penetrated into the gel layer propagated in it without any decrease and then returned to the crystal undamped. Thus, the Sonotech Shear Gel can be considered as a suitable couplant only at frequencies much lower that the operating frequency of the developed sensor, 27 MHz, apparently at frequencies lower than 10 MHz.

7.3 Time Gated Experiments

Measurements of time gated insertion losses $IL_{TG}(x)$ of the TIRUS were carried out with the same phase meter that was used in section 4, the frequency of the probing pulse carrier was 27 MHz, its duration was 5 µs. The TIRUS sample was the same that was used in the CW experiments, the Ug2_2. The defected specimen D1+ and the sliding technique itself used in the experiments are described in detail in section 7.1.

The measurements were conducted by moving the specimen with respect to the sensor step by step in a quasi-static manner: one measurement taking procedure lasted for 10 s and was divided into two stages with the first one characterizing by the specimen movement. It started at the 3rd second after taking a previous measurement and finished at the 6th second, so 4 seconds were left to stabilize the contact. Because movement of the specimen was performed manually, the initial 3 “empty” seconds were left for comfort of the operator. All the measurements were conducted in the normal laboratory conditions. The load from the sensor applied to the specimen surface was 330 g.

The main drawback of the applied technique in experiments with the Sonotech Shear Gel® used as a couplant was rather unstable contact between the TIRUS sensitive surface and that of the moving tested specimen. It was connected with insufficient rigidity of the balance holder (see Fig. 7.1.2) and with rather significant change in properties of the couplant during a single measurement operation that resulted in a visible difference between results obtained when moving in forward (0-40 mm) or backward (40-0 mm) directions. The measurements were done during one day in six series of forward-backward pair passes across the specimen surface along the *x*-direction. However, only the results are presented here obtained in the forward movement of the

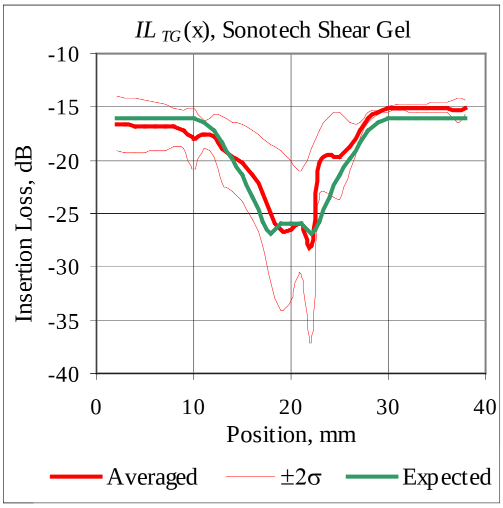

Fig. 7.3.1. Averaged time-gated insertion loss IL_{TG} of the TIRUS vs the sensor position x. The Sonotech Shear Gel used as a couplant; the forward motion (0 to 40 mm). The ±2σ lines show the 95% confidence limits.

TIRUS because in this case repeatability of obtained results was for unknown reason significantly better than in the backward movement.

Averaged results of 6 individual measurements of $IL_{TG}(x)$ taken when moving in the forward direction are presented in Fig. 7.3.1; the thin red ±2σ lines show the 95% confidence limits; green line shows insertion losses expected to be obtained in the experiment. As seen in the figure, measured insertion losses (thick red line) in the area where there exists a subsurface defect are up to 10 dB greater than those in the flawless area. It is an absolutely unexpected although very encouraging result taking into account the fact that no response from the defective area was detected in the CW experiments in the previous section.

The expected losses were calculated as a normalized overlap integral

$$EL^*(x) = \frac{\int_{-\infty}^{\infty} DZ^*(y) \cdot TA(y-x)dy}{\int_{-\infty}^{\infty} TA(y) \cdot TA(y)dy} \qquad (7.3.1)$$

of two functions, the first of which, complex $DZ^*(x)$, represents a different zones in the specimen, flawless and defective ones; the second function $TA(x)$ represents a sensitive zone of the TIRUS, the “TIRUS aperture” of 7 mm in size. Magnitude and argument of complex function $EL^*(x)$ represent an expected insertion loss and phase of the output TIRUS signal. The use of the overlap integral reflects the measurement procedure in which the TIRUS aperture moves across the specimen passing sequentially its flawless and defective parts, in which case the strength of the output signal at each position of the sensor depends on the overlap area. Figure 7.3.2 illustrates the calculation procedure – the green line in it is the calculated expected losses $EL(x)$=20Log($|EL^*(x)|$) expressed in dB.

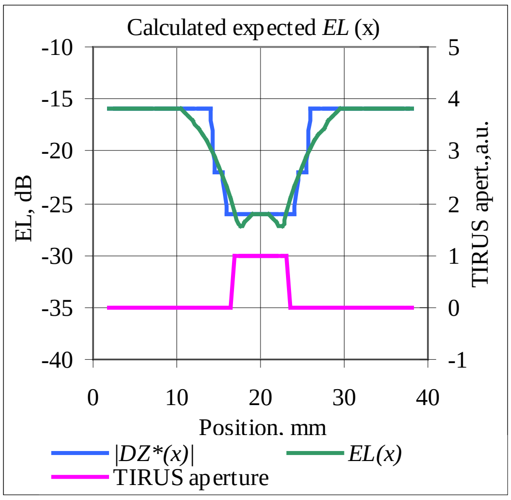

Fig. 7.3.2. Calculated *EL(x)* that could be expected on the base of experimental results

Data for computing function $|DZ^*(x)|$ representing the insertion losses were formed as follows: its bottom value equated to the average of all readings taken while the entire aperture of the TIRUS was on a flawless part of the specimen; on the contrary, its top value was taken as an average of the complete set of readings taken while the aperture was within the defective area. Data for the grooves between defected and flawless specimens (see a description of them in section 7.1) were taken in measurements with the TIRUS lifted up from the specimen surface and coated with the Sonotech Shear Gel that simulated grooves filled with the gel. Their influence on function $|DZ^{*}(x)|$ is expressed by steps on the blue line in Fig. 7.3.2.

The correlation coefficient between the expected and measured averaged functions $IL_{\mathrm{TG}}(x)$ is equal to 0.93. It is worth noting that this coefficient was also extremely high (0.89-0.93) for each individual measurement in the series. This certainly can be considered an encouraging result in assessment of applicability of the sliding technique.

In the experiments, measurements of the TIRUS time gated insertion losses $IL_{\mathrm{TG}}(x)$ and the output phase $\phi_{\mathrm{TG}}(x)$ were taken simultaneously. Averaged results of 6 individual measurements of *EPh(x)* taken when moving in the forward direction are presented in Fig. 7.3.3; the thin red ±2σ lines show the 95% confidence limits; the green line shows an expected phase of the TIRUS output signal. Figure 7.3.4 illustrates a procedure for calculation of the expected phase values identical to that described above for the expected insertion losses. The correlation coefficient between the calculated expected phase and the averaged experimental data is equal to 0.58 (0.48-0.63 in the series). It is less than in the case of the insertion loss measured that can be explained by a higher sensitivity of the time-gated phase to the thickness of the couplant layer, which varies when the TIRUS moves. Nevertheless, it demonstrates a probable high practical potential of the phase measurement channel.

Time gated experiments with glycerin used as a couplant were carried out in the same manner, however, no changes in the TIRUS time gated responses, both the insertion loss and the phase, were discovered. Apparently, it was a consequence of relatively small viscosity of this couplant.

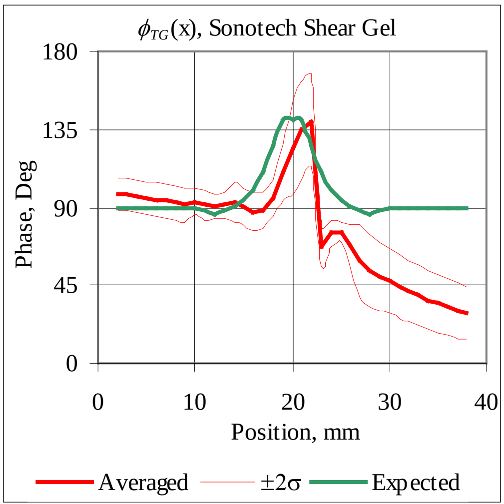

Fig. 7.3.3. The TIRUS averaged time-gated output phase ϕ_{TG} vs the sensor position *x*. The Sonotech Shear Gel used as a couplant; the forward motion (0 to 40 mm). The ±2σ lines show the 95% confidence limits.

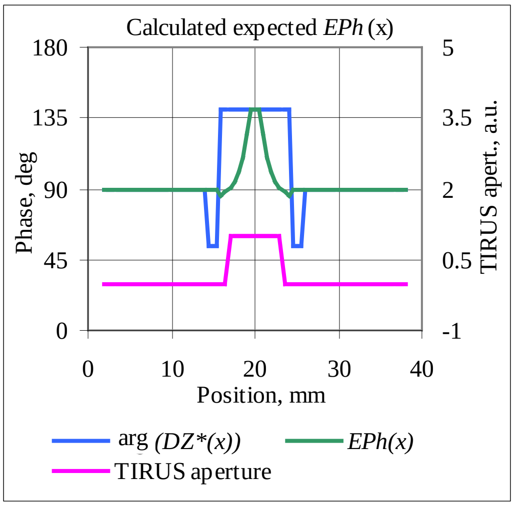

Fig. 7.3.4. Calculated *EPh(x)* that could be expected on the base of experimental results.

8 Optical Visualization of Ultrasonic Beams in Experimental Samples

8.1 Introduction

Well-known optical techniques, schlieren or photoelastic ones, are widely used for visualization of acoustic fields and propagation of ultrasonic pulses in liquids and solids for a long time [9-12]. In these techniques, the degree of disturbance of a light beam passing through a tested object caused by an ultrasonic wave is determined by a value of an effective photoelastic coefficient p_{eff} depending on properties of the material and on geometry of acousto-optic interaction [13].

In the TIRUS design (section 2.2), a probing slow shear wave (SSW) propagates along the [110] direction of the TeO_2 crystal and then is reflected from its sensitive inclined surface into the [001] direction. A sketch of the TIRUS body geometry is presented in Fig. 8.1.1. The side transducer emits an ultrasonic wave that after reflection travels up to the top transducer (reverse operation is also possible - see page 23 for the detail). The emitted wave is polarized along the [1$\bar{1}$0] direction, i.e. with respect to the inclined and to the top and bottom faces of the crystal it is a shear horizontal (SH) wave. It is done so to avoid conversion of the probing shear wave into other acoustic modes on reflection from the sensitive surface.

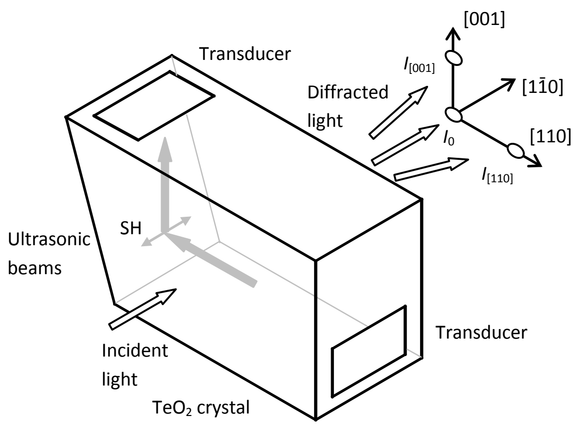

Fig. 8.1.1. Light diffraction patterns caused by acoustic waves propagating in different directions. A SSW emitted into the [110] direction is then reflected from the inclined face into the [001] direction. The direct beam spot I_0 denotes a light beam passing through the crystal; $I_{[001]}$ and $I_{[110]}$ denote light beams diffracted by the waves propagating in the directions [001] and [110] respectively.

Depending on the type of data to be obtained in optical experiments, an optical scheme of the optical setup should be essentially different. It is connected with two very different factors. One of them is a common feature of optical setups meant to visualize sound fields in investigated solids: different types of acoustic waves produce different types of light diffraction patterns to be recorded in the plane of observation. Therefore, an experimenter needs either to select a specific diffraction order from an entire diffraction pattern if the purpose is to study a specific acoustic mode or to collect all diffraction orders simultaneously to study mutual transformations of all acoustic modes observed. In which case, the observation conditions cannot be made equally beneficial for all studied modes and a compromise should be found depending on what a task is being solved.

Another factor is specific to experiments conducted in the current project. It is connected with the fact that shear waves polarized along the [1$\bar{1}$0] direction and propagating in the [110] and [001] directions of the TeO_2 crystal are undetectable when visualized with the light propagating along the [1$\bar{1}$0] direction, which can be defined as a “forbidden direction” [14]. The effective photoelastic constant that determines efficiency of the acousto-optic interaction depends on direction and polarization of acoustic and light waves and can be calculated [13, p.31] from the relation written in the index form

$$p_{eff} = p_{ijkl} d_i d_j m_k u_l \, . \tag{8.1.1}$$

Here d_i and d_j are components of the polarization vectors of the incident and diffracted light, u_l and m_k are components of the direction and polarization vectors of the ultrasonic wave, p_{ijkl} stands for components of the photoelastic tensor. As can be shown [3], for the chosen geometry of acousto-optic interaction (Fig. 8.1.1) and ultrasonic frequency of 27 MHz, only isotropic diffraction can take place, which means that incident and diffracted light beams have identical polarization. For the illuminating light polarized along the [001] direction, which is the case in the described experiments, "acting components" of the photoelastic tensor are p_{33kl}. Then, as can be derived from (8.1.1), for the shear waves propagating along the [110] and [001] directions respectively effective photoelastic constants in abbreviated notation are

$$p_{eff[110]} = p_{31} - p_{32} = 0 \qquad \text{and} \qquad p_{eff[001]} = p_{35} - p_{34} = 0 \tag{8.1.2}$$

because $p_{31} = p_{32}$ and $p_{34} = p_{35} = 0$. As seen from (8.1.2), for the geometry of acousto-optic interaction illustrated in Fig. 8.1.1 $p_{eff} = 0$ for both waves of interest. However, in the study of the TIRUS (and loss samples as well) just such geometry is necessary in the experiment because it enables the both incident and reflected ultrasonic beams to be visualized simultaneously, which is not possible when probing light comes from any other direction. As a result, one needs to deal with very weak, theoretically zero, diffraction patterns caused by the waves of interest. It has been shown, however, that light beams diffracted by the incident and reflected acoustic waves, although very weak, are observable in this case too [3]. In the recent researches [15, 16], not only the light diffraction patterns caused by these waves were observed but also the structure of ultrasonic beams and pulses was visualized.

In this section, the results are reported on real time optical visualization of an ultrasonic SH wave reflecting from an inclined boundary of the TeO_2 crystal, which is the TIRUS body. Additionally, images of "satellite pulses" caused by imperfection of the sensor design as well as images of spurious longitudinal waves emitted by a shear wave transducer are presented. Besides the results for the TIRUS, those for the "loss sample design" are also presented. Apart from these listed ones, two "side results" obtained in optical visualization experiments are discussed separately because they demonstrate *two effects that have apparently never been observed before*, a displacement of an ultrasonic beam on its reflection from a free flat surface [17] and conversion of an incident SH-wave into a longitudinal one [16]. All reported results are obtained in experiments with experimental "Loss" (Uj1, Uj2) and "TIRUS" (Uj3, Uj4) samples described in section 2.3.

8.2 Optical Setup

All images of visualized ultrasonic beams/pulses were obtained using a technique that can be called an acousto-optic one [18]. Unlike conventional techniques [9-12] in which all light diffracted by acoustic waves is collected by the lens of a recording camera, in the reported experiments individual diffraction orders were spatially filtered from the entire diffraction pattern to record images of different acoustic modes in the crystal. As a result, acoustic modes producing very weak light responses could be registered. After post-processing and alignment of the images recorded at the corresponding time points, they could also be superimposed to get a whole picture of acoustic modes present in the crystal.

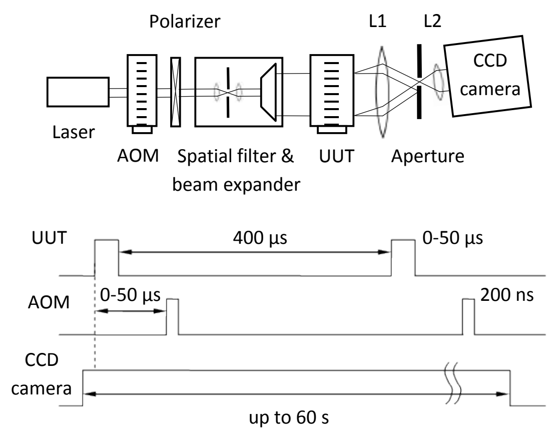

Fig. 8.2.1. Optical setup for visualization of ultrasonic pulses in the TIRUS and its time diagram. UUT stands for the "Unit Under Test".

A sketch of an optical setup is shown in Fig. 8.2.1. An output beam of a green laser is modulated with an acousto-optic modulator (AOM) and then passes through the optical forming system consisting of a spatial filter with a 15 µm pin-hole and a beam expander. From its output a well collimated light beam of 37 mm in diameter strikes an input surface of the unit under test (UUT) at the angle of incidence close to zero, passes it being diffracted by ultrasonic waves (Fig. 8.1.1) and then is collected by lens L1 located next to the UUT. A polarizer next to the AOM is necessary because the light passing through it becomes elliptically polarized.

Diffracted and passed light beams are not spatially separated immediately behind the UUT but lens L1 forms in its focal plane a diffraction pattern with separated diffraction orders $I_{[110]}$ from an incident ultrasonic wave and $I_{[001]}$ from a reflected one (see Fig. 8.1.1). The zero order I_0 is formed from the passing light beam. A particular diffraction order carries information on the structure of a corresponding ultrasonic beam. It is filtered by an aperture located in the focal plane of lens L1, which selects a diffraction order of interest. In visualization experiments, the focal distance of the lens was 500 mm and the aperture size was chosen from tenths of millimeter to a few millimeters depending on the level of the background noise. It is worth noticing here that the aperture size not only reduces the background noise but also determines an angular spectrum range of plane waves passing through the aperture, i.e., determines a sharpness of the image recorded by the CCD-camera.

The optical part of the setup is assembled on an optical bench. A diode-pumped solid state laser Monopower-532-100-SM ® produced by the Alphalas Gmbh is used as a light source. It provides up to 100 mW of continuous wave (CW) power at a wavelength of 532 nm producing an output beam of a good quality (M^2=1.1) with an excellent, less than 10 µrad/ºC, angle stability. With very weak light diffraction patterns to be recorded, it is important because the use of spatial filters requires a stable angle position of the laser beam dur-

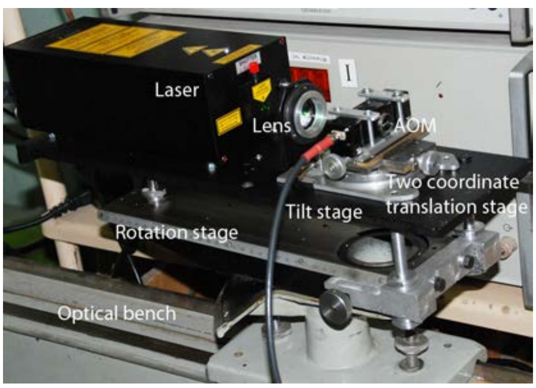

Fig. 8.2.2. A laser-AOM platform of the optical setup. After adjustment of the Lens-AOM assembly, the entire platform can be tilted and rotated to align the output light beam with an optical axis of the setup.

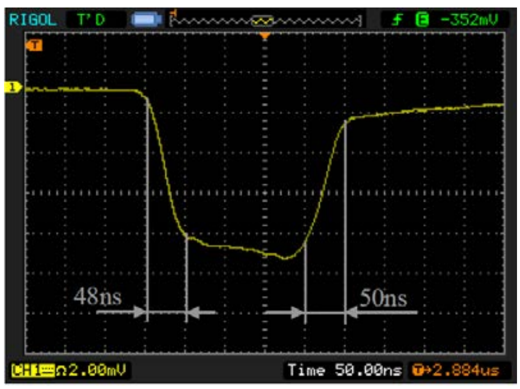

Fig. 8.2.3. A light pulse obtained with the AOM.

ing long lasting experiments that can take a few hours for a single series of measurements. The laser and the AOM are assembled on the common base forming a laser-AOM platform. An appearance of the constructed block is presented in Fig. 8.2.2. Its design includes two stages providing rotation and tilt of the entire block for alignment of the output laser beam with an optical axis of the optical bench. A lens at the laser output narrowing its beam enables the light pulses from the AOM to be as short as 200 ns (Fig. 8.2.3). That makes images of ultrasonic pulses as short as 1 μs recorded by the CCD camera be sharp enough. The two coordinate translation stage provides adjustment of the AOM relative to the lens and the laser beam.

The CCD camera lens L2 forms an image of an ultrasonic pulse on the CCD sensor. The Sony ICX285 sensor of the Baumer's TXG-14 industrial camera used as a recording device has resolution of 1392×1040 pixels and a very low intrinsic noise allowing exposure times from 4 μs to 60 s. That makes a choice of operational conditions very flexible and suitable for a wide variety of measured intensities of filtered diffraction orders.

8.2.1 Controller

The optical setup controller was designed as a single device interacting with a controlling PC through the interface developed on the platform LabVIEW®. The choice of this platform was determined by its flexibility and possibility of fast re-adjustment of the developed interface. In addition, it has an advanced library for processing and analysis of the acquired experimental data.

Specially developed electronics of the controller synchronize the TIRUS and AOM drivers as well as a CCD camera exposure to take images at predefined time intervals relative to a driving pulse for the Unit Under Test (UUT), which can be the TIRUS or the Loss sample. These time intervals and the delay times of the AOM driver and the camera trigger can be adjusted with the accuracy of 10 ns. Time diagrams of controlling signals are shown in Fig. 8.2.1. An interval between sequential timing signals is chosen to be 400 μs that is long enough

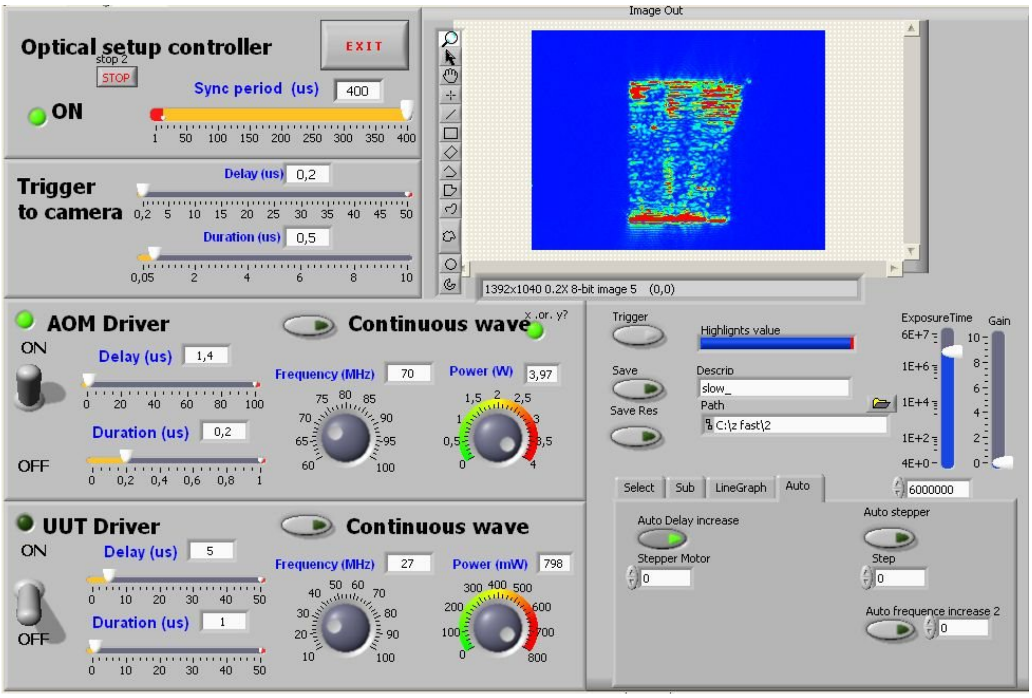

Fig. 8.2.4. Operational interface of the optical setup controller.

to provide a quasi-single sequence operation and avoid an overlap between ultrasonic pulses sequentially emitted by a transducer and pulses reflected from the crystal boundaries. In this case, duration of the emitted pulses can be chosen long enough, up to the entire propagation time of an ultrasonic wave along the crystal, if one needs to study a structure of an ultrasonic beam occupying its entire length. In the case of short emitted pulses, one can trace propagation, reflection and change in spatial structure of the pulses. Controlling the delay time between the pulse driving the UUT and an illuminating AOM pulse, one can also obtain a sequence of images for making a video of an ultrasonic pulse propagation and reflection. It also makes possible a time division of obtained images for different acoustic modes.

To match in time the set of generated pulse trains the high level host computer software written in the LabVIEW environment has been designed. The appearance of its interface is shown in Fig. 8.2.4. It is divided into separate functional blocks. On the left, three blocks meant to form matched pulse trains to control the camera, AOM and UUT are located. They are marked as “Trigger to camera”, “AOM driver” and “UUT driver”. A specific block responsible for interaction between the camera and the controlling PC is put on the right. The window within this block allows an operator to observe recorded images. Both RF channels, namely the AOM and UUT drivers, can be turned off or switched into a continuous wave mode.

The carrier of the RF driving pulses for the AOM and the UUT can be adjusted in the frequency ranges of 60-100 MHz and 10-100 MHz respectively. However, in the majority of experiments it was chosen to be 70 MHz for the AOM and in the vicinity of 27 MHz for the UUT, usually 27 MHz exactly.

The CCD camera is connected to the PC via the GigE interface using the LabVIEW module Vision Assistant. The images acquired are displayed in the window within the functional block in the right part of the interface window. Controlled parameters of the camera are the exposure time (4 µs – 60 s) and the amplification (gain) factor (0-10 dB). It can also be switched to run in the autonomous mode or to operate under control of the trigger from the optical setup controller. The images acquired can be saved as separate bitmap files or as a series of subsequent frames of the recorded video.

8.3 Experimental Technique

In the experiments, duration of light pulses from the AOM was 200 ns that determined temporal uncertainties in illumination of studied acoustic fields leading to spatial uncertainties in positions of their “frozen” images of the order of 5.5 wavelengths of acoustic waves [10]. With the shear wave (SW) velocities along the [001] and [110] directions equal to 2100 m/s and 612 m/s respectively and their frequency of 27 MHz, it derived corresponding spatial uncertainties ~430 µm and ~125 µm.

Because of very weak light responses from the studied ultrasonic waves, exposure times of the CCD camera were chosen rather long, up to 40 s for one frame [16, 17]. During this time a vast number of light pulses, up to 100,000, were accumulated by the camera sensor that enabled satisfactory images of ultrasonic pulses to be recorded. Nevertheless, real time processing of recorded images was as a rule necessary to separate a recorded pulse from an additive background noise caused by an internal scattering of light from the crystal. It consisted in recording of two sequential images, one with the emitting transducer switched off and another with an operating one, and subtraction of the former from the latter. In some cases, a further post-processing of the resulting image could be necessary to get an image suitable for an analysis.

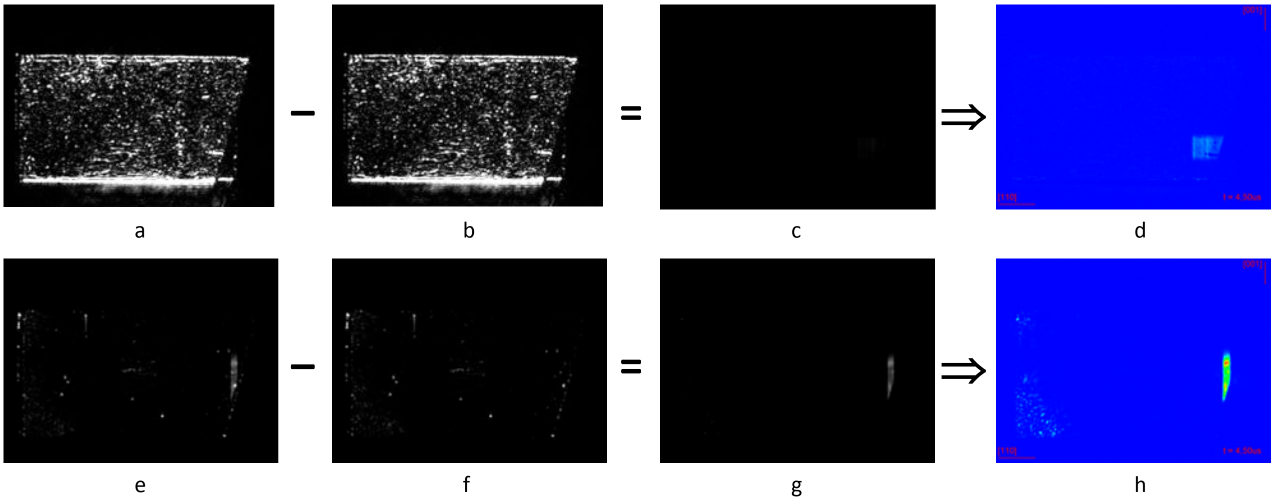

Fig. 8.3.1. A post-processing procedure applied to originally recorded images to extract an image of interest from the noise.

The whole procedure is illustrated in Fig. 8.3.1. It demonstrates obtaining images of a 1 μs pulse emitted by the top transducer into the [001] direction and then reflected into the [110] direction by the inclined face of the crystal. The top images are obtained from the $I_{[001]}$ diffraction order and the bottom ones –from the $I_{[110]}$ (see Fig. 8.1.1). Accordingly, the top row depicts the pulse incident at the inclined face and the bottom one shows the pulse reflected from it. Series of images of incident and reflected pulses, which then were used to create a video, were recorded in two successive experiments immediately following each other. (A combined image made from the selected frames of such a video will be presented in Fig. 8.4.6).

Images (a) and (e) correspond to the case of the emitting transducer, and images (b) and (f) were obtained when it was switched off, i.e., they represent an additive background noise present in the recorded images. A much greater noise while recording the pulse propagating along the [001] direction is explained by an almost 3.5 times less angle of diffraction of the diffraction order filtered by the aperture (see Fig. 8.2.1), in which case much more light scattered from the crystal are let into it. As seen in picture (*c*), this makes it impossible to observe the recorded pulse in the image with the subtracted background noise without its further post-processing because its brightness is too small to be visible. Results of the post-processing performed by means of applying a color palette to the brightness scales for images (*c*) and (*g*) are shown in pictures (*d*) and (*h*). In picture (*d*) derived from the “empty” picture (*c*) not only the pulse itself is seen distinctively, but also its spatial structure can be observed. In addition, comparative quantitative analysis of intensities of optical responses from incident and reflected pulses can be done based on data containing in images (*d*) and (*h*).

Depending on the purpose of a specific visualization task, the whole procedure described can be reduced to a simplified one omitting some steps in the post-processing, such as colorizing the difference image. Instead of that, the image can be only “amplified” that simplifies and accelerates the post-processing procedure essentially. It is particularly beneficial when an illustrative video is supposed to be made. A result of such a simplified procedure applied to images presented in Fig. 8.3.1 (*a*) and (*e*) is shown in Fig. 8.3.2 (*b*) and (*d*) respectively. The difference image (*d*) is cleaned from noise and the recorded image is clearly seen with no further post-processing. In image (*b*), the range of the lowest brightness levels of the initially “empty” image from Fig. 8.3.1 (*c*) is widen by 8 times to make the visualized ultrasonic pulse visible.

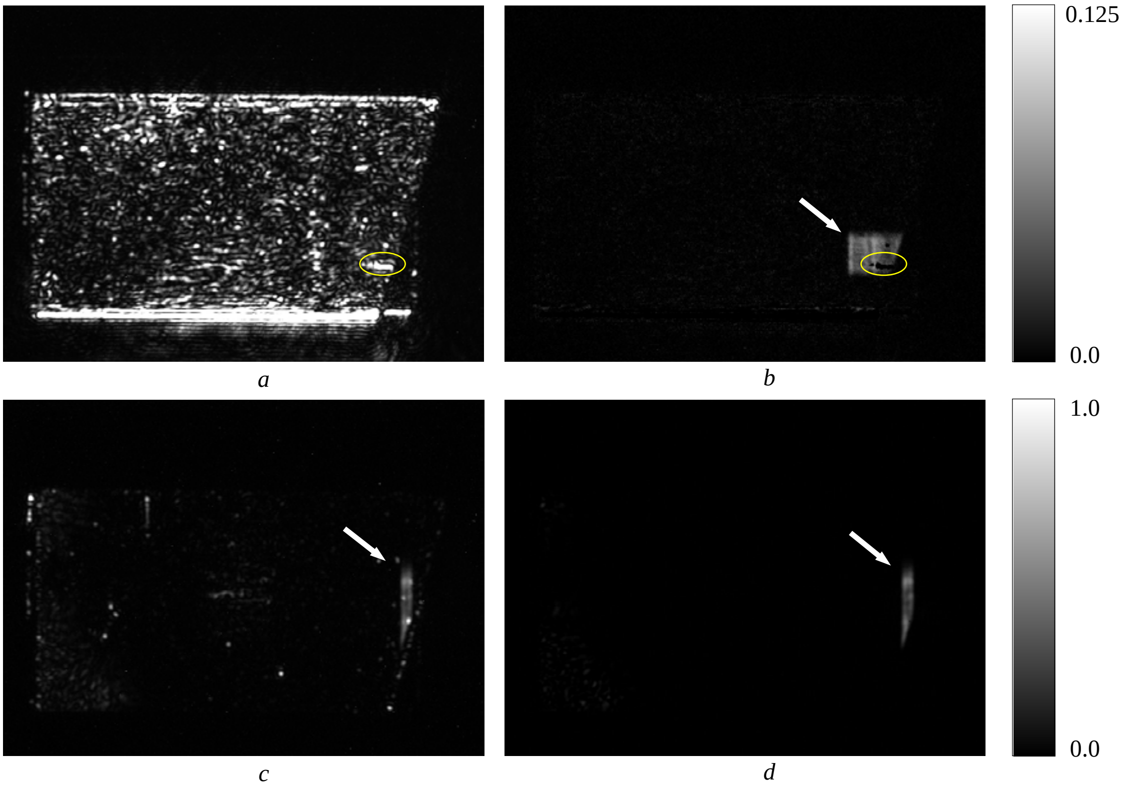

Fig. 8.3.2. A simplified post-processing procedure applied to recorded images. Images (*a*) and (*c*) are recorded by the camera; resultant images (*b* and *d*) are obtained after subtraction of background noise. The range of the lowest brightness levels in image (*b*) is widen by 8 times to make the recorded pulse visible. “Voids” in it outlined with a yellow oval are caused by the over-exposed regions in the recorded image (*a*). (Taken from [17]).

A special consideration should be given to overexposed regions of the originally recorded images caused by a background noise. After subtraction of the noise from original images, corresponding regions in the resultant ones become “empty” and looking as “voids”. An example of such voids marked with a yellow oval is presented in Fig. 8.3.2 (*b*). The overexposed regions that caused these voids are also marked with a yellow oval in the originally recorded image in Fig. 8.3.2 (*a*). It is obvious that a number and a size of the voids in the recorded image depend on the noise level and the exposure time of the camera. The longer exposure is, the more weak light responses from acoustic modes can be recorded; however, the noise also increases resulting in extension of the overexposed regions in the recorded image and in reduction of its contrast (dynamic range). In the resultant difference image, however, the contrast is retrieved or even increases because the noise is subtracted. At the same time, the voids, with no information in them, remain. Therefore, choice of exposure is always a trade-off between a necessary number of details of the lowest brightness levels in the resultant image to be obtained and an acceptable size of the void areas in it.

Thus, all the images of visualized ultrasonic fields presented below were obtained similarly. First, a unit under test (UUT) was mounted on the optical table in such a way that the input optical surface (L×H) of the TeO_2 crystal was oriented normally to the direction of the illuminating light beam with accuracy not worse than ±2 arcmin. A driving CW or RF pulse signal of 27 MHz was applied to one of the transducer of the UUT. Continuous illumination from the laser was switched on and a diffraction spot from an ultrasonic wave of interest in the focal plane of the lens behind the UUT was manually selected with the aperture to let it through to the camera. The light beam was switched to pulse illumination with the light pulse duration of 200-500 ns that provided the images recorded to be sharp enough. The exposure time and gain of the CCD camera were chosen in such a way to achieve a best, from the point of view of an experimenter, signal-to noise ratio. After that, a measurement cycle was launched organized as follows: (1) an image of an ultrasonic wave was captured with the camera; (2) the ultrasonic wave was switched off and a background image of the crystal without sound was captured – just such a situation operated by the optical setup controller is demonstrated in Fig. 8.2.4 in section 8.2.1; (3) it was then subtracted from the image recorded at the first step to get a difference image without a background noise. The cycle was operated by the optical controller automatically and was applied to each single individual measurement procedure.

8.4 Results and Discussion

8.4.1 Visualization of Ultrasonic Beams in the Loss Samples

Ultrasonic beams were visualized in two loss samples, Uj1 and Uj2, described in section 2.3, (Fig. 2.3.1). Each of them had mechanical damages on one of their faces. In the experiments, it did not deteriorate images obtained from the sample Uj1 significantly but certainly did so for the sample Uj2 screening a part of the sound field to be mapped into the optical image captured by the camera.

The two loss samples investigated in the experiments had different designs: in the Uj1, the transducers were located in the center of the crystal; in the Uj2, they were located in a position close to one of the crystal boundaries. As seen in Fig. 8.4.1 (*c*) on the next page, it results in “pure propagation” of an ultrasonic wave in the Uj1: it propagates not touching the boundaries. At the same time, in the Uj2 it touches, although very slightly, a top boundary of the crystal (picture (*e*)). However, it is difficult to conclude something more certain from this picture because of: (1) the ultrasonic beam seems to propagate a bit up from the emitting transducer. This effect could have been seen better if there had not been a screening effect from the damaged zone of the crystal (picture (*b*) in Fig. 8.4.1 and Fig. 2.3.1 (*b*) in section 2.3); (2) there is some imperfection in the crystal structure itself that seems to scatter ultrasonic waves. This imperfection is seen best of all in picture (*b*) where an image is presented of the crystal itself obtained from a non-diffracted light beam. It was also visible to the naked eye at thorough examination of the crystal.

Deflection of the ultrasonic beam also appears to take place in picture (*f*) but here the beam seems to propagate down. These deflection effects might have been a consequence of inaccurate orientation of the crystal with respect to the crystallographic direction [110] that causes deflection of the group velocity vector (the sound beam) from the wave vector. There was a high probability, however, it resulted from an improper adjustment of the optical setup that requires further investigation.

In experiments with Uj1, no particular effects were observed except the fact that in picture (*d*) there was no sound field observed immediately in front of the emitting transducer. For the time being, this fact is inexplicable but apparently, it is connected with geometry of the acousto-optic interaction used in the experiment, that is, with adjustment of the optical setup.

Because only qualitative results were of interest, some of the images in Fig. 8.4.1 were additionally processed with an image editor to better reveal a structure of the sound field examined. Therefore, quantitative comparison of these images would be incorrect. Anyway, observation of smooth fields in sample Uj1 and dis-

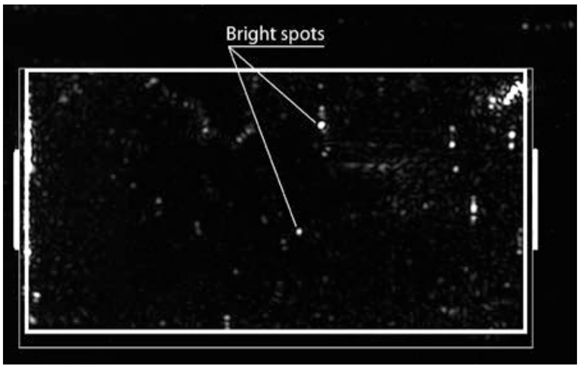

(*a*) Uj1, sound wave switched off

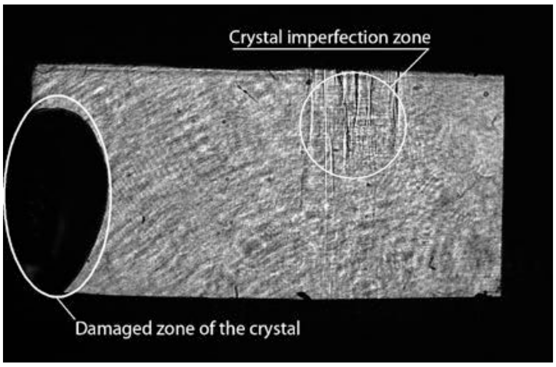

(*b*) – Uj2, crystal itself

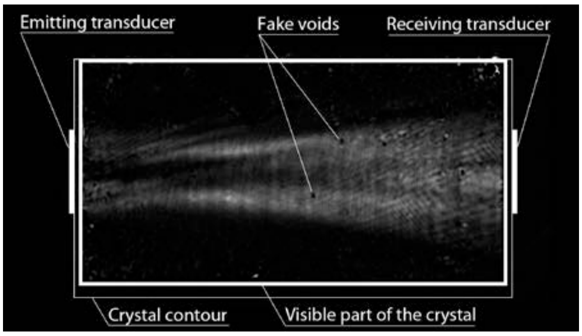

(*c*) Uj1 driven with the 35 μs RF pulse from the left. Exposure time 15 s, gain of the camera 10 dB.

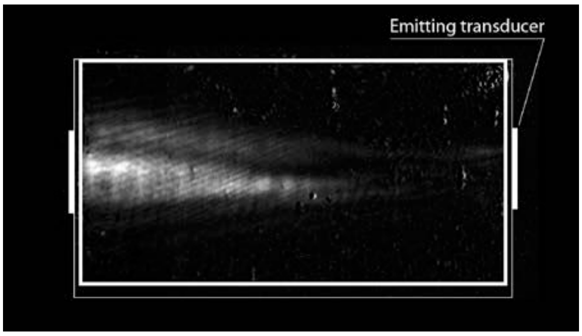

(*d*) Uj1 driven with the 35 μs RF pulse from the right. Exposure time 15 s, gain of the camera 10 dB.

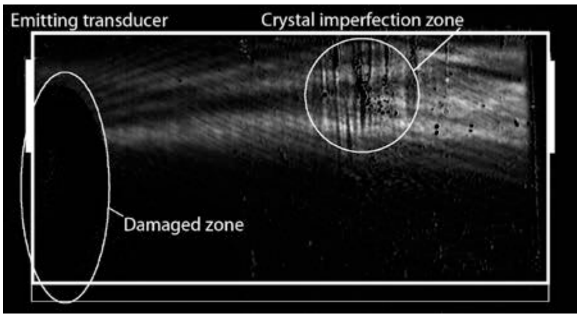

(*e*) Uj2 driven with the 36.5 μs RF pulse from the left. Exposure time 20 s, gain of the camera 0 dB.

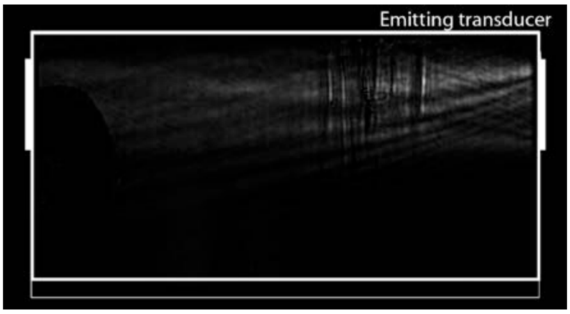

(*f*) Uj2 driven with the 36.5 μs RF pulse from the right. Exposure time 20 s, gain of the camera 0 dB.

Fig. 8.4.1. Results of visualization of sound fields in the loss samples. (*a*) – Uj1, background image; (*b*) – Uj2, image of the crystal itself, sound is switched off; (*c*), (*d*) – Uj1, sound field in the crystal; (*e*), (*f*) – Uj2, sound field in the crystal. The light pulse duration is 0.5 μs. The crystal sizes are 21.3×12 mm (Uj1) and 23×12 mm (Uj2).

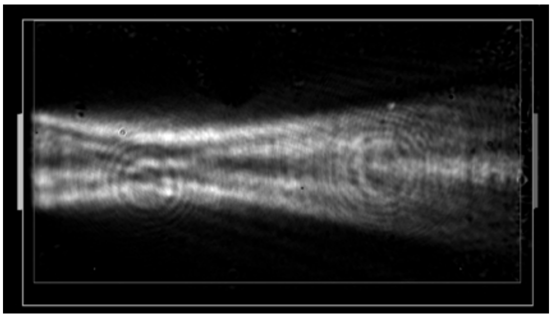

Fig. 8.4.2. A near-field structure of the SSW field observed from the forbidden [1$\bar{1}$0] direction. (Taken from [15]).

turbed ones in the Uj2 can seem to serve an explanation of greater insertion loss of Uj2 measured in sections 3.1 and 4.1.

Another certain conclusion that can be inferred from the results presented is that ultimate understanding of the ultrasonic wave behavior in the loss samples could have been achieved only with a greater number of samples examined. At the same time, as seen in Fig. 8.4.2 [15], the developed technique produce quite satisfactory results in mapping a sound beam observed from the forbidden direction: the near field structure of the radiated ultrasonic beam is distinguishable.

8.4.2 Visualization of Ultrasonic Beams and Pulses in the TIRUS

Unlike the experiments with the "Loss samples", those with the TIRUS samples could be conducted not only to visualize ultrasonic beams propagating along the [110] direction of the TeO_2 crystal but also to visualize waves propagating along the [001] direction. It is connected with two factors: (1) in the TIRUS design there are two different transducers that can emit ultrasonic waves into two orthogonal directions, [110] and [001]; (2) an ultrasonic beam excited by either of two transducers reflects from a tilted surface of the TIRUS and changes its propagation direction into a perpendicular one.

Results of visualization of shear slow waves (pure modes) radiated by the transducers into the [110] direction of two TIRUS samples Uj3 and Uj4 are presented in Fig. 8.4.3, (*a*) and (*b*) respectively. An active (emitting) transducer is depicted with a green line, a passive – with the red.

As seen from the figures, the observed ultrasonic beams are on the whole similar to each other in their structure but the details are different. For example, an area just in front of the emitting transducer in the sample Uj3 is dark whereas in the sample Uj4 it is bright. In addition, diffraction divergence observed in the right part of the image is more explicit and the beam waist is also shaped more explicitly in Fig. 8.4.3 (*b*) than in (*a*). Despite all these distinctive qualitative differences, ultimate conclusions about a real field distribution can be done only after improvement of experimental technique and conducting a quantitative analysis of additional data obtained with it.

Although the reported data are not of a proper quality for a quantitative analysis of the sound field distribution, the developed technique itself is perfectly suitable for a study of propagation and reflection of ultrasonic pulses in the TIRUS body. Some unexpected results obtained in such a study of the TIRUS sample Uj3 are presented in Fig. 8.4.4.

The picture in Fig. 8.4.4 (*a*) was obtained at an intermediate stage in the TIRUS fabrication process when an inclined surface of the crystal had not been yet made. Examination of the entire light diffraction pattern caused by ultrasonic waves showed that a light response from a longitudinal wave emitted by the shear wave

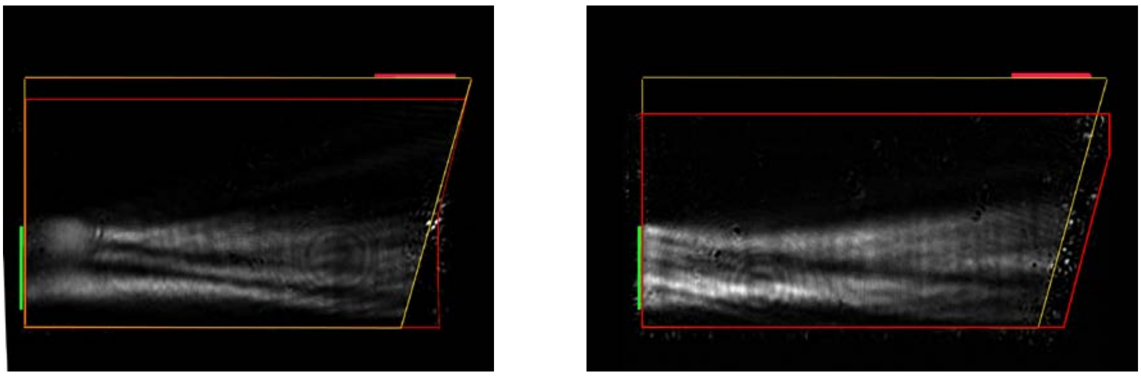

a *b*

Fig. 8.4.3. A SSW in the TIRUS propagating in the [110] direction. Ultrasonic pulse duration is 35 µs, exposure time 15 s; *a* – sample Uj3, no camera gain; *b* – sample Uj4, camera gain 10 dB. Yellow lines depict the crystal boundaries, red – a visible area in the experiments.

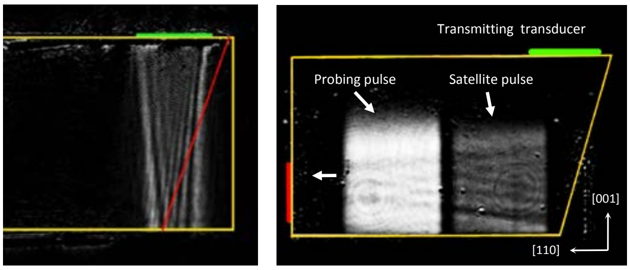

a *b*

Fig. 8.4.4. A longitudinal wave excited by a shear wave transducer (*a*) and a satellite pulse caused by re-excitation of the top transducer (*b*). The sample studied is Uj3. Duration of ultrasonic pulses is 3 µs (*a*) and 10 µs (*b*). Yellow lines depict boundaries of the crystal. Picture (*a*) is obtained at an intermediate stage of the sample fabrication process. The red line in it shows a position of an inclined surface of the crystal to be done at the next stage.

transducer into the [001] direction was much easier to observe than to detect a sought shear wave. In the experiment, the top transducer was excited by a 3 µs RF pulse with carrier frequency of 27 MHz and an optical response from the longitudinal wave was filtered with the aperture (see Fig. 8.2.1) to record an image of the emitted ultrasonic pulse. As seen from Fig. 8.4.4, the ultrasonic pulse field has a typical near-field structure and occupies the full height of the crystal because the flight time of the longitudinal wave across it is ~3 µs. The longitudinal wave is emitted because the transducer of 163° y-cut $LiNbO_3$ generates not a pure shear acoustic mode but a quasi-shear one with the angle between the displacement vector and the wave front ~2°. Although the intensity of this wave is much less than that of the shear wave, at least by 26 dB, it was easily observed due to a rather great value of its acousto-optic figure of merit $M_2=34.5\times10^{-15}$ s^3/kg [19]. Obviously, its presence can cause spurious signals in the TIRUS if a high dynamic range is of concern.

Another effect causing spurious signals observed in visualization experiments was an unexpected occurrence of a satellite ultrasonic pulse due to a mismatched size of the top transducer, which is demonstrated in Fig. 8.4.4 (b). A 10 µs probing RF pulse is emitted by the top (green) transducer into the [001] direction and after reflection from the inclined face travels in the [110] direction towards the red transducer on the left side of the crystal. One can see, however, that behind it there is a weak image of a second, satellite pulse of the same duration, travelling in the same direction (the image is post-processed to emphasize the satellite pulse). This satellite pulse is a result of reflection of a small part of energy of the initially emitted pulse that reaches the crystal bottom face parallel to the top face. Returning to the top face, it re-excites a part of the transducer, which re-emits one more pulse from its entire surface covered with electrodes. The re-emitted pulse repeats the path of the first pulse reflecting from the inclined face and emerging behind the first one delayed by 12 µs, which is just the time for passing the double height of the crystal. The visualized effect manifested itself in the time gated experiments as a spurious second pulse train (see Fig. 4.2.1 in section 4.2) at the TIRUS output.

8.4.3 Conversion of a SH-wave into a Longitudinal One on Normal Reflection From a Free Flat Surface

Theoretically, there should be no conversion of a shear horizontal (SH) plane bulk elastic wave into other acoustical modes on its reflection from a flat interface in an isotropic medium [20]. The same holds true for an anisotropic medium if the incident SH-wave is a pure mode because in this case its displacement vector lies in the reflecting surface and its projections on the displacement vectors of two other eigen waves of the medium are equal to zero. In this section, **we report experimental results on visualization of the SH-wave conversion into a longitudinal one on its normal reflection from a (001) free face of the TeO_2 crystal, which is just a mentioned type of reflection** [16].

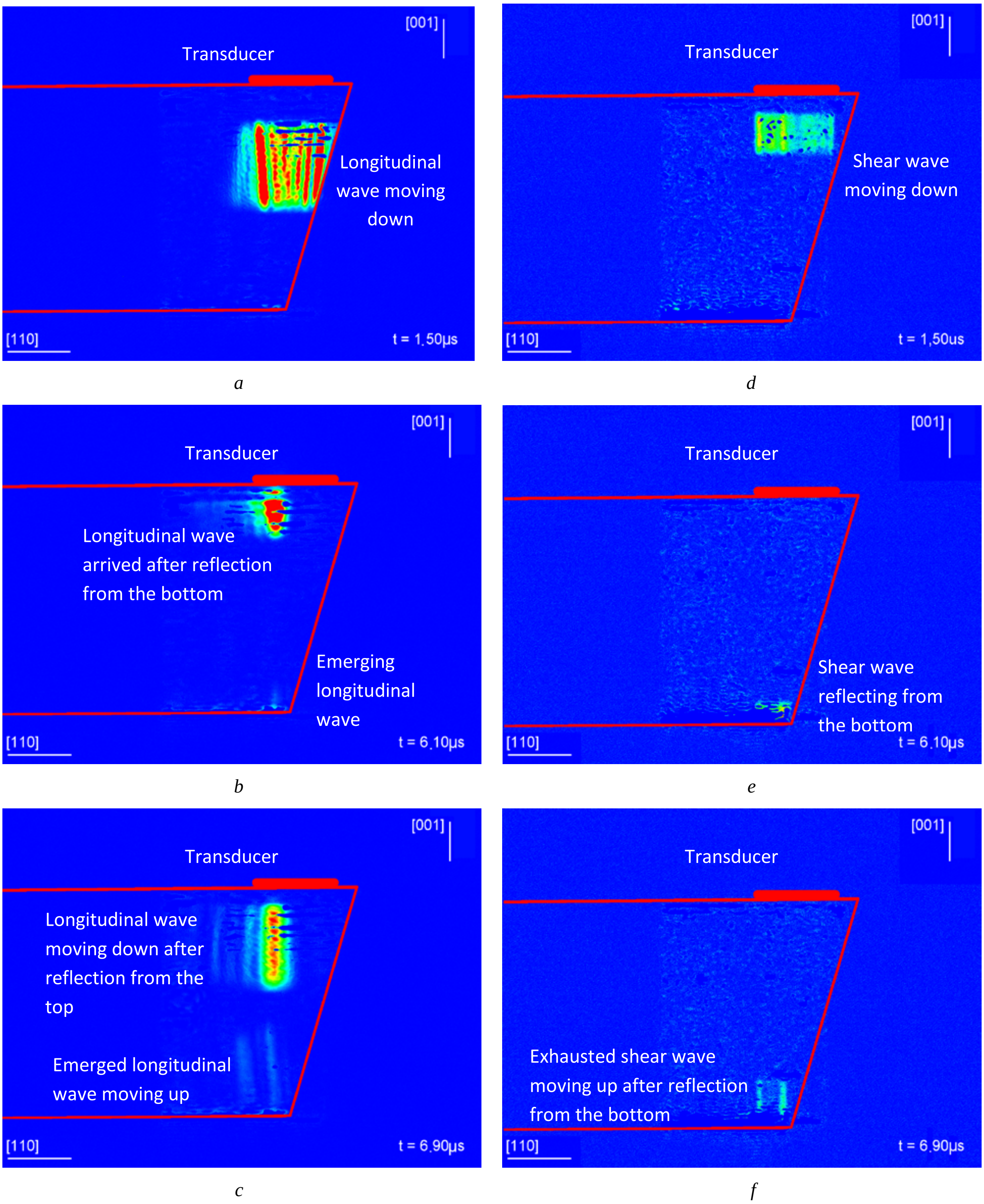

Fig. 8.4.5. Conversion of the SH wave into a longitudinal one on its normal reflection from the face (001) of the TeO_2 crystal. *a*, *b*, *c* – propagation, reflection and emergence of the longitudinal waves; *d*, *e*, *f* – propagation and reflection of the shear wave. Duration of the radiated pulses is 1 μs, the carrier frequency is 27 MHz.

The reflection process is shown in Fig. 8.4.5 where the ultrasonic pulses recorded in successive moments of time are presented. The left column of pictures represents a longitudinal wave, the right column – a shear wave, which is of a SH-wave type because it is polarized normal to the plane of the picture. Both studied waves (pulses) are emitted into the [001] direction by the shear wave transducer located on the top face of the crystal, the situation considered in the previous section. Duration of the radiated pulses is 1 μs, the carrier frequency is 27 MHz.

Time markers in the right low corners of the images display moments of time when the images are taken with the camera. They are counted from the moment of the top transducer excitation by a probing RF pulse taken as a zero point on the time scale. The first pair of images taken at 1.5 μs (*a* and *d*) are selected simply to portray both the longitudinal and the SH waves radiated. As is seen from the pictures, the spatial length of the longitudinal pulse is twice as large as that of the shear one because the longitudinal wave is approximately twice faster than the shear one. There is nothing unusual in these images.

On the contrary, **images *b* and *e* taken at 6.1 μs depict an unexpected phenomenon**: a longitudinal wave emerges (image *b*) from that place on the bottom face of the crystal where the shear wave, initially radiated from the top transducer, strikes it (image *e*). By this moment (6.1 μs), the initially radiated longitudinal wave pulse has already reflected off the bottom and has reached the top face reflecting from it, that is, it cannot be a source for the longitudinal wave emerging at the bottom face. The last pair of images (*c* and *f*) displays the development of the process: both the emerged longitudinal and the reflected from the bottom shear waves move toward the top face of the crystal whereas the originally radiated longitudinal wave reflected from it moves to the bottom repeating a cycle.

The only reasonable conclusion that can be drawn from what is presented in images *b*, *e*, *c* and *f* of Fig. 8.4.5 is that **the observed phenomenon is partial conversion of the incident SH wave into a longitudinal one on its reflection from the bottom face of the crystal. This is theoretically inexplicable** because the displacement vector of the incident SH wave lies in the reflecting plane, in which case no longitudinal wave can emerge at the bottom. Thus, the results obtained have raised the question of what is the reason for the observed phenomenon. **A possible reason for the observed theoretically impossible for plane waves conversion of the pure SH-wave pulse into a longitudinal one on its normal reflection might be conversion of some plane-wave spectral components of the incident shear wave ultrasonic beam slightly deflecting from the [001] direction.** The displacement vectors of these waves might lie out of the (001) plane and consequently can have [001] components to generate a longitudinal wave. Anyway, the described finding requires further research including both an experimental confirmation of the observed conversion and a theoretical analysis of spatial properties of the incident ultrasonic beam including calculation of its angular spectrum.

8.4.4 Displacement of an Ultrasonic Beam on Oblique Reflection from a Free Flat Surface

The material in this section is presented closely following [17]. **A phenomenon reported has, to the best of our knowledge, never been observed or theoretically predicted before. It is a displacement of an ultrasonic beam (pulse) on its reflection from an oblique *free* flat surface.** The displacement of an ultrasonic beam on its reflection from a flat surface is a well-known phenomenon that has been repeatedly observed by many researchers since the middle of the last century. These displacements, however, were observed exclusively when an incident beam reflected either from an interface between an examined medium and another liquid or solid, or a reflecting surface was disturbed by a periodic spatial structure on it [21]. In which cases some types of surface waves could be excited by an incident ultrasonic beam that caused a displacement of the reflected beam. No such waves can be excited by a SH bulk wave incident on the free flat surface.

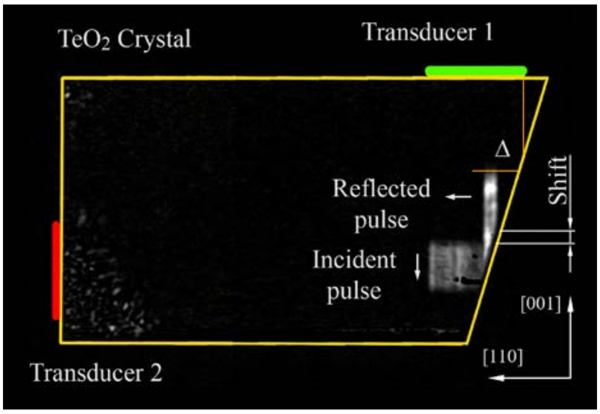

Fig. 8.4.6. Displacement of a reflected ultrasonic beam. The intersection point of the reflected pulse rear and the reflecting plane is shifted up with respect to that of the incident pulse. A real displacement of the beam is determined by a gap Δ between virtual boundaries of the incident and reflected beams indicated with orange lines.

The discussed phenomenon was discovered in the analysis of processed data when corresponding images of incident and reflected 1 μs pulses were superimposed to get combined images consisting of both incident and reflected pulses put together into one image. One of such images combined from images of Fig. 8.3.2, (*b*) and (*d*), is shown in Fig. 8.4.6. A significant difference between pulses lengths is connected with the difference between their velocities. As seen from the figure, **the reflected pulse is shifted up with respect to the incident one approximately by a third of the size of the latter. As to the beam displacement, it can be inferred from the observed gap Δ between the virtual boundaries of the incident and reflected beams indicated with the orange lines.** The demonstrated picture is one from a sequence of images recorded one after another with a 0.1 μs interval. Other pictures from the sequence display similar shifts. **Thus, one can conclude that the phenomenon observed takes place at least for the considered geometry of the TeO_2 crystal.**

For the time being, there is no satisfactory explanation of the observed phenomenon. It follows from the theory of the beam displacement [22] that it can be treated as a phase shift between incident and reflected beams on a virtual plane in the vicinity of the reflecting boundary. Since in the experiment the observed beams are shifted from the reflecting boundary because of a screening effect of a 0.2 mm chamfer, a similar phase shift can result in the observed displacement. There may be, however, another reason that should be analyzed. Because TeO_2 is a piezoelectric material, although a weak one, a possible excitation of Bleustein–Gulyaev waves might occur [23], which changes boundary conditions and leads to the displacement of the beam.

8.5 Conclusions

An acousto-optic technique incorporating a principle of accumulation of a vast number of light pulses diffracted by an acoustic wave has proved to be suitable for imaging of shear wave acoustic fields observed in the TeO_2 crystal from the “forbidden” $[1\bar{1}0]$ direction. Its application made it possible to trace propagation and reflection of ultrasonic pulses in real time and to get images of ultrasonic beams structures. As a result, an “effect of a satellite pulse” caused by imperfection of the sensor design that led to appearance of spurious signals at the TIRUS output reported in section 4.2 was observed and explained. A spurious longitudinal wave generated by a shear wave transducer was discovered that can be an explanation of appearance of longitudinal waves in the sensor body observed in the previous research [1].

Some minor effects, inexplicable for the time being, such as deflection of an ultrasonic beam from the normal to the emitting transducer or a dark zone in front of it observed in particular experimental samples require additional investigations with a more number of experimental samples to be explained.

Two effects that have apparently never been observed before were discovered, a displacement of an ultrasonic beam on its reflection from a free flat surface and conversion of an incident SH-wave into a longitudinal one. These findings are the most important results obtained in optical visualization experiments therefore the observed phenomena require further research into their nature including both an experimental study of them and a theoretical analysis of spatial properties of incident ultrasonic beams including calculation of their angular spectra to be verified and confirmed.

9 Modeling of ultrasonic beams and calculation of diffraction losses in the TIRUS

List of Symbols

Latin alphabet

a	radius of a circular transducer
a	complex amplitude of a plane wave
a_α	complex amplitude of the wave mode α
$\mathbf{A}$ and A_i	the normalized polarization vector and its components
$\mathbf{A}_\alpha$ and A_x^α, A_y^α, A_z^α	the normalized polarization vector of mode α and its components
b_α	complex amplitude of a reflected wave of mode α
$\mathbf{c}$ and c_{ijkl}	the stiffness tensor and its components
$\mathbf{k}$ and k	the wave vector and its length
$\mathbf{k}_\alpha$	the wave vector of mode α
$k_{\parallel}$	length of in-plane projection of the wave vector
k_x, k_y	components of in-plane projection of the wave vector
k_z^α	z-projection of the wave vector of mode α
$\mathbf{L}_\alpha$	a specific vector of the Stroh formalism
$\mathbf{L}_\alpha^i$ and $L_{\alpha x}^i$, $L_{\alpha y}^i$, $L_{\alpha z}^i$	vector $\mathbf{L}_\alpha$ for the incident wave of mode α and its components
$\mathbf{L}_\alpha^r$ and $L_{\alpha x}^r$, $L_{\alpha y}^r$, $L_{\alpha z}^r$	vector $\mathbf{L}_\alpha$ for the reflected wave of mode α and its components
$\mathbf{m}$	unit vector corresponding to the direction of in-plane projection of the wave vector
$\mathbf{n}$ and n_j	unit vector corresponding to normal to a boundary plane and its components
$\hat{N}$	a matrix of the Stroh eigenproblem
p_α	eigenvalue of the Stroh problem
$\mathbf{P}_\alpha$	the Pointing vector for mode α
$\mathbf{q}$	unit vector of the wave normal
$\mathbf{r}$	radius vector
S	a normalized distance from the source to the receiver
$\mathbf{T}_0$ and T_x^0, T_y^0, T_z^0	an angular plane wave spectrum (Fourier transform) of the traction force at a boundary plane
t	time
$\boldsymbol{u}$ and u_i	the displacement vector and its components
$\mathbf{U}$	an angular plane wave spectrum (Fourier transform) of the displacement field
$\mathbf{U}_0$ and U_x^0, U_y^0, U_z^0	an angular plane wave spectrum of the displacement field at a boundary plane
v	velocity of the sound wave
x_i	coordinates of the radius vector
x, y, z	Cartesian coordinates associated with the calculation planes where z is a beam propagation direction

Greek alphabet

α	index of the plane wave mode in the crystal
λ	wavelength of sound
ξ_α	eigenvector of the Stroh problem
ρ	density of the material
$\boldsymbol{\sigma}$ and σ_{ij}	stress tensor and its components
$\boldsymbol{\Sigma}$ and Σ_{ij}	an angular plane wave spectrum (Fourier transform) of the stress tensor and its components
$\boldsymbol{\tau}$ and τ_i	the traction force at a boundary plane and its components
$\boldsymbol{\tau}_\alpha$ and τ_x^α, τ_y^α, τ_z^α	the traction force at a boundary plane for mode α and its components
ω	cyclic frequency

Introduction

Spatial properties of an ultrasonic beam in the TIRUS determine its behavior as a sensor. Unexpectedly large insertion losses obtained in electrical experiments posed a problem of modeling ultrasound beam propagation in the TIRUS. This can provide needed information to analyze possible reasons of such behavior. Modeling of the beam propagation was expected to answer two questions concerning operation of the TIRUS. Firstly, whether some unusual mode conversion is possible on a reflecting plane which is the sensitive surface of the TIRUS. Secondly, what diffraction losses the sound beam experiences during its propagation from an emitting transducer towards a reflecting plane and after its reflection towards a receiving transducer. Thus, the modeling includes two procedures, one for calculation of diffraction effects in a freely propagating ultrasonic beam, and another, for calculation of the beam field after reflection from the boundary plane.

9.1 Modeling of an Ultrasonic Beam Propagation

9.1.1 Choice of a Model

The approach to analysis of known ultrasonic beam models applicable to the TIRUS case should start from consideration of the TIRUS design itself. Taking into account specific properties of the considered design, one can filter those models that better represent physical mechanisms underlying principle of operation of the TIRUS.

As seen from Fig. 9.1.1, the TIRUS design includes as main constructive elements, besides the TeO_2 crystal itself, a free reflecting surface and two piezoelectric transducers. The latter are shear wave transducers made of the *y*+163º cut of $LiNbO_3$. They generate a quasi-shear (QS) wave with the angle between its polarization and wave vectors equal to 91.7º [24]. That is, the difference of the QS-polarization from that of a pure transverse mode is only 1.7°, which for the purpose of the current research can be neglected. The transducers operate at the frequency

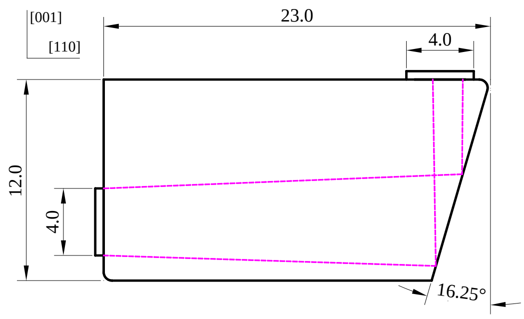

Fig. 9.1.1. The TIRUS design. Transducers on the left and top sides of the crystal are of 4×6.5 mm size. They are made out of the $LiNbO_3$ plates and transmit or receive a shear wave polarized perpendicular to the plane of the picture. This picture is the same as Fig. 2.2.1 appeared in a section describing the TIRUS concept.

27 MHz, their size is 4×6.5 mm with the shorter size along the [001] direction. They are bonded to the crystal with overall thickness of bonding layers as small as 1 μm so their influence can also be neglected. Thus, a natural assumption of the transducer as a uniform force applied in the free (110) plane of the TeO_2 crystal across the radiating area seems reasonable for the problem of modeling the beam radiated.

Because of interest in their applications to the NDE purposes, a wide variety of techniques for modeling ultrasonic beams in anisotropic solids have been developed in recent three decades. Early developments are reviewed in [25, 26], more recent in [27, 28]. The vast majority of them analyze a typical "immersed" NDE situation when an ultrasonic wave is excited in solid by an external ultrasonic beam incident at its surface from a fluid medium. Although this is not the considered case of a SH wave excitation from a surface of the crystal and not each of the developed approaches can be applied to the TIRUS directly, most of them are of use while analyzing the issue of which of the modeling techniques can be most beneficial for the case considered.

The developed techniques can be divided into a few categories: (1) those exploiting Green's functions representing point sources; (2) the angular plane wave decomposition of the wave field; (3) a point source synthesis approach; (4) multiple Gaussian beams superposition; (5) finite element modeling (FEM). They naturally differ in their computational power and also in the assumptions put into the underlying procedures and the spheres of their applications.

The FEM technique is the most calculation intensive. With the wavelength of the ultrasonic wave radiated by the transducer being 23 μm and the sensor body of 23×12×10 mm in size, assuming 6 elements per wavelength [29], the number of nodes necessary to build a 3D mesh over the whole crystal should have been $1000\times522\times435\times6^3=1.7\cdot10^{11}$. This is well known practical restrictions of the finite element method, therefore with it usually 2-D problems are analyzed when ultrasonic beams in fluid medium are modeled [30]. The TIRUS case cannot be reduced to such an approach because divergence of the sound beam in differently oriented cross-sections differs considerably. Calculation of a full 3D mesh is computationally very expensive, and for this reason, it is impossible to use FEM in the frame of the current project.

The use of the Green's function approach [31] and angular plane wave decomposition method [32, 33] enables to model ultrasonic beams using moderate requirements to the computer power. These two methods are very similar with regard to numerical implementation and differ only in formulation of boundary conditions. In the Green's function method, the radiation caused by a force load is considered whereas in the plane wave decomposition method, diffraction effects in the sound wave propagation in the medium without any applied forces are studied. Both methods can be effectively implemented using the fast Fourier transform. However, they cannot be readily applied in the far field because of difficulties with integration of fast-oscillating integrands. This problem is usually avoided by applying the method of stationary phase [33]. Such an approach also somehow reduces computational requirements, but gives rise to another problem of finding positions of stationary points, which can be not a trivial task.

The method of point source synthesis [28] is an approximate method for calculation of sound fields. It uses point directivity patterns and is based on the far-field approximation, but might possibly give good results at intermediate distances too. Computational requirements are comparable with those of stationary phase methods. The method fails for directions in which there is a singularity on the slowness surface.

The method of Gaussian beam superposition [35] is the fastest one among those used for calculation of ultrasonic fields. It uses far-field approximation and does not take into account variations of the wave polarization inside each of Gaussian beams. Therefore, it is almost certainly not suitable for application to the TIRUS case because of change in the polarization within ultrasonic beams propagating in the sensor body, which in the TeO_2 crystal takes place and is especially noticeable in the [001] direction.

Considerations made in [26] and [28] show that Gaussian beam superposition fails in calculation of the field in the vicinity of the transducer. At the same time, techniques using the Green’s function approach or the plane wave decomposition operate better in the near field than in the far field. As the TIRUS design supposes that the near field zone of the emitting transducer is ~15-20 mm [1], it seems reasonable to use one of these two techniques to model the ultrasonic beam. In further sections an approach realizing a plane wave decomposition technique is developed and tested.

9.1.2 A Plane Wave Decomposition Method

The plane wave decomposition technique [33, 35] enables an ultrasonic *displacement* field to be calculated at any point of a half-space given the field distribution is known at its boundary. If an assumption is made that a transducer contacting the boundary determines displacements at it, this technique can be applied to the TIRUS case with the crystal treated as a half-space. It differs from the assumption about the transducer as a *force* uniformly distributed over its radiating surface, made in the previous section, but is a reasonable alternative to simplify the problem being solved. We consider a situation when the transducer size is much greater than the wavelength, which also supports this assumption.

Acoustic wave propagating in an anisotropic medium satisfies the wave equation [5]

$$c_{ijkl}\frac{\partial^2 u_l}{\partial x_j \partial x_k} = \rho\frac{\partial^2 u_i}{\partial t^2}, \tag{9.1.1}$$

where c_{ijkl} is the stiffness tensor and ρ is the medium density. Its plane-wave solution for the displacement field

$$\mathbf{u}(\mathbf{r},t) = a\,\mathbf{A}\exp[i(\mathbf{k}\cdot\mathbf{r} - \omega t)], \tag{9.1.2}$$

where a is a scalar amplitude, $\mathbf{A}$ is a normalized polarization vector, which coincides with the direction of a displacement vector $\mathbf{u}$; $\mathbf{r}$ is the radius vector, $\mathbf{k} = (\omega / v)\mathbf{q}$ is the wave-vector, ω is a cyclic frequency, v is a phase velocity of the wave, t is time and $\mathbf{q}$ is a unit vector of the wave normal. Substitution of a plane wave solution into the wave equation yields a Christoffel equation

$$c_{ijkl}q_j q_k A_l = \rho v^2 A_i\,. \tag{9.1.3}$$

Solving the eigenvalue problem for this equation produces polarization vectors $\mathbf{A}_\beta$ and associated phase velocities v_β. In an anisotropic medium there always exist three solutions (denoted with subscript β) corresponding to three waves, generally one quasi-longitudinal and two quasi-shear ones, propagating in a chosen direction of the wave normal $\mathbf{q}$.

Equation (9.1.1) is a linear homogeneous differential equation, so any linear combination of its solutions also satisfies it and can be combined into a single generalized solution

$$\mathbf{u}(x,y,z,t)=\int_{-\infty}^{\infty}d\omega\int_{-\infty}^{\infty}\int_{-\infty}^{\infty}dk_x dk_y\sum_{\alpha=1}^{3}a_\alpha\mathbf{A}_\alpha\exp[i(\mathbf{k}_\alpha\cdot\mathbf{r}-\omega t)]\,. \tag{9.1.4}$$

(Here and in the following text Greek indexes are used as free indexes and don't mean summation if repeated, so we use explicit summation sign for α.) Such a representation of the wave field is the main idea of the plane wave decomposition method: any given solution can be described as a sum of the plane wave solutions. Integration is performed only over two components of the wave vector k_x, k_y. The third component k_z^α cannot be arbitrary as it depends on the two other components. It is allowed only three values $k_z^\alpha(k_x,k_y)$, $\alpha=1,2,3$, each of them having its own polarization $\mathbf{A}_\alpha$. (The reason why polarization vectors are here denoted having subscripts α instead of subscripts β introduced earlier will become clear from the following discussion). Considering only monochromatic waves, integration over ω can be omitted as well as harmonic dependence on time:

$$\mathbf{u}(x,y,z)=\int_{-\infty}^{\infty}\int_{-\infty}^{\infty}\sum_{\alpha=1}^{3}a_\alpha(k_x,k_y)\mathbf{A}_\alpha(k_x,k_y)\exp[i\,k_z^\alpha(k_x,k_y)z]\exp[i(k_x x+k_y y)]dk_x dk_y\,. \tag{9.1.5}$$

The solution of the problem (9.1.1) written in a form of (9.1.5) clearly indicates its connection to a Fourier transform. Putting z = 0 we obtain

$$\mathbf{u}(x,y,0)=\int_{-\infty}^{\infty}\int_{-\infty}^{\infty}\mathbf{U}_0(k_x,k_y)\exp[i(k_x x+k_y y)]dk_x dk_y\,. \tag{9.1.6}$$

where the Fourier expansion coefficients $\mathbf{U}_0(k_x,k_y)$ are related to polarizations of different modes

$$\sum_{\alpha=1}^{3}a_\alpha(k_x,k_y)\mathbf{A}_\alpha(k_x,k_y)=\mathbf{U}_0(k_x,k_y)\,. \tag{9.1.7}$$

The expansion coefficients are obtained directly from the field distribution $\mathbf{u}(x,y,0)$ across the initial plane as

$$\mathbf{U}_0(k_x,k_y)=\int_{-\infty}^{\infty}\int_{-\infty}^{\infty}\mathbf{u}(x,y,0)\exp[-i(k_x x+k_y y)]\,dx\,dy\,. \tag{9.1.8}$$

The plane wave decomposition (9.1.5) relates a displacement $\mathbf{u}(x,y,z)$ at an arbitrary point of space to the field distribution $\mathbf{u}(x,y,0)$ over the plane z=0. In application to the TIRUS design, this enables a 3D sound field distribution in the sensor body to be calculated provided its distribution across the transducer area is given. A most efficient way to calculate a full 3D field is to compose it from a set of planes parallel to the boundary plane z=0. In this case, the field distribution across every such a plane can be calculated numerically by means of the fast Fourier transform using (9.1.5).

The wave propagation over the distance z can be viewed as an effect of a linear filter described by a complex response function $\exp[i\,k_z^\alpha(k_x,k_y)z]$ applied to a Fourier decomposition of an original field distribution.

This filter affects each possible polarization mode $\mathbf{A}_\alpha(k_x, k_y)$ differently, therefore a Fourier expansion of the original field $\mathbf{U}_0(k_x, k_y)$ should be decomposed into just these polarizations. Coefficients $a_\alpha(k_x, k_y)$ in the equation (9.1.7) are projections of vector $\mathbf{U}_0(k_x, k_y)$ onto a not necessarily orthogonal coordinate system made out of polarization vectors $\mathbf{A}_\alpha(k_x, k_y)$. They can be found [36] from a matrix equation

$$\begin{bmatrix} a_1 \\ a_2 \\ a_3 \end{bmatrix} = \begin{bmatrix} A_x^1 & A_x^2 & A_x^3 \\ A_y^1 & A_y^2 & A_y^3 \\ A_z^1 & A_z^2 & A_z^3 \end{bmatrix}^{-1} \begin{bmatrix} U_x^0 \\ U_y^0 \\ U_z^0 \end{bmatrix}. \tag{9.1.9}$$

Generally, polarization vectors $\mathbf{A}_\alpha$ in this expression are not mutually orthogonal, unlike polarizations $\mathbf{A}_\beta$ obtained by solving Christoffel equation (9.1.3). It is connected with the difference between an approach used to study propagation of plane elastic waves in crystals and that used to decompose a given distribution of a wave field on a plane into a sum of plane waves that contribute to this distribution. The latter is just a problem considered here. In the first case, *a specific selected direction in a crystal is considered* and the solving a wave equation (9.1.1) gives three solutions in a form of three plane waves with mutually orthogonal polarizations. In the second case, *all plane waves in the crystal having the same components k_x, k_y of their wave vectors are considered*, and these waves, generally, can belong to different "branches of the wave field" having different propagation directions determined by different slowness surfaces. As a result, their polarizations are not orthogonal. Thus, specification of k_x and k_y necessary as a first step in decomposition of a given field distribution into a plane waves spectrum leads to three different propagation direction of its components, which is illustrated in Fig. 9.1.2.

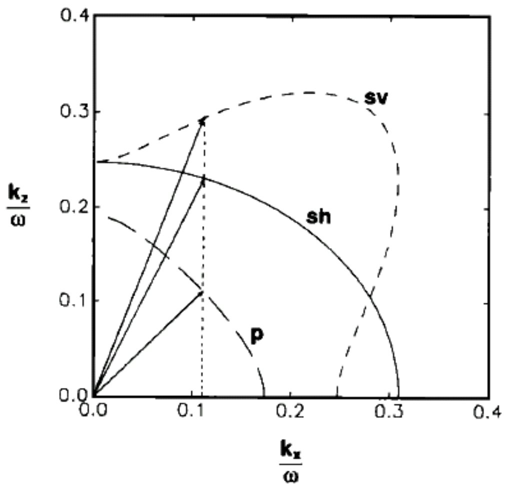

Fig. 9.1.2. Acoustic modes to be taken into account in the plane wave decomposition. Given a component k_x, three plane waves with different polarizations propagating in different direction have to be considered. The image is taken from [35].

9.1.3 Boundary Conditions in Terms of a Traction Force

In the plane wave decomposition method the source can be represented as a predetermined displacement field defined in a restricted area on the crystal surface. But such representation is not absolutely accurate because the displacement field outside the area is assumed to be zero. In reality, the outside region usually is a free surface that does not restrict movement of body particles. The correct way is to specify the source not by a displacement of particles, but as a force applied to the surface. In this case, the force outside the transducer region can be assumed to be zero that corresponds to the correct boundary condition for the free surface. The plane wave decomposition method can be extended to specify boundary conditions in terms of a *traction force* on the boundary plane [32].

The boundary conditions for displacements can be reformulated for forces by using the stress-strain law

$$\sigma_{ij} = c_{ijkl} \frac{\partial u_k}{\partial x_l} . \tag{9.1.10}$$

A traction force at a boundary interface is

$$\tau_i = \sigma_{ij} n_j \tag{9.1.11}$$

Let us find a traction force caused by the plain wave. A displacement field of the plane wave is described by a relation

$$\mathbf{u}(\mathbf{x}) = \mathbf{A} \exp(i\, \mathbf{k} \cdot \mathbf{x}) , \tag{9.1.12a}$$

$$u_i = A_i \exp[i(k_1 x_1 + k_2 x_2 + k_3 x_3)] . \tag{9.1.12b}$$

and has following coordinate derivatives

$$\frac{\partial u_k}{\partial x_l} = A_k\, k_l \exp[i(k_1 x_1 + k_2 x_2 + k_3 x_3)] . \tag{9.1.13}$$

Substitution of the derivatives into the stress-strain law gives

$$\tau_i (x_1, x_2, x_3) = c_{ijkl}\, k_l\, A_k\, n_j \exp(i\, (k_1 x_1 + k_2 x_2 + k_3 x_3)) . \tag{9.1.14}$$

Dropping coordinate dependence to simplify notation we get the traction force as the following tensor product

$$\boldsymbol{\tau} = \mathbf{c} \cdot \mathbf{k} \cdot \mathbf{A} \cdot \mathbf{n} . \tag{9.1.15}$$

As seen from (9.1.15), the traction force $\boldsymbol{\tau}$ at the interface and the polarization vector $\mathbf{A}$ of the plane wave are related by fairly simple expression. This demonstrates that amplitudes of plane waves may be found both for boundary conditions specified in terms of the displacement and for conditions in terms of traction forces at the source plane. Analogously to (9.1.9), amplitudes of the angular spectrum plane waves for boundary conditions specified as tractions can be found using

$$\begin{bmatrix} a_1 \\ a_2 \\ a_3 \end{bmatrix} = \begin{bmatrix} \tau_x^1 & \tau_x^2 & \tau_x^3 \\ \tau_y^1 & \tau_y^2 & \tau_y^3 \\ \tau_z^1 & \tau_z^2 & \tau_z^3 \end{bmatrix}^{-1} \begin{bmatrix} T_x^0 \\ T_y^0 \\ T_z^0 \end{bmatrix} , \tag{9.1.16}$$

where τ_x^α, τ_y^α, τ_z^α are components of vector $\boldsymbol{\tau}_\alpha = \mathbf{c} \cdot \mathbf{k}_\alpha \cdot \mathbf{A}_\alpha \cdot \mathbf{n}$ found for each of three different polarization modes $\mathbf{A}_\alpha (k_x, k_y)$; T_x^0, T_y^0, T_z^0 are components of vector $\mathbf{T}_0 (k_x, k_y)$ that defines Fourier spectrum of traction force specified at the boundary. As one can see, the expressions for amplitudes of the angular spectrum components for displacement boundary conditions (9.1.9) and traction conditions (9.1.16) differs only in the transform matrix. This enables the same field calculation algorithm to be used for both types of quantities at the boundary.

Relation (9.1.16) along with representation (9.1.5) helps finding distribution of the displacement field given the traction force at the source plane. Similarly, the stress tensor can be found from the plane-wave spectrum. It can be done with the help of the Fourier-transformed stress tensor components defined as

$$\mathbf{\Sigma}(k_x,k_y) = \sum_{\alpha=1}^{3} \mathbf{c}\cdot\mathbf{k}_\alpha \cdot \mathbf{A}_\alpha\, a_\alpha(k_x,k_y)\,, \tag{9.1.17}$$

where $a_\alpha(k_x,k_y)$ is a complex amplitude of mode α in the angular spectrum of the displacement field, $\mathbf{k}_\alpha$ and $\mathbf{A}_\alpha$ are the corresponding mode wave vector and polarization. To change (9.1.17) into coordinate representation, each of the stress tensor components $\Sigma_{ij}(k_x,k_y)$ should be inverse-Fourier-transformed. Note also that for obtaining coefficients $a_\alpha(k_x,k_y)$ from the arbitrary displacement field spectrum $\mathbf{U}(k_x,k_y)$, the mode decomposition similar to (9.1.9) should be done. However, this step is redundant if the radiated field is modeled with the plane wave decomposition (9.1.5), in which propagation of each wave mode is considered separately.

Representing the stress tensor components by their Fourier spectra (9.1.17) has an advantage over using general equation (9.1.10), because it allows calculation of stresses directly from the angular plane wave spectrum and avoids calculation of spatial derivatives of the displacement field distribution.

Summarizing, the formulated relation between the angular spectra of displacement and stress fields provides a calculation technique with boundary conditions defined in terms of traction forces at the boundary interface that allows one to calculate a radiation field of the transducer easily.

9.2 The Stroh Formalism for Modeling Ultrasonic Beams

The Stroh formalism is a convenient approach to solving many dynamic problems where wave vectors and wave polarizations need to be found given only a projection of the wave vector on a plane. It deals with the situation when solutions of the three-dimensional problem are sought as functions depending only on two coordinates, so reducing the problem to the two-dimensional case. The method allows finding plane waves that satisfy the wave equation (9.1.1) by solving an eigenproblem [37, 38]

$$\hat{N}\,\xi_\alpha = p_\alpha \xi_\alpha\,, \tag{9.2.1}$$

where $\hat{N}$ is a specially built matrix that depends on a given wave vector projection (components of matrix $\hat{N}$ can be found in [38]). The wave vector projection is defined by its orientation $\mathbf{m}$ and length $k_{\|} = \sqrt{k_x^2 + k_y^2}$. As far as only two components k_x, k_y of the wave vector are given, a real orientation of sought plane waves is not known and should be found by solving the eigenproblem. A unit vector $\mathbf{m}$ that defines an orientation of the wave vector projection lies in the plane of interest defined by its normal $\mathbf{n}$. This plane usually coincides with a real interface between considered media, but it is not necessary so – the theory remains valid for any arbitrary choice of a plane. The eighenproblem (9.2.1) always has six solutions [37, 38]. Six eigenvalues p_α determine missing components k_z of six wave vectors

$$k_z^{\alpha} = p_{\alpha} k_{\|}, \ \alpha = 1,...,6 . \tag{9.2.2}$$

Corresponding eigenvectors consist of two parts $\mathbf{A}_{\alpha}$ and $\mathbf{L}_{\alpha}$, each part being a vector value

$$\xi_{\alpha} = \begin{pmatrix} \mathbf{A}_{\alpha} \\ \mathbf{L}_{\alpha} \end{pmatrix}, \ \alpha = 1,...,6 . \tag{9.2.3}$$

The first vector $\mathbf{A}_{\alpha}$ determines displacement polarization of the found plane waves

$$\mathbf{u}_{\alpha}(\mathbf{r},t) = \mathbf{A}_{\alpha} \exp[i(k_{\|}[\mathbf{m} + p_{\alpha}\mathbf{n}]\mathbf{r} - \omega t)] . \tag{9.2.4}$$

The second vector $\mathbf{L}_{\alpha}$ determines traction force caused by the mode α on the plane of projection

$$\boldsymbol{\tau}_{\alpha}(\mathbf{r},t) = -ik_{\|}\mathbf{L}_{\alpha} \exp[i(k_{\|}[\mathbf{m} + p_{\alpha}\mathbf{n}]\mathbf{r} - \omega t)] . \tag{9.2.5}$$

Among the six found waves there may be both homogeneous and inhomogeneous waves. Homogeneous solutions correspond to bulk waves usually considered in infinite space. Inhomogeneous solutions have exponentially increasing (decreasing) amplitudes, and this means that in an unlimited space they will grow to infinity, which is physically meaningless. But if a physical boundary is present in the space, inhomogeneous solutions take on a meaning and can describe evanescent components of a field in the vicinity of the emitting transducer or surface waves. In this case, among all the mathematically possible solutions only those inhomogeneous waves that decay while propagating into the medium should be selected. Similarly, only those bulk waves that carry energy from the boundary into the medium are of interest in the task of radiation. Therefore, among the six mathematically possible solutions only three ones corresponding to physical aspects of the problem are selected. It is perfectly possible that the selected solutions will contain a mix of homogeneous and inhomogeneous waves.

Note that the Stroh approach does not define actual amplitudes of waves, it only answers the question of what types of plane waves are *possible* in a medium given a projection of the wave vector on the plane of interest. Representation based on projections of the wave vector is very useful for solving diffraction problems. It allows finding k_z components of wave vectors in an easy way, which is necessary to expand a source field given on the plane into an angular plane wave spectrum (9.1.5).

The way in which a traction force is defined in solution (9.2.5) makes the described technique particularly suitable for solving reflection and transmission problems at the boundary. It enables boundary conditions on the interface to be determined immediately.

Thus, even though Stroh formalism does not deal with any boundary condition directly, it proves to be very useful for solving all kind of problems where boundary conditions are defined on some plane. It suits both for the case of a real plane boundary between media and of an imaginary plane inside the medium.

9.2.1 Application of Stroh Formalism to the Diffraction Problem

Modeling of ultrasonic field propagation with angular plane wave decomposition integral (9.1.5) requires finding *z*-components of the wave vector along with mode polarizations for each projection of the wave vector on the source plane. Amplitudes of plane waves found from boundary conditions also require finding polarization vectors to perform a projection onto a basis as it is done in (9.1.9) for displacements or in (9.1.16) for traction forces. Eigenproblem (9.2.1) formulated in the Stroh approach allows to solve this task immediately providing orientation of a boundary plane and two components k_x, k_y of the wave vector lying in this plane. Missing *z*-components of the wave vector are determined from eigenvalues (9.2.2) and mode polarizations are obtained from (9.2.3).

Equation (9.2.1) produces six solutions, from which only three have to be selected and used for calculation of the field distribution. Selected solutions have to meet criteria of transferring energy from the source plane into the medium (for bulk waves) or to decay during propagation into the medium (for inhomogeneous waves). It is imperative that both homogeneous and inhomogeneous waves have to be considered for decomposition of a source field into the angular plane wave spectrum. Homogeneous solutions are obviously included because they correspond to bulk waves. Inhomogeneous solutions describe those components of the source field that cannot propagate in the medium as bulk waves, but nevertheless are generated by the source excitation. The source is represented as an arbitrary distribution of the field at the boundary plane. Being arbitrary, such a distribution may contain spectral components that correspond to inhomogeneous waves which therefore have to be present in the decomposition to satisfy imposed boundary conditions.

Eigenvalues p_α obtained by solving (9.2.1) can be either real or complex. In the case of being real, they correspond to propagating bulk waves and a direction of energy propagation can be found by projection of the Pointing vector $\mathbf{P}_\alpha$ onto the plane normal **n**

$$\mathbf{P}_\alpha \cdot \mathbf{n} = -\frac{\omega k_\parallel}{2}(\mathbf{A}_\alpha \mathbf{L}_\alpha^* + \mathbf{A}_\alpha^* \mathbf{L}_\alpha) > 0\,, \tag{9.2.6}$$

where symbol * denotes complex conjugation and positive projections are sought solutions. Complex eighenvalues correspond to inhomogeneous waves. They always come in complex-conjugated pairs, so one value corresponds to a wave with an increasing amplitude, whereas the other corresponds to a decaying inhomogeneous wave. Obviously, only latter solutions have to be selected and this can be done by inspecting a sign of the imaginary part

$$\mathrm{Im}[p_\alpha] > 0\,. \tag{9.2.7}$$

Using criteria (9.2.6) for real eigenvalues and (9.2.7) for complex ones, one can determine a proper 3D basis formed out of the plane wave polarizations $\mathbf{A}_\alpha$ in decomposition (9.1.5). The same basis should be used to find amplitudes of plane waves from displacement boundary conditions using (9.1.9) or from the traction boundary conditions using (9.1.16).

9.2.2 Using the Stroh Formalism to Find a Field After Reflection

The sensitive face of the TIRUS is the crystal face where reflection of the sound beam occurs. The configuration of the sensor was specially designed to avoid mode conversion on reflection, but it was developed using a very simple model of a plane wave reflecting from a plane surface. In reality, the beam has a complex field distribution and should be represented by a whole spectrum of plane waves incident on the boundary. Some components of this angular spectrum can possibly be reflected in a specific way, so an additional analysis is necessary to confirm that the reflection process does not deteriorate the beam upon reflection.

To find reflection and transmission coefficients for a plane wave incident on a boundary interface between two media, a conventional procedure [5] can be applied. This procedure implies finding wave vectors of the involved plane waves that are to have equal projections onto the interface. In this context, the Stroh approach is readily applicable to solving this task, because it operates with waves having specified projections of wave vectors. Wave vectors and polarizations of waves involved into reflection (or refraction) from the interface can be easily found by solving eigenproblem (9.2.1). Its solution produces six roots, but for a given orientation of the boundary plane, only three waves are selected for each half-space taking into account consideration of the energy flow. For the refraction problem, the adjacent media are on both sides of the interface, therefore two different eigenproblems should be solved for each medium separately. In the case of reflection from a free surface, one eigenproblem is solved. Three solutions of this eigenproblem are associated with incident waves and other three with reflected waves. Reflection and transmission coefficients can be then calculated using obtained polarizations of acoustic modes by means of solving a system of equation composed to satisfy proper boundary conditions.

In addition, in the case of a free surface, the only boundary condition to be satisfied is that mechanical traction must be zero over all the surface of interest:

$$\sigma_{ij} n_j = 0 . \tag{9.2.8}$$

This means that the sum of traction forces caused by all incident and reflected waves should be equal to zero.

For each projection of the wave vector specified by its components k_x, k_y there will be three different plane waves from the angular plane wave representation with different component k_z^α. These waves should be considered simultaneously as three incident waves generating three reflected waves. Amplitudes of incoming waves a_α are assigned by components of the angular spectrum, and amplitudes of reflected waves are to be found. After finding amplitudes of reflected components, the reflected beam can be reconstructed in a usual way as a Fourier integral over all plane waves.

The traction force in equation (9.2.8) could be calculated from polarizations and amplitudes of the found waves using the stress-strain relation (9.1.10), but there is no need to do it this way. The Stroh formulation provides a necessary traction force as eigenvalue component $\mathbf{L}_\alpha$ (9.2.3), so equation (9.2.8) may be rewritten as

$$\sum_{\alpha=1}^{3} a_\alpha \mathbf{L}_\alpha^i + \sum_{\alpha=1}^{3} b_\alpha \mathbf{L}_\alpha^r = 0 , \tag{9.2.9}$$

where b_α are amplitude coefficients of the reflected waves, $\mathbf{L}_\alpha^i$ and $\mathbf{L}_\alpha^r$ are traction parts of eigenvectors. All traction vectors for incoming $\mathbf{L}_\alpha^i$ and reflected $\mathbf{L}_\alpha^r$ waves are found from the same eigenproblem (9.2.1) and are intermixed between six eigenvectors. Three vectors for incident waves are to be separated from the three associated with reflected waves using criteria based on consideration of energy flow. Real-valued solutions corresponding to bulk waves are selected using the criterion (9.2.6) derived earlier, while complex-valued solutions are selected using (9.2.7). Being real-valued or complex-valued (or both), selected eigenvectors correspond to three reflected, i.e., outgoing waves. Due to the symmetry of the task, other three eigenvectors correspond to the incoming waves.

System of equations (9.2.9) can be reformulated in a matrix form as

$$\begin{pmatrix} L_{1x}^r & L_{2x}^r & L_{3x}^r \\ L_{1y}^r & L_{2y}^r & L_{3y}^r \\ L_{1z}^r & L_{2z}^r & L_{3z}^r \end{pmatrix} \cdot \begin{pmatrix} b_1 \\ b_2 \\ b_3 \end{pmatrix} = -\begin{pmatrix} [\sum a_\alpha \mathbf{L}_\alpha^i]_x \\ [\sum a_\alpha \mathbf{L}_\alpha^i]_y \\ [\sum a_\alpha \mathbf{L}_\alpha^i]_z \end{pmatrix}. \tag{9.2.10}$$

Quantities b_α can be found by inversion of this matrix equation. They represent amplitudes of plane waves with projections k_x, k_y in the angular plane wave spectrum of the reflected beam. Repeating such calculations for all projections of the wave vectors enables the whole beam reflected from the boundary to be reconstructed. Further propagation of the reflected beam is modeled using already developed the angular plane wave decomposition method.

9.3 Calculation of a 3D Structure of an Ultrasonic Beam in the TIRUS

An approach to modeling of ultrasonic beams radiated into an anisotropic medium from a plane boundary developed in the current project is based on the plane wave decomposition of the displacement field in the crystal. Numerical implementation of the field calculation procedure uses fast Fourier transform which exhibits intrinsic periodicity. This periodicity results in calculation artifacts caused by spatial aliasing: for large propagation distances side lobes of the beam reach boundaries of a calculation region and reappear wrapped on the other sides of the region. The negative effect of the aliasing can be reduced by increasing a size of the calculation region, so that the boundaries are moved away from the region of a high field “concentration”. Such an approach has a drawback because a number of points in the sampling grid should be increased in two dimensions, greatly increasing amount of numerical operations and total calculation time.

An alternative approach that proved to be suitable to mitigate the effect of spatial aliasing was developed in the current work. The main idea behind it is to prevent wrapped components of the field from propagating back to the region of interest. To realize this approach the simulated field was calculated in steps starting from the source plane. At each step, the field was modified (“masked”) with a specific apodization function quickly approaching zero value near the edges of the calculation region. Such a technique resembles application of absorbing boundaries widely used in the FDTD modeling. An illustration of the calculation procedure is presented in Fig. 9.3.1. Each step should be small enough to prevent the wrapped field to develop and to leave a region where masking is performed. After masking done, the calculation should be restarted from the very beginning using the obtained field distribution as a source field. This procedure introduces some additional computational cost. The increase in complexity of calculations can be estimated as a constant factor not greater than 2, because instead of a single Fourier transform we need to perform two ones in each intermediate plane: an inverse transform to recover the field and apply the mask, and a direct transform to resume calculations at the next step. The additional cost can be significantly reduced if apodization is applied not on every calculation plane, but only after some predefined number of steps.

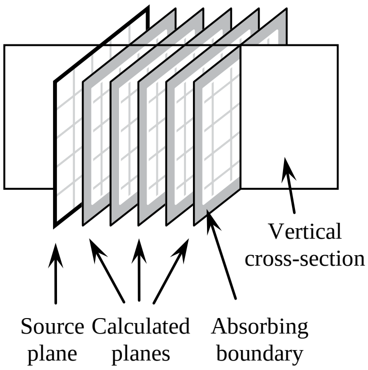

Fig. 9.3.1. Illustration of a calculation procedure for 3D modeling of a radiated ultrasonic beam.

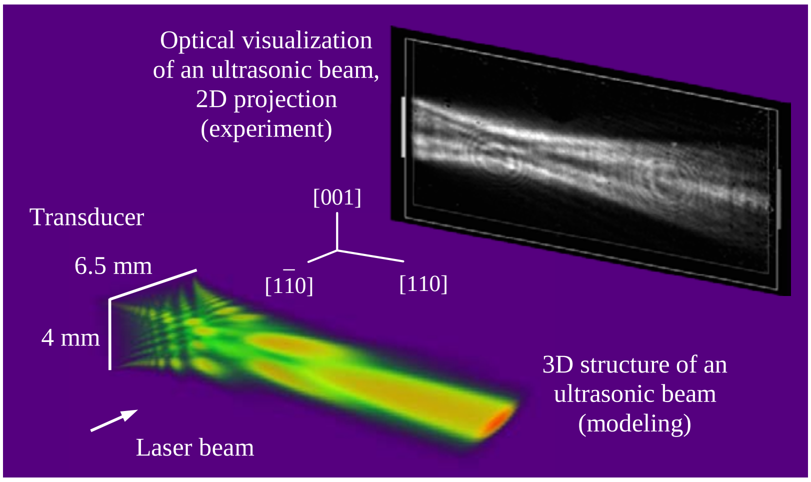

Fig. 9.3.2. 3D distribution of the displacement field of a modeled sound beam. The field shows a good-shaped main diffraction lobe near the right edge. Color palette and transparency settings are arbitrarily adjusted for better visualization of the field. A 2D image of the beam obtained in the optical visualization experiment put in the picture for comparison resembles “an inverse shadow” of the calculated beam structure.

A 3D distribution of the displacement field amplitude in the TIRUS calculated using the described technique is presented in Fig. 9.3.2. It reveals an unexpected at a glance fact of a focusing effect in the direction [001] where the transducer size is smaller and diffraction divergence of the beam has to be greater, which, of course, is a consequence of the crystal anisotropy. For comparison, a two-dimension projection of the actual field visualized in the experiment (see section 8.4.1, Fig. 8.4.2) with an acousto-optic technique is shown in the inset of Fig. 9.3.2. Its structure looks as a projection of the calculated ultrasonic beam although there is an obvious difference between two images: the beam visualized in optical experiments has well noticeable side lobes above and underneath of the main one that are absent in the calculated beam. This difference is only seeming and is connected with the palette chosen for presentation of the 3D image.

9.4 Calculation of Diffraction Losses

One of physical mechanisms contributing to the insertion loss of the TIRUS is diffraction losses caused by the beam divergence and the wavefront distortion of a propagating ultrasonic wave [39]. Therefore a first step in estimating them should be calculation of an ultrasonic field radiated by a transducer. Certainly, the calculation procedure to be used should be validated before its application to a real situation. To verify validity of the developed procedure it was compared with known solutions [40-42] that enabled the validity of the calculation algorithm to be confirmed. After that actual parameters of the medium and the transducer size corresponding to the TIRUS design were used to assess diffraction losses in the sensor. The results obtained are discussed in next sections. A specific result of the current research is computation of the diffraction losses along a two-segment polyline path caused by reflection from an inclined surface, along which the medium properties are essentially different across each of the segments.

A diffraction loss as a numerical quantity can be defined in numerous ways. A source-receiver configuration that has been most widely studied [40-42] consists of a circular transducer radiating a compressional wave into an isotropic solid or fluid with a circular receiver of the same size located at some distance from the source; the diffraction loss is defined as reduction of the average pressure calculated over the receiving area compared to the radiated one. For this case, an explicit analytic expression for the resulting field pressure can be obtained [40], which explains popularity of this configuration. Presence of an anisotropic medium or an asymmetrical source-receiver configuration complicates the analytical solution significantly. Diffraction losses of a longitudinal wave propagating along certain directions in anisotropic solids were considered by Papadakis in [41]. The shear wave diffraction losses in an isotropic solid were analyzed in [42]. The authors considered the shear stress averaged over the receiver (which is the same as the averaged tangential component of a traction force) instead of considering the averaged pressure commonly used for longitudinal waves. Source field at radiating transducer is also defined as a shear stress. There are also works dealing with different geometry of emitting and receiving transducers: rectangular transducers [43], circular transducers of different sizes [44], non-co-axial transducer configuration [45], but they all deal only with the pressure field in an isotropic medium. To the best of our knowledge, there is no publication providing calculation results for the diffraction loss of a shear wave in an anisotropic medium – the task on hand.

In next subsections results of the validation of the calculation procedure against known solutions are provided. The last subsection deals with diffraction losses calculated specifically for the TIRUS.

9.4.1 Validation of the Diffraction Loss Calculation Procedure

Data provided by the articles [40-42] were selected as main sources to validate the developed field calculation algorithm. The first paper contains tabulated values for the compressional wave diffraction loss in an isotropic medium. The second one provides plots of the longitudinal wave diffraction loss for several propagation directions in anisotropic solids. The third paper gives a comparison between diffraction losses for shear and longitudinal waves in an isotropic medium for small values of parameter *ka*, where $k = 2\pi/\lambda$ is the wave vector and *a* is a radius of the radiating area. Usually an approximation is applied to simplify analytical expressions for $ka \to \infty$. Papers [40-41] deal with high-frequency approximation $ka \to \infty$, whereas paper [42] analyze small and intermediate values of parameter *ka* = 10, 20, 50, 100.

9.4.2 Longitudinal Waves in an Isotropic Medium

To model propagation of an ultrasonic beam in an isotropic medium material parameters of fused silica were loaded into the calculation algorithm, although actually used values are of no importance in an isotropic case. The calculated diffraction losses are plotted in normalized coordinates: the source-receiver separation distance *S* is normalized to the wavelength and the transducer size

$$S = z\lambda / a^2, \qquad (9.4.1)$$

where *z* is an actual distance between the receiver and transducer planes. The source field was defined with a stress component corresponding to the longitudinal wave, and stresses obtained at the receiver plane were projected on the same direction as the source force to take into account only longitudinal components. The

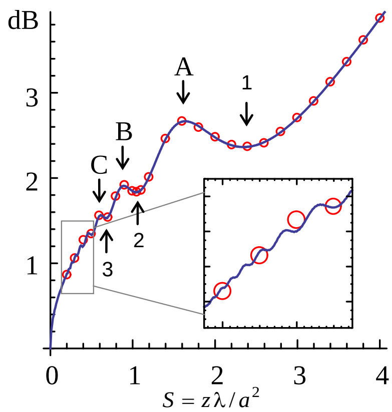

Fig. 9.4.1. Calculated diffraction losses for longitudinal waves in an isotropic medium: comparison with [40]. Our data are shown as a blue line; tabulated values from [40] are shown as red circles.

stresses were averaged over the circular receiver area and normalized to the value at the source plane. The size of the transducers was chosen to correspond to $ka = 100$. The calculated diffraction losses show an excellent agreement with the tabulated values of [40] (Fig. 9.4.1). Besides peaks "A", "B", "C" and minima "1", "2", "3" usually mentioned in cited papers, our calculations show also additional maxima and minima for small values of the parameter *S* (see an inset in Fig. 9.4.1).

9.4.3 Longitudinal Waves in an Anisotropic Medium

Paper by Papadakis and Margetan [41] provides data for the longitudinal wave diffraction losses in a number of anisotropic media. All plots are obtained for the high-frequency approximation $ka \to \infty$. To repeat calculations with our algorithm we used the same material parameters as in their reference list. A comparison was

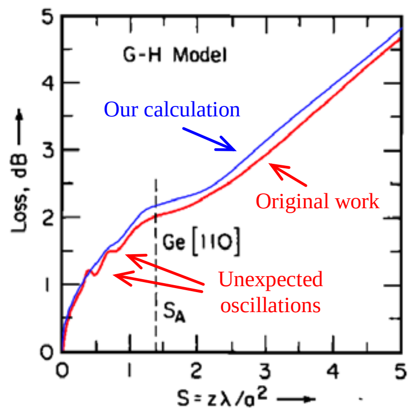

Fig. 9.4.2.Calculated diffraction losses for longitudinal waves in the [110] direction in germanium: comparison with [41]. Discrepancy is seen both in values and in the pattern of near-field oscillations. Original black and white image was colored: original curve for diffraction loss was highlighted in red; our data superimposed as blue line. Captions in color are made by us.

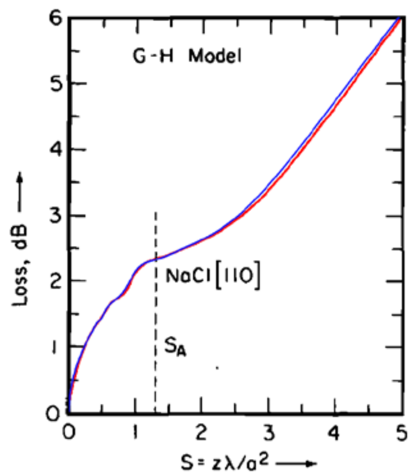

Fig. 9.4.3.Calculated diffraction losses for longitudinal waves in the [110] direction in NaCl: comparison with [41]. Good agreement is seen. The original black and white image was colored: curve for diffraction loss was highlighted in red; our data superimposed as a blue line.

done for several combinations of propagation directions in different crystalline solids: Si [100], Si [111], Si [110], Ge [110], NaCl [110]. All of them show very good agreement of calculated losses with the original curves except only the one. A noticeable discrepancy appears for the [110] direction in germanium (see Fig. 9.4.2). It is not clear what is the reason for that because there is a very good agreement for two other materials, Si and NaCl, for the same direction of the wave propagation (see a plot for NaCl in Fig. 9.4.3), in which case the same result is naturally expected for germanium.

The plot for germanium in the original work [41] shows noticeable oscillations in the near-field region which are absent in the plots for other materials and also do not appear in our calculations. Apparently it could be an error in the original paper, because all three materials have the same cubic symmetry and only the values of material parameters differ. Calculation of the field distribution for the wave propagating in the [110] direction is most difficult among the considered cases because of an asymmetric shape of the slowness surface in its vicinity. Authors of [41] applied the Gauss-Hermit beam expansion method to calculate diffraction losses in this direction. We used an asymmetric grid of 2048×512 points to take into account anisotropic beam spreading when calculated the diffraction loss in the [110] direction, whereas a symmetrical grid of 1024×1024 points was used for other directions. Despite a noticeable difference between results for germanium obtained in [41] and in the current research (Fig. 9.4.2), positions of the inflection points on both curves coincide, which indicates that a significant error in the calculation done is hardly likely.

9.4.4 Shear Waves in an Isotropic Medium

Diffraction loss calculations for shear waves are presented in [42]. The authors come to an important conclusion that for transducers of a large size (*ka*>100) dependence of diffraction losses on the source-receiver separation distance *S* coincide for both longitudinal and shear waves, and a significant difference appears only for small values of *ka*. We calculated the diffraction losses for *ka* = 10 and 20 for both modes to compare them with those provided in the paper. The results obtained for *ka* = 20 show an excellent agreement, which, however, is not so with the results for *ka* = 10 shown in Fig. 9.4.4. Curves for compressional waves in the figure match closely; curves for shear waves show some discrepancy: positions of the peaks are nearly the same and the difference diminishes for larger separations. A possible reason for this discrepancy can be associated with a limited grid resolution for small values of *ka* because a circular source cannot be represented accurately by a rectangular grid used in the developed technique. Why this difference takes place for shear but not for longitudinal waves remains unclear.

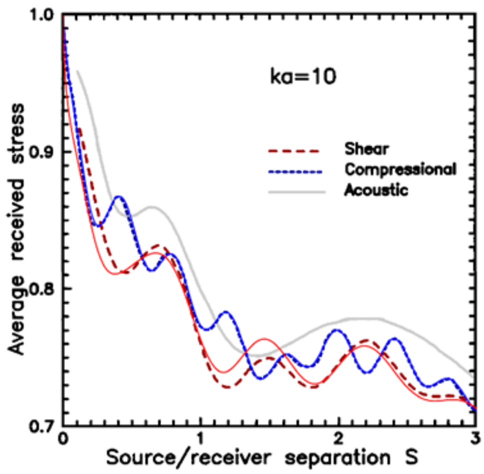

Fig. 9.4.4. Calculated diffraction losses for longitudinal and shear waves in an isotropic medium: comparison with [42]. The original black and white image was modified: dashed curves for shear and compressional waves were colored in red and blue; our data are presented by solid lines. An acoustic solution colored in gray is irrelevant to the task and was not analyzed.

9.4.5 Calculation of the Diffraction Loss in the TIRUS

Diffraction losses in the TIRUS are the part of the sound attenuation due to the beam divergence in the crystalline body of the sensor. A probing ultrasonic beam emitted by the transducer is reflected by the sensor sensitive surface, so the total propagation path can be divided into two regions: one before and another after reflection. Calculation of the diffraction loss before reflection is straightforward. The displacement field is projected onto the $[1\bar{1}0]$ direction and is averaged over a rectangular area equal to the size of the emitting transducer, but located at a distance from the source plane. The situation after reflection is different because a virtual receiver area changes in size due to inclination of the reflecting plane. Its proper boundaries can be determined by a simple geometrical projection of the source boundaries taking into

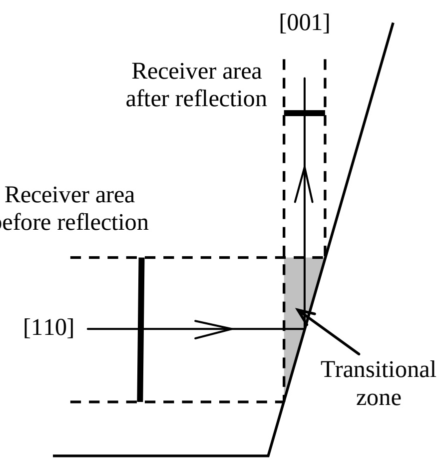

Fig. 9.4.5. The diffraction loss calculation geometry before and after reflection.

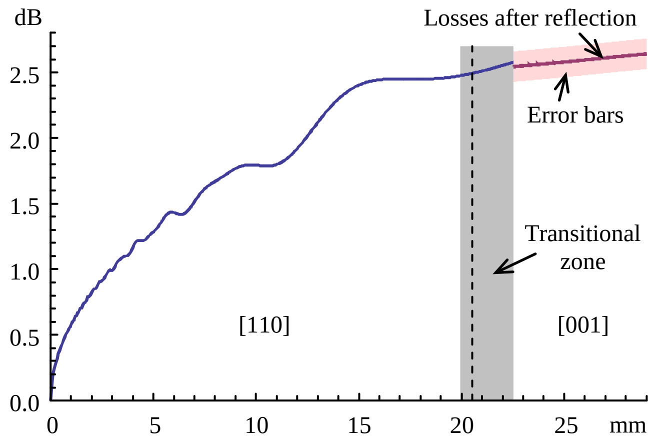

Fig. 9.4.6. The calculated diffraction loss for SH waves in the TIRUS. The propagation distance is measured along the beam central line.

account anisotropic nature of the medium (see Fig. 9.4.5). As illustrated in the figure, there is a transitional zone where diffraction loss cannot be determined in a conventional way because a fragment of the incoming beam already passed reflecting plane but another part of the beam still approaching it. Therefore in computation the losses data in transitional zone are unavailable. Diffraction losses for regions before and after reflection are combined together in Fig. 9.4.6. In calculations, a transitional zone where correct data are not available was filled up with the data calculated for the case with no reflecting plane in presence. The Propagation distance on the plot is measured along the central line of the beam and is expressed in absolute units (millimeters). Normalized coordinate *S* is not applicable here because the wavelength of sound and the beam divergence are significantly different before and after reflection. Losses after reflection can contain considerable calculation errors due to the grid coarsening caused by peculiarities of the calculation algorithm. Magnitude of this errors is estimated by varying a number of points averaged over the receiver area and is presented on the plot as error bars. Error margins for values before reflection are much smaller and do not exceed the line width on the plot. The beam divergence along direction [001] is particularly small, which is indicated by the slope of the loss curve after reflection that is in good agreement with the shape and curvature of the slowness surface in this direction.

A graph of the diffraction loss in Fig. 9.4.6 shows that the field magnitude just after reflection does not differ significantly from the field magnitude before reflection, so the SH wave still carries the major part of the energy. Diffraction losses are determined taking into account both magnitude and phase of the filed, so distortion of the wavefront is also included into consideration. Therefore, a rather small change of diffraction losses observed after reflection confirms indirectly that the wavefront of the reflected beam does not suffer from degradation on reflection. Thus, the computational results show that in the frame of the developed theoretical model large insertion losses observed in the experiments cannot be explained with mode conversion on the reflecting plane.

9.5 Conclusions

The plane wave decomposition method was applied to develop an algorithm suitable for calculation of an ultrasonic beam transmission, propagation and reflection in an anisotropic medium. Calculation of the radiated filed in the TIRUS showed that the beam has a good-shaped main diffraction lobe in the region where reflecting plane is located. This confirms that the sensitive plane is far enough to obtain uniform distribution of the field in a zone where the sensor should contact a tested specimen. Inspection of the field after reflection from a free surface showed no noticeable conversion of the incident shear horizontal wave into other acoustic modes. This means that in the frame of the developed theoretical model unexpectedly large diffraction losses observed in the experiments cannot be explained with mode conversion on the reflecting plane. The total calculated diffraction loss associated with the beam divergence is equal to 2.64±0.12 dB, which is much less than the values observed in the experiment. This poses the problem of finding other physical reasons for such sensor behavior. The developed calculation procedure is not limited to the considered TIRUS configuration and can also be used for calculation of other modes of radiated ultrasonic fields in different anisotropic media.

10 Development of an Approach to Extraction of Reference Data from an Unstable TIRUS Output

List of Symbols

a and **b**	vectors representing multiplicative and additive parts of the sinusoidal model
$C(t)$	random phase part of vector $\mathbf{f}(t)$
$\mathbf{f}(t)$	vector of a periodic component of experimental data
F_n	spectral components of vector $\mathbf{f}(t)$
K	estimation coefficient applied in the testing procedure
$n(t)$	a random function of time
r	correlation coefficient
$R_{\mathrm{Ph}}(k)$	autocorrelation function of the TIRUS output phase
$R_{\mathrm{A}}(k)$	autocorrelation function of the TIRUS output amplitude
Y_m	spectral components of vector $\tilde{\mathbf{y}}^{(1)}$
$\tilde{\mathbf{y}}^{(1)}$	first principal vector determined from experimental data
$\tilde{\mathbf{y}}^{(2)}$	second principal vector determined from experimental data
Ω	frequency of oscillations of the statistical model output

Introduction

As shown in [1], a complex transfer function of the TIRUS has significant instability that makes it difficult to chose a single measured characteristic as a reference that characterizes a sample examined. Results of measurements show that averaged characteristics obtained in different series of measurements differ significantly and a reasonable choice of “a best one” is also difficult. This raises questions about what is the character of the observed differences and whether it is possible to apply a post processing technique for the purpose of making the reference. In the current research, a number of tasks were solved to answer these questions: (1) a statistical analysis of the obtained data sets for the purpose of detection of their general stationary parameters or properties; (2) the building of a mathematical model of an analyzed stochastic process to describe the instability of data acquired; (3) the use of the built mathematical model and application of blind processing techniques to the purpose of reference data extraction; (4) development of an estimation procedure for testing flawless and defected specimens using reference data.

Solving the first two tasks enables to describe an unstable TIRUS output using a sinusoidal model. This significantly simplifies the task of reference data extraction. The discussion of an approach developed is presented in section 10.1.

The third task solved was an application of the Principal Component Analysis (PCA) to an unstable TIRUS output. It has been shown that meaningful results can be obtained under rather strict conditions imposed on raw data sets used as a PCA input. In addition, a spectral analysis based on the Fourier transform of a periodic constituent of the TIRUS output was carried out. The results obtained are presented in Section 10.2.

In the third section, the techniques developed were tested on actual flawless and defected specimens. The results obtained were used for solving the fourth task, building an estimation procedure. The developed procedure proved to be suitable for detection subsurface defects in tested specimens using a single measured TIRUS response.

10.1 Data Analysis and Development of a Mathematical Model

The data used for the following analysis were taken from [1] as ones "ready to use". A representative appearance of measured characteristics is presented in Fig. 10.1.1. As seen from the figure, all frequency responses of the insertion loss measured at successive points of time have the same periodic structure within one series of

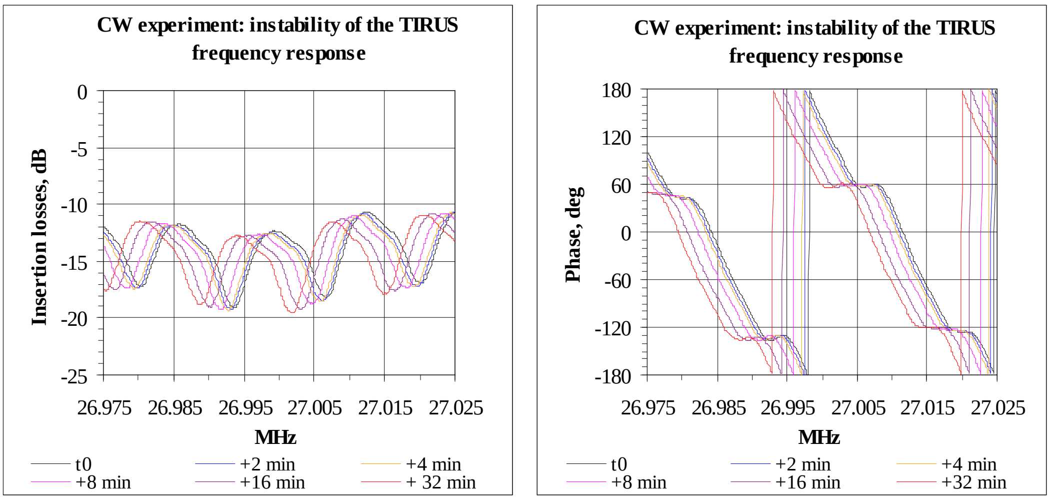

Fig. 10.1.1. Instability of the TIRUS frequency response. The picture is taken from [1].

measurements. It leads to the thought that a mathematical model built should also provide, firstly, a similar structure of its output expressed as a basic periodic function and, secondly, should have a term providing random fluctuations of the output data similar to those observed in the characteristics measured. Then, if a chosen processing technique applied to data generated by the model produces the same basic function that was originally put into the model, it will indicate that this technique actually produces an expected result.

In statistical analysis of the data measured, magnitude and phase of the transfer function were taken from 5 arbitrary records of frequency responses of length of 400 samples each within the frequency range of 26.975÷27.025 MHz. At the stage of data processing, the phase characteristics were unwrapped to exclude phase discontinuities and a specific slope of 58.6º was removed. It is easy to notice that the phase characteristics obtained after processing, as well as insertion losses in Fig. 10.1.1, have an explicit periodic structure. Its period can be determined easily by a position of the second maximum of their autocorrelation functions [46] (Fig. 10.1.2). As seen from Fig. 10.1.2, both autocorrelation functions characterizing the phase $R_{\mathrm{Ph}}(k)$ and amplitude $R_{\mathrm{A}}(k)$ parts of a complex TIRUS output are practically identical for all 5 records taken for analysis and have the same period of 106 samples.

Thus, one can conclude that the experimental data analyzed manifest a periodic pattern that, when measured at different time points, shifts randomly along the abscissa axis keeping its shape. A sinusoidal model similar to the one analyzed in [47] appears to be suitable for modeling such a pattern. In our case, let it be as follows:

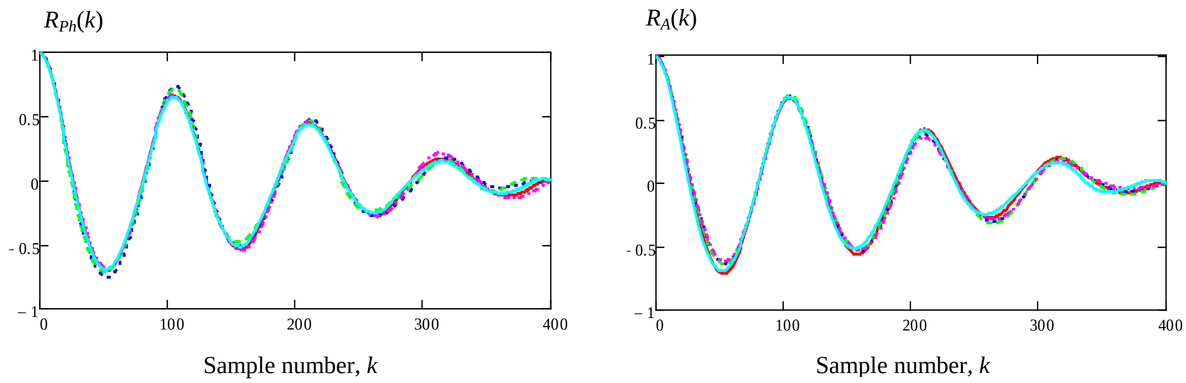

Fig. 10.1.2. Autocorrelation functions of 5 amplitude (right) and phase (left) characteristics taken for analysis.

$$y_k(t) = a_k \sin[2\pi\Omega k + n(t)] + b_k \,, \tag{10.1.1}$$

where $y_k(t)$ are components of the model output vector $\mathbf{y}(t)$ depending on time t, a_k and b_k are components of some unknown vectors **a** and **b** that do not depend on time and determine a multiplicative and an additive parts of the sinusoidal model; Ω is “a conceptual frequency” that is an inverse value of the data pattern period, $n(t)$ is a random function of time.

In the analyzed sinusoidal model the random component affects only a phase of the output obtained that corresponds to random phase shifts observed in the experimental data (Fig. 10.1.1). In this case, a simple approach such as data averaging is not applicable because with a random $n(t)$ having a normal or uniform distribution a result of averaging will sum to zero. Thus, one needs to seek an alternative approach enabling to exclude a random component from the data obtained. In fact, it comes to the blind signal processing techniques in which it is possible to extract vector **y** whose elements characterize a time-independent system. Then vectors **a** and **b** for such a system can be determined using sinusoidal model (10.1.1).

The approach proposed works only if periodic constituents of the examined sensors are pure sinusoids. However, the shapes of extracted periodic constituents of the examined sensors outputs were different and could significantly differ from sinusoidal ones. Moreover, a change in the shape of a constituent could be caused by a defect in a tested specimen and this change in no way had been taken into account by additive and multiplicative vectors of the sinusoidal model. This raised a question of development of a procedure taking into account a shape of the periodic constituent, or, in other words, a question of the change in its spectrum.

For solving this problem the sinusoidal model (10.1.1) was replaced with a new model in which the simplest periodic part of the sinusoidal model is replaced with a more complicated function mapping a periodic part of experimental data. It is presented in a form

$$\mathbf{y}(t) = \mathbf{a}\cdot\mathbf{f}(t) + \mathbf{b} \,, \tag{10.1.2}$$

where $\mathbf{f}(t)$ is a vector of a periodic constituent of experimental data with components $f_k(t)$; phase shifts between its realizations produce a random function of time that represents an unstable character of the TIRUS output.

In the currently developed procedure for reference data extraction, the periodic constituent $\mathbf{f}(t)$ is introduced by means of the inverse complex discrete Fourier transform [48]:

$$f_k(t) = \sum_{n=0}^{N-1} F_n \cdot e^{i\left(\frac{2\pi}{N}k + C(t)\right)n}, \tag{10.1.3}$$

where N is a number of components of vector $\mathbf{f}(t)$, F_n is a complex amplitude of the vector $\mathbf{f}(t)$ spectrum, which is defined as $F_n = |F_n| \cdot e^{i\varphi_n}$, where φ_n is an initial phase of n-th spectral component and $|F_n|$ is its magnitude. The right hand of equation (10.1.3) is modified in its phase part by term $C(t)$ to take into account a random character of vector $\mathbf{f}(t)$ manifesting itself as a changing in time random shift of a measured frequency characteristic across the range of measurement:

Unlike the sinusoidal model, in the model (10.1.2) vector of the periodic constituent of experimental data $\mathbf{f}(t)$ is not an unchangeable one and together with vectors **a** and **b** can play a role of the sensor identifier. In this case magnitudes of the $\mathbf{f}(t)$ harmonics can serve as reference data identifying the sensor if they are computed from data obtained while testing the sensor itself with no tested specimens at its sensitive surface. In such an approach, random phase shifts $C(t)$ do not disturb reference data because they do not affect the spectrum magnitudes.

10.2 A Procedure for Extraction of Reference Data

10.2.1 Application of the Principal Component Analysis to the Data Processing

In the blind signal processing, the Principal Component Analysis is the most widely spread technique [49]. The PCA technique is applied to reduce a dimension of space of the observed vectors of experimental data without essential loss of information. Let **x** be a vector of an initial set of vectors in a linear space $\mathbf{R}^n$. Application of the PCA enables transition to a basis of a new space such that a first component (a first vector of its basis) determines a direction with a maximum dispersion amongst the original vectors. The second vector of the new basis is chosen in such a way that dispersion of the original vectors along it is maximum and it itself is orthogonal to the first vector of the new basis. Other new basis vectors are constructed similarly. As a result, a basic variability of the original vectors is mainly mapped by several first (principal) components in the new space, and there is a possibility to move into a space of less dimension omitting less essential components.

Mathematically, the result of application of PCA is expressed as calculation of a matrix **W** of $m \times n$ size that maps vectors of the space $\mathbf{R}^n$ into the subspace $\mathbf{R}^m$ spanned by the principal components

$$\tilde{\mathbf{y}} = \mathbf{W}(\mathbf{y} - \boldsymbol{\mu}), \quad \tilde{\mathbf{y}} \in \mathbf{R}^m, \mathbf{y} \in \mathbf{R}^n, \tag{10.2.1}$$

where $\mathbf{y}$ is a vector from the original set, $\tilde{\mathbf{y}}$ is a vector in the subspace of principal components, $\boldsymbol{\mu}$ is a mean vector of the original set.

As mentioned above, PCA is a technique meant to reduce amount of data or, what is the same, a number of variables. So the question arises of how many components one needs to select and which a component should be chosen as a principal one. To answer the question a number of experiments were carried out with the model (10.1.1).

Samples from the several series of data generated by the model (10.1.1) were taken as the test ones in which the components of the vector **a** were specified as polynomials

$$a_k = A_1 k^3 + A_2 k^2 + A_3 k + A_4, \tag{10.2.2}$$

where A_1, A_2, A_3 and A_4 are some arbitrary coefficients. In the first place, a case was considered when **b**=0. All constants in (10.2.2) were chosen in such a way that components of the vector **a** were rendered as shown in Fig. 10.2.1 when the random function $n(t)$ in (10.1.1) was taken to be zero.

The testing was carried out in the LabVIEW environment. While testing the model with a non-zero $n(t)$, a generator with a normal distribution (Fig. 10.2.2 (*a*)) was used. Despite that, it resulted in the distribution at the output essentially different from the normal (Fig. 10.2.2 (*b*)).

In the course of modeling, 400 samples of the model output producing one data vector were generated. Such vectors were generated several times in succession and the set obtained formed the set of the input vectors **x** for the PCA technique. After processing, a set of output vectors **y** was formed by the principal components extracted from the input data. Such principal components proved to be only two.

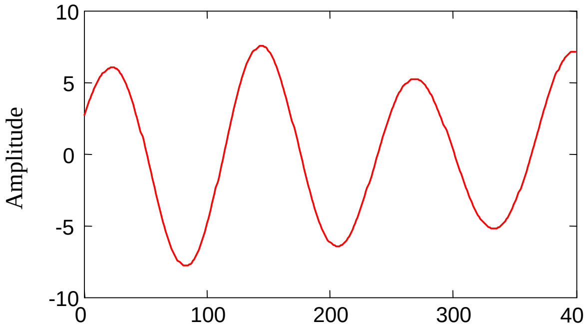

Fig. 10.2.1. Initial characteristic used to test applicability of the PCA technique.

In the processing procedure, different numbers of input vectors were tried. When number of vectors was small (less than 15), the principal components obtained were rather unstable that manifested itself as random phase shifts. On the other hand, the phase shift between them was steady and equal to $\pm\pi/2$ (that is, ~26 samples on the abscissa axis). The frequency of their periodic part and envelops of their amplitudes resembled exactly the input frequency Ω and the data set of the original vector **a**. This is confirmed by features of their cross-correlation functions $R(k)$ presented in Fig. 10.2.3.

When number of vectors was 16 or more, a position of the principal components became stable and further increase in number of vectors caused only random phase shifts of them by $\pm\pi$. It is worth noting that neither of two principal components coincided with the original vector but, as seen in Fig. 10.2.4, they lay symmetrically around it with the phase shift of $\pm\pi/4$. As a result, both principal components can be used to extract the original vector **a**. The results obtained in experiments with the model show that a positive result with real data from TIRUS samples might well be expected.

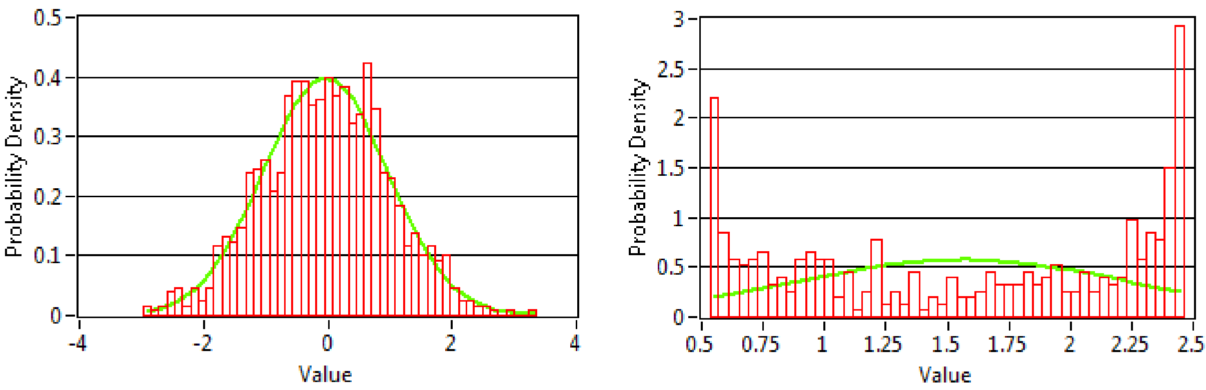

(*a*) (*б*)

Fig. 10.2.2. Distribution of the generated random function $n(t)$ (*a*) and that of the model output (*b*).

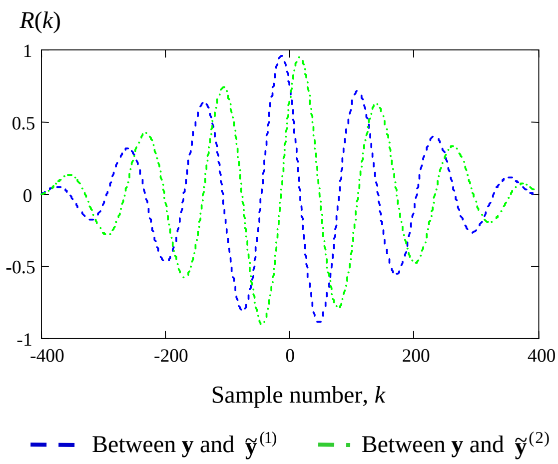

Fig. 10.2.3. Cross-correlations between the initial characteristic and two first principal components.

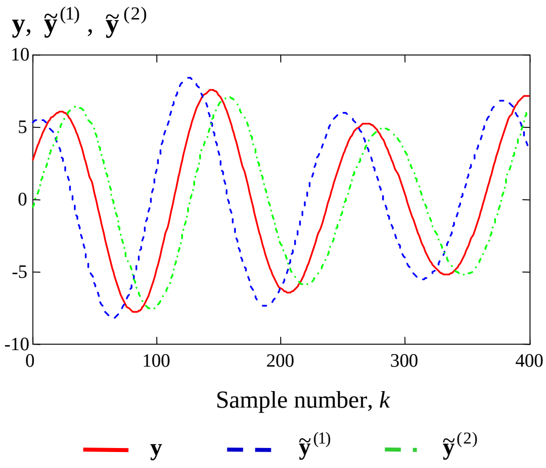

Fig. 10.2.4. A comparison between two first principal components and the initial characteristic.

As was established in simulation, the PCA technique can be effective to remove noise from processed data only in the case when the data set has uniform distribution with a rather large standard deviation (σ>0.5). But for finding a multiplicative or an additive part of the sinusoidal model (10.1.1) complete removal of the noise constituent $n(t)$ is unnecessary. Thus, the condition of having uniform distribution or large standard deviation of the experimental data set is not strict. So, even if experimental data do not have uniform distribution, the PCA technique can be helpful in extracting reference data.

10.2.2 A procedure for Extraction of Reference Data

As noted above, model (10.1.2) will further be used to extract reference data from experimental data. Let us consider the case when the Fourier transform of the periodic vector $\mathbf{f}(t)$ does not depend on time, i.e., there is no random phase shift $C(t)$ in (10.1.3) and changes in vector $\mathbf{y}(t)$ are connected only with changes in vectors **a** and **b** in model (10.1.2). In addition, the k-th components of vectors **a** and **b** have to depend on index k much weaker than components of vector $\mathbf{f}(t)$ (i. e., conditions $da_k/dk << df_k(t)/dk$ and $db_k/dk << df_k(t)/dk$ have to be satisfied); otherwise, extraction of vectors **a** and **b** from the data vector $\mathbf{y}(t)$ is impossible. If the conditions are satisfied, the vector $\mathbf{f}(t)$ of a periodic component of experimental data obtained from the TIRUS itself, with no tested specimen, can be determined using the PCA technique [49] in the following steps. First, the first principal vector $\tilde{\mathbf{y}}^{(1)}$ is extracted from the pre-processed experimental data. Second, an autocorrelation function of $\tilde{\mathbf{y}}^{(1)}$ is calculated, from which a period N_T of the periodic constituent $\mathbf{f}(t)$ is produced. Third, having the period N_T of vector $\mathbf{f}(t)$ known, amplitude components F_n of its spectrum are found by means of removing from the spectrum of vector $\tilde{\mathbf{y}}^{(1)}$ all the components distinct from harmonics of vector $\mathbf{f}(t)$:

$$F_n = \sum_{m=0}^{N_T-1} Y_{p\cdot m}\,\delta(p\cdot m - n), \qquad (10.2.3)$$

where $p = \left\lfloor \dfrac{N}{N_T} \right\rfloor$ is an integer part of the N/N_T ratio, Y_n are components of vector $\tilde{\mathbf{y}}^{(1)}$, δ is the Dirac delta function. Substitution of spectral components F_n found from equation (10.2.3) into equation (10.1.3) yields the sought vector $\mathbf{f}(t)$ calculated at $C(t) = C_0$. The constant phase shift C_0 of the periodic constituent corresponding to vector $\tilde{\mathbf{y}}^{(1)}$ can be then determined with a trial and error technique using a least square approximation of the vector $\tilde{\mathbf{y}}^{(1)}$ data.

The vector of a periodic constituent $\mathbf{f}(t)$ found in such a way is further used to find multiplicative and additive constituents of the model (vectors $\mathbf{a}^{ref}$ and $\mathbf{b}^{ref}$) to be used as reference ones in the post-processing of data obtained while testing defected specimens.

The algorithm of finding vectors $\mathbf{a}^{ref}$ and $\mathbf{b}^{ref}$ is as follows. First, the components of vector $\tilde{\mathbf{y}}^{(1)}$ with indexes of the zero-valued components of vector $\mathbf{f}(t)$ are sought. These components determine corresponding components of vector $\mathbf{b}^{ref}$:

$$b_k^{ref} = \tilde{y}_k^{(1)}\Big|_{f_k(t)=0} . \tag{10.2.4}$$

The remaining components of vector $\mathbf{b}^{ref}$ are determined by approximation with cubic splines of values found using expression (10.2.4). When vector $\mathbf{b}^{ref}$ is determined, components of vector $\mathbf{a}^{ref}$ are sought using (10.1.2):

$$a_k^{ref} = \frac{\tilde{y}_k^{(1)} - b_k^{ref}}{f_k(t)}\Bigg|_{\frac{d f_k(t)}{dk}=0} . \tag{10.2.5}$$

The remaining components of vector $\mathbf{a}^{ref}$ are determined by approximation with cubic splines of values found using expression (10.2.5). Then $\mathbf{a}^{ref}$ and $\mathbf{b}^{ref}$ can be used as reference data to monitor a change in vectors **a** and **b** of the sensor output $\mathbf{y}(t)$ caused by a tested specimen being in touch with the sensor. In this procedure, vector $\mathbf{f}(t)$ should be matched with vector $\mathbf{y}(t)$ by means of the search for the phase shift $C(t)$ as it was described above.

10.2.3 Extraction of Reference Data from an Unstable TIRUS Output on the Base of Spectrum Analysis

Let us consider the case when a periodic vector $\mathbf{f}(t)$ in (10.1.2) depends not only on random changes of phase shifts but also on the parameters of a tested specimen. In particular, it is related to a change in the vector $\mathbf{f}(t)$ spectral content when its period stays the same. This change can be monitored by comparison of vector $\mathbf{f}(t)$ with a reference vector $\mathbf{f}^{ref}$ built on the base of processing of data obtained from the TIRUS itself, with no specimens in a contact with its sensitive surface. An estimator K for monitoring changes can be a measure of energy deviation of spectral components F_n from energy of spectral components F_n^{ref} of the reference vector $\mathbf{f}^{ref}$ normalized to the total energy of the reference vector components:

$$K = \frac{\sum_{n=0}^{N-1} \left| |F_n|^2 - |F_n^{ref}|^2 \right|}{\sum_{n=0}^{N-1} |F_n^{ref}|^2} . \tag{10.2.6}$$

In addition, it is necessary to note that the periodic constituent $\mathbf{f}(t)$ itself of vector $\mathbf{y}(t)$ is determined from equation (10.1.2) after extraction of vectors **a** and **b** by means of the technique described above.

10.3 Processing Experimental Data Using the Technique Developed

Experimental data obtained form TIRUS samples Ug2 and Ug2_2 were taken for the analysis. Each data set consisted of 120 series of individual measurements taken at different times of the day. The length of each data vector obtained from a single measurement was 400, that is, it was the same as in the model examined. Results of one of the measurement series for TIRUS samples Ug2 and Ug2_2 are presented in Fig. 10.3.1.

The analyzed experimental data can be characterized as follows:

- the data have an obvious periodic component and for all data sets a period of the component stays constant and equal to 110 samples. This enables the technique used for the analysis of the previously described sinusoidal model to be applied to the experimental data.
- the data obtained from the same TIRUS sample have a typical random phase shift of the periodic component changing in time that does not cause any essential change in the shape of originally obtained graphs (Fig. 10.3.1). The same is typical for the sinusoidal model as well.

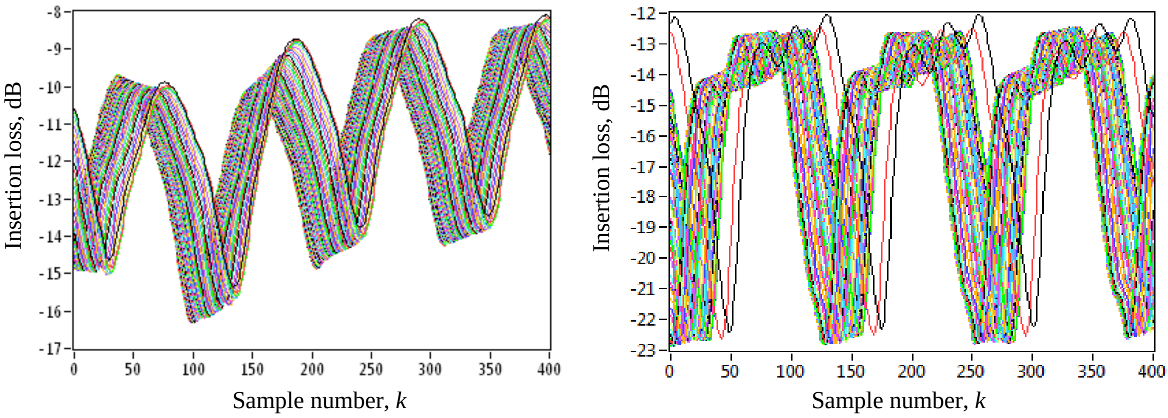

a *b*

Fig. 10.3.1. Frequency responses of the TIRUS samples obtained within one series of measurements; frequency range 26.975÷27.025 MHz, number of samples 400. *a* – sample Ug2, *b* - sample Ug2_2.

Each set of experimental data represents a frequency characteristic of the TIRUS insertion loss measured in the frequency range of 50 kHz around the TIRUS operating frequency of 27 MHz. The actual physical quantities, frequencies, at which the samples were taken in the measurement procedure, have nothing to do with "conceptual frequencies" Ω in the spectra of vectors **a, b, f** and **y** of previous section. Thus, before applying the post-processing procedure to experimental data sets, they were “cleared up” and separated from their actual physical interpretation. Further in this section, the term “frequency” will be used in this “cleared up” meaning.

10.3.1 Extraction of Reference Data from Experimental Data Obtained from TIRUS Samples

The procedure for reference data extraction described in the previous section was tested on the TIRUS samples Ug2 and Ug2_2. The reference vectors were formed using the PCA technique on the base of 120 data sets of individual measurements with 400 samples taken in each one.

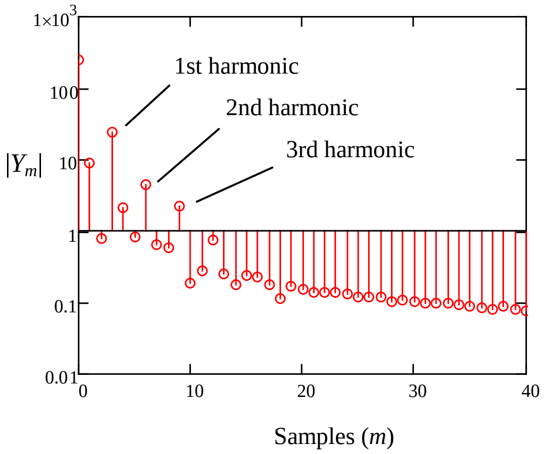

Fig. 10.3.2. Spectral components Y_m of vector $\tilde{\mathbf{y}}^{(1)}$ extracted from data obtained with sensor Ug2.

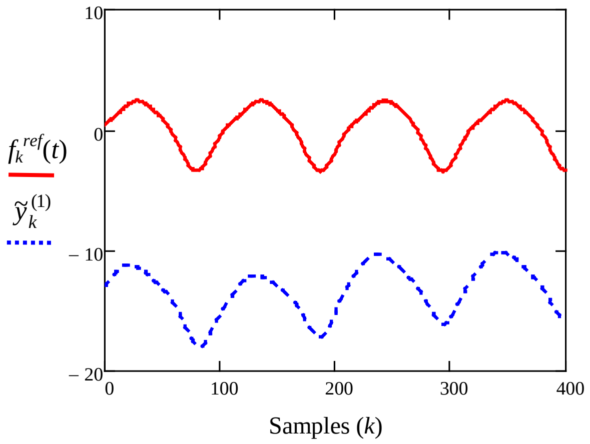

Fig. 10.3.3. Components of vectors $\tilde{\mathbf{y}}^{(1)}$ and $\mathbf{f}^{ref}(t)$ extracted from data obtained with sensor Ug2.

For sensor Ug2, spectral components of vector $\tilde{\mathbf{y}}^{(1)}$ computed in such a manner are presented in Fig. 10.3.2. Vector $\tilde{\mathbf{y}}^{(1)}$ itself and vector $\mathbf{f}^{ref}(t)$ of its periodic constituent computed from the spectrum of $\tilde{\mathbf{y}}^{(1)}$ using (10.2.3) and (10.1.3) are presented in Fig. 10.3.3. For extraction of vector $\mathbf{f}^{ref}(t)$, three first harmonics (samples 3, 6 and 9) that contributed to vector $\tilde{\mathbf{y}}^{(1)}$ mostly were used (Fig. 10.3.2).

For sensor Ug2_2, the similar calculation results are presented in Figs. 10.3.4 and 10.3.5. In this case, four first harmonics (samples 3, 6, 9 and 12), were used for extraction of the periodic vector $\mathbf{f}^{ref}(t)$.

The periods of extracted periodic constituents $\mathbf{f}^{ref}(t)$ for sensors Ug2 and Ug2_2 were 105 and 126 samples respectively. For this reason, the DFT was performed taking into account only three complete periods, i.e., 315 samples for sensor Ug2 and 378 samples for sensor Ug2_2 from 400 samples of computed vectors $\tilde{\mathbf{y}}^{(1)}$ corresponding to each sensor.

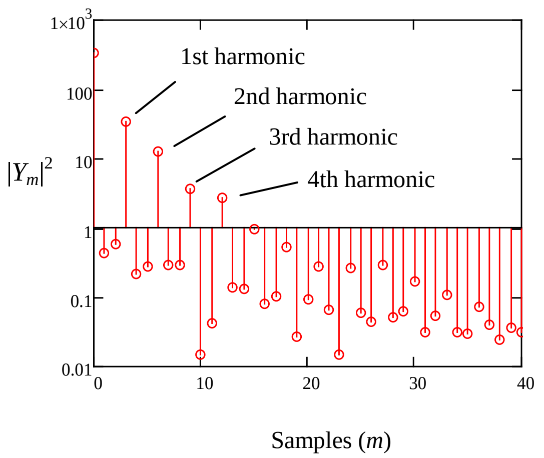

Fig. 10.3.4. Spectral components Y_m of vector $\tilde{\mathbf{y}}^{(1)}$ extracted from data obtained with sensor Ug2_2.

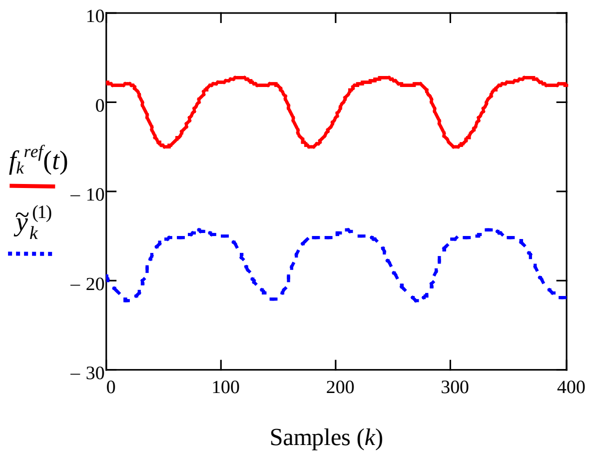

Fig. 10.3.5. Components of vectors $\tilde{\mathbf{y}}^{(1)}$ and $\mathbf{f}^{ref}(t)$ extracted from data obtained with sensor Ug2_2.

10.3.2 Testing the Developed Approach on Real Experimental Data

The developed approach was tested on real experimental data obtained from the TIRUS samples to confirm the possibility of extracting reference data. It was important to understand whether the developed technique is capable of giving the same results when different arbitrarily chosen individual data sets obtained from the same sensor are used as input data. 6 sets of experimental data from the TIRUS sample Ug2 were taken for the analysis; each set consisted of 120 series of individual measurements taken at different times of the day.

According to the model (10.1.2) and to the procedures of the technique described in section 10.2.2, an additive and a multiplicative components were extracted from the experimental data for every data set. Corresponding representative points of the multiplicative components (**a**) and the additive components (**b**) are presented in Fig 10.3.6. They are approximated by cubic splines.

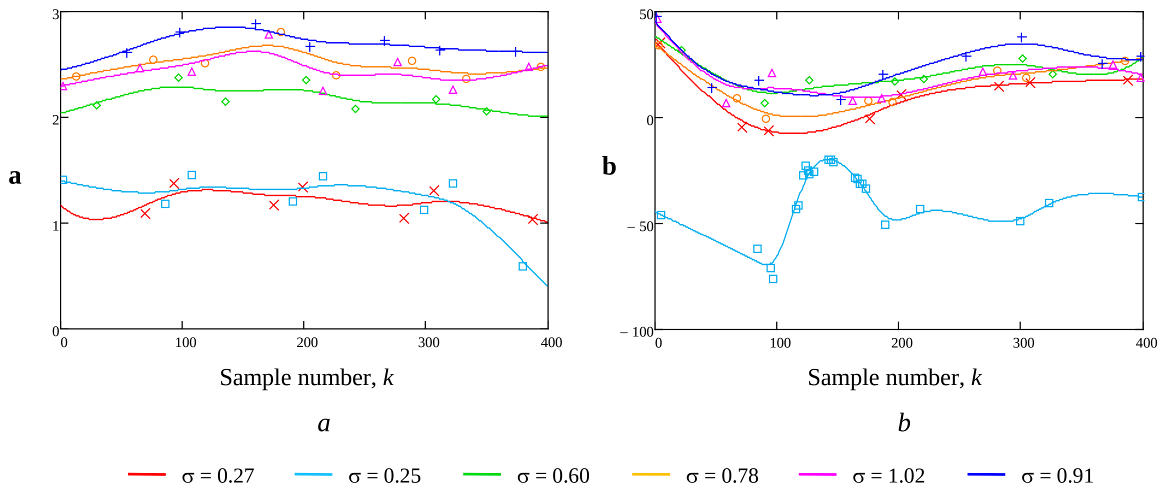

Fig. 10.3.6. Multiplicative (*a*) and additive (*b*) components found from first principal vectors extracted using the PCA technique. Six data sets are used for TIRUS sample Ug2.

Processing of the datasets from sample Ug2 having rather large standard deviation ($\sigma \geq 0.6$) gave similar multiplicative components (Fig. 10.3.6*a*). It is also worth noting that datasets with close values of standard deviations from the same sample gave close values of multiplicative components. Additive components found from the data sets (Fig. 10.3.6*b*) have similar features too. Significant difference between the one of calculated characteristics and the others seen in Fig. 10.3.6 is explained by jumps in measured values present in one of the data sets. These jumps were caused by an experimental setup failure while measuring these characteristics that was revealed already after the data processing had been performed.

Unlike the Ug2 sample, the similar data processing with experimental data from the TIRUS sample Ug2_2 showed that vectors **a** and **b** proved to be scalars, i.e., constants. It illustrates the fact that multiplicative and additive components found from the data sets obtained in experiments with the same TIRUS sample are intrinsic to just this sample. This fact enables to discriminate the samples on hand already at the stage of data processing.

10.3.3 Identification of Defective Specimens Using Reference Data Extracted

Results of processing of a data set obtained from sensor ug2 while testing a defected specimen are presented in detail below. Vector **y**(t) of this data set is shown in Fig. 10.3.7. Vectors of multiplicative and additive constituents $\mathbf{a}$, $\mathbf{a}^{ref}$ and $\mathbf{b}$, $\mathbf{b}^{ref}$ were computed using this vector $\mathbf{y}(t)$ and vector $\tilde{\mathbf{y}}^{(1)}$ computed before. They are shown in Figs. 10.3.8 and 10.3.9; vectors $\mathbf{a}$ and $\mathbf{a}^{ref}$ are normalized.

As seen in Figs. 10.3.8 and 10.3.9, the presence of the defect affects vectors of multiplicative and additive constituents of model (10.1.2) significantly. One can also conclude from Fig. 10.3.8 that vector $\mathbf{a}^{ref}$, characterizing reference data, is, in fact, a scalar (a constant). A quantitative characteristic for comparison of reference data to those obtained in actual testing the specimens can be a difference between components of vectors $\mathbf{a}$ and $\mathbf{b}$ and components of vectors $\mathbf{a}^{ref}$ and $\mathbf{b}^{ref}$. As will be seen below, a suitable estimate of this difference for the multiplicative constituent can be the mean squared difference of their components

$$\left\langle (\Delta\mathbf{a})^2 \right\rangle = \frac{1}{N}\sum_{k=0}^{N-1}\left(a_k - a_k^{ref}\right)^2 , \qquad (10.3.1)$$

and for the additive constituent – the correlation coefficient r.

In this case, a significant difference between the estimations made for a particular data set obtained in a single measurement act and the reference data can be a criterion indicating the presence of a defect. The estimates made for an arbitrary chosen dataset of the sensor Ug2 itself are as follows:

$$\left\langle (\Delta\mathbf{a})^2 \right\rangle_{\mathrm{Ug2}} = 0.017 ; \qquad r_{\mathrm{Ug2}} = 0.962 .$$

The same estimates made for the data set obtained while testing a defected specimen are:

$$\left\langle (\Delta\mathbf{a})^2 \right\rangle = 0.413 ; \qquad r = 0.155 .$$

As can be seen from these results, both the mean squared differences and correlation coefficients differ between the two cases significantly. Thus, chosen estimates for changes in multiplicative or additive constituents of model (10.1.2) caused by the presence of a defect in a tested specimen (if such changes exist) can serve as suitable criteria for making conclusions on the presence of defects in tested specimens.

As noted above, in the case of sensor Ug2_2, vectors $\mathbf{a}^{ref}$ and $\mathbf{b}^{ref}$ turned out to be scalars, i.e., constants. Vectors $\mathbf{a}$ and $\mathbf{b}$ also proved to be scalars for the data obtained while testing both flawless and defected specimens. That is, here we deal exclusively with a change in the vector of the periodic constituent $\mathbf{f}(t)$, more exactly, with a change in its harmonic magnitudes. Therefore, to conclude about the presence of a defect in this case, it is enough to consider only a change in these magnitudes compared to those of the reference vector $\mathbf{f}^{ref}(t)$. An estimator K introduced in section 10.2.3 for quantitative estimation of changes in the spectral content of vector

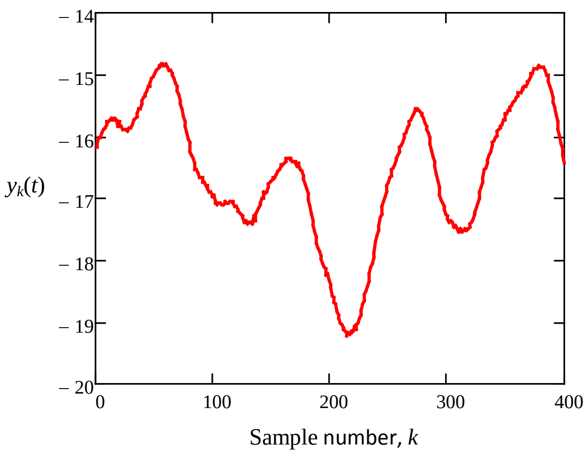

Fig. 10.3.7. Components of a single TIRUS output vector $\mathbf{y}(t)$ obtained while testing a defected specimen. The device under test is Ug2.

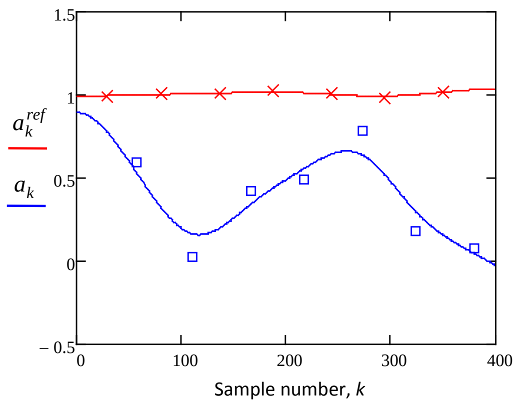

Fig. 10.3.8. Components of multiplicative constituents of data obtained with sensor Ug2. A flawless (a_k^{ref}) and a defected (a_k) specimen were tested.

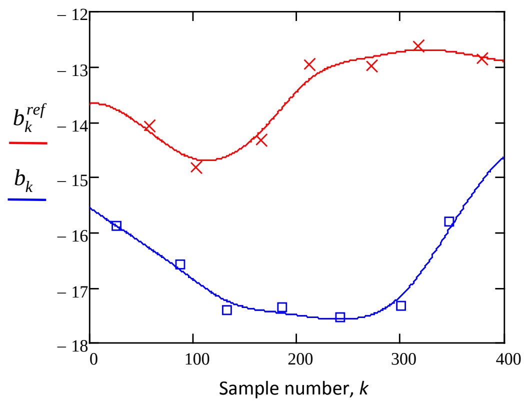

Fig. 10.3.9. Components of additive constituents of data obtained with sensor Ug2. A flawless (b_k^{ref}) and a defected (b_k) specimen were tested.

f(t) caused by the presence of defects in a tested specimen is based just on this notion. Let it be further called the energy deviation coefficient (EDC).

Results of calculations of EDC for a number of trial tests carried out with sensors Ug2 and Ug2_2 are presented in Table 10.3.1. The tests with Ug2 were performed in an open manner, i.e. a manner where the presence or absence of the defects in tested specimens was known in advance. On the contrary, tests with the Ug2_2 sensor were performed in a blind manner, where the raw data were processed with no a priori information on details of the testing procedure and the character of data acquired. In all cases, a critical value K_0 of the EDC was calculated that then was used as a threshold to make a judgment on whether a specimen tested with the sensor was a flawless or defected one. It was defined as defected if a calculated value of EDC K exceeded the K_0 value. The critical values K_0 were defined and calculated as averages of raw series of experimental data sets obtained while testing the sensors themselves with no specimens being in contact with them.

Table 10.3.1. Results of an analysis of data collected in testing procedures.

Data set #	Sensor	Energy deviation coefficient K / K_0 value	Conclusion on the presence of a defect	Tested specimen	Testing conditions
1	Ug2	0.346 / 0.15	Yes	DE1 [1)]	Open manner [2)]
2	Ug2_2	0.277 / 0.35	No	Flawless	Blind
3	Ug2_2	0.232 / 0.35	No	No	Blind
4	Ug2_2	0.586 / 0.35	Yes	Lacquer [3)]	Blind
5	Ug2_2	0.188 / 0.35	No	No	Blind
6	Ug2_2	0.605 / 0.35	**Yes**	Flawless	Blind
7	Ug2_2	0.768 / 0.35	Yes	DE1	Blind
8	Ug2_2	0.619 / 0.35	**Yes**	Flawless	Blind
9	Ug2_2	0.613 / 0.35	Yes	DE1	Blind
10	Ug2_2	0.509 / 0.35	Yes	DE1	Blind

[1)] The tested specimen with a defect of a “subsurface epoxy layer” type.
[2)] Testing conditions are known in advance.
[3)] No tested specimen, protective lacquer is spread on the sensitive surface.

As can be seen from Table 10.3.1, in the majority of cases the developed estimation procedure lead to the right conclusions on the presence of a defect in the tested specimens. Only in two cases out of ten, the conclusions were wrong (rows 6 and 8) and in both cases the calculated *K* values were close. At the moment, it is difficult to suggest an explanation to this fact and there should be done a lot of additional investigations to find the reasons for that. On the whole, however, the result obtained at this stage can be considered satisfactory.

Conclusions

A mathematical model is developed to describe an unstable character of the TIRUS output. A correspondingly developed procedure using this model has proved to be suitable for extraction of distinctive features of the examined TIRUS samples by means of post-processing of raw datasets obtained from them. It is based on the discrete Fourier transform (DFT) of the output and exploits a few first Fourier components to construct specific key features representing the TIRUS itself to be used as a reference in testing procedures for detection of subsurface flaws. The PCA is used as an instrument to prepare an input for the DFT at the first stage of the post-processing procedure. A quantitative estimator built on the base of the developed procedure has demonstrated a rather high probability (~80%) of detecting subsurface defects when being tested on defective and flawless specimens. Despite the fact that the developed technique has produced encouraging results, it should be tested on a greater number of experimental TIRUS samples because in the current project it was verified only on two ones.

11 Results and Discussion

In the course of the project, very different tasks were solved and therefore the types of results obtained are very different as well. Experimental results concerning characteristics of the TIRUS as a two-port network are obtained in investigations described in sections 3-7. They are closely connected with results of optical visualization of ultrasonic beams in the TIRUS body (section 8) that uncover real features of the beams affecting TIRUS operational functionality. A procedure for 3D modeling of ultrasonic beams developed in section 9 provides a calculation instrument for obtaining quantitative results on diffraction losses in the TIRUS and for simulation of transmission, propagation and reflection of ultrasonic beams in an anisotropic medium. A mathematical model developed in section 10 proved to be effective enough to be applied to unstable data obtained from the TIRUS when testing specimens with subsurface defects. All these results having little in common at a glance constitute, in fact, results of a complex research into underlying physics of the TIRUS. Further, they are considered with reference to the objectives of the project.

11.1 Optical Visualization

In the current project, optical visualization of ultrasonic beams has been a valuable instrument for experimental study of their behavior in the TIRUS body. A visualization technique based on isotropic acousto-optic diffraction was applied to observe shear waves polarized along the $[1\bar{1}0]$ direction and propagating in the [110] and [001] directions illuminated from the “forbidden” $[1\bar{1}0]$ direction. In this case, an effective photoelastic constants p_{eff}=0 for both waves (see eq. (8.1.2) in section 8.1) and the observed waves become “theoretically invisible”. In practice, however, a very weak responses from these waves can be observed and optical images of waves of interest have been recorded in the visualization experiments. It is worth mentioning that a mere fact of visualization of the field structure of an “invisible wave” (Fig. 8.4.2) under such conditions is a pioneering result in itself. Concrete results obtained are discussed in the relevant parts of the following subsections, particularly in 11.4 and 11.5.

11.2 Insertion Losses and Spurious Signals

Data obtained in measurements of insertion losses of experimental samples are collected in Table 1.1.1 on the next page. They were acquired in both continuous wave and time-gated experiments, in the temperature controllable environment at 20°C and under ordinary laboratory conditions when temperature could change within 8-10°C. Although some data collected are controversial, e.g. those marked with dark-grey in row 2, this does not change common results following from data analysis.

An obvious result obtained from an analysis of these data is that measured insertion losses of the TIRUS samples are certainly greater than those of the “Loss Samples”. The difference is significant, of the order of 6-8 dB, and is observed for all experimental samples with no exclusion. Therefore, a natural conclusion to be drawn from this at a glance is that the main reason for an unexpectedly large insertion loss of the TIRUS is the presence of an inclined reflecting surface in its design (see Fig. 2.2.1). That is, it looks like the slow shear wave emitted by the transducer into the [110] direction of the TeO_2 crystal does lose energy on reflection from this surface, which might be a result of acoustic mode conversion on the reflection. However, optical visualization of propagation and reflection of ultrasonic pulses in the crystal has shown that no conversion is observed. Moreover, the calculated value of the diffraction loss in the TIRUS (row 4 in Table 11.1.1) taking into account a bro-

Table 11.1.1. Insertion losses of experimental samples

No	Results on	Data obtained for sample:
1	TIRUS, $\|IL(f)\|$ in the 50 kHz range around 27 MHz, dB.	Ug2: 13.2-17.6 [1]; Ug2[1)]: 11-17, Fig. 6.2.6; Ug2_2[1)]: 13-18, Fig. 6.2.8; Uj4[1)]: 11-23, Fig. 6.2.3.
2	TIRUS, $\|IL_{TG}\|$ at 27 MHz, dB.	Ug2_2[1)]: 14.1, Table 6.3.1; Uj4: 14.7±0.2, Fig. 4.2.2; Uj4: 13.8, Table 6.3.1.
3	TIRUS, Reflection loss at 27 MHz, dB.	Uj4: 0.7, Fig. 3.2.5
4	TIRUS, Diffraction loss at 27 MHZ, dB, calculated.	2.64±0.12, section 9.5 and Fig. 9.4.6.
5	Loss samples, $\|IL(f)\|$, dB, measured at 27 MHz.	Uj1: 5.7±1.0, Fig. 3.1.3; Uj2: 7.7±2.6, Fig. 3.1.3.
6	Loss samples, $\|IL_{TG}\|$, dB, measured at 27 MHz.	Uj1: 7.7±0.1, Fig. 4.1.1; Uj2: 7.2±0.1, Fig. 4.1.1.

[1)] at 20±0.1°C.

ken (polygonal) propagation path of the ultrasonic beam because of the reflection from the inclined face of the crystal proved to be too small (2.6 dB) to be a reason for that. Thus, this "jumped conclusion" is hardy correct and some other physical mechanism is responsible for the increase.

As far as the TIRUS design differs from that of the loss samples (see Fig. 2.3.1), apart from the presence of the inclined reflecting plane, only by the transducer on the top face of the TIRUS crystal, it makes one think that this can be a reason. So the real difference is that the normal to the receiving transducer in the loss samples is oriented along the [110] direction whereas in the TIRUS it is orients along the [001] one, which can be the reason for a change in the transducer transduction loss. The transduction loss is a sum of reflection losses at the electrical and acoustic sides of the transducer and dissipative losses at both sides and inside. Because dissipative losses of transducers in the TIRUS and loss samples are certainly very close in values, the only visible physical mechanisms responsible for the discussed increase in total losses is reflection at an electrical or an acoustic side or both. A measured value of reflection loss at electrical side is too small (0.7 dB, row 3 in Table 11.1.1) to really affect total losses hence the only mechanism to be considered is reflection at the acoustic side.

One more important factor that can play a role in the transduction process is a significant narrowing of the ultrasonic beam propagating in the [001] direction after reflection from the inclined face of the crystal. As a result, the size of the receiving transducer on the top of the crystal is much greater than the size of the ultrasonic beam[1]. It raises a question of how these mismatched sizes can affect the transduction loss. Answering this question requires a special research that is out of the scope of the project.

As shown in section 8.4.2, appearance of "satellite pulses" in the TIRUS body and spurious pulse trains at its output (Fig. 4.2.1) are also explained by a mismatched size of the receiving transducer in the fabricated TIRUS sample (Fig. 8.4.4 (*b*)). Thus, a requirement of matching sizes of the transducers and ultrasonic beams is of great importance in the TIRUS design.

Spurious longitudinal ultrasonic waves observed in optical visualization experiments (Fig. 8.4.4 (*a*)) is a simple corollary of the use of a 163° Y-cut $LiNbO_3$ plate as a shear wave transducer because it generates not a pure transverse mode but a quasi-shear one having a longitudinal displacement component. Although the excited longitudinal wave is very weak, less than -26 dB compared to the shear one, a transducer generating a pure shear wave should be used if one needs a greater dynamic range.

[1] It is important to note here that it is not exactly so for TIRUS samples Ug2 and Ug2_2 where the top transducer is almost twice less in size than that in Uj4.

11.3 Instability of the TIRUS Output

Instability of the TIRUS output is a serious problem for its applicability in practice. Investigations of the TIRUS in a temperature controllable environment using a temperature chamber have shown (Figs. 6.2.3 and 6.2.4) that this instability is connected with temperature effects, first of all, as shown in [1], with a strong dependence of the SSW velocity on temperature. The reason for this instability is a change in a resonance frequency of the acoustic resonator, which is the TeO_2 crystal. Therefore, if the TIRUS is driven with a CW signal the change in the resonance frequency results in a change in its insertion loss $IL(f)$. On the contrary, in the time-gated measurements acoustic resonances are absent because the driving pulse is shorter than a propagation time of the SSW along the crystal and the insertion loss IL_{TG} remains steady. Phase parts of the TIRUS output react to change in a temperature similarly in both cases.

As far as the observed instability in the case of CW measurements manifests itself as a shift along the frequency scale of the TIRUS frequency response as a whole, its negative effect can be mitigated by post-processing of experimental data. A corresponding procedure is developed in section 10.

11.4 Acoustic Mode Conversion

Conversion of an emitted SSW into other acoustic modes on reflection from the inclined face of the crystal was supposed [1] to be a possible reason for observed appearance of quasi-longitudinal (QL) and quasi-shear fast (QSF) waves. In the current research, visualization of an ultrasonic shear wave of the SH type has shown (sections 8.4.3 and 8.4.4) that there is no conversion of it on reflection from this face. The same conclusion has been drawn in section 9.5 from calculation results. Thus, the most probable reason for the observed QL and QSF modes is conversion of the spurious longitudinal waves emitted by the shear wave transducer. The observed stronger intensities of optical responses from QL and QSF waves than those from the excited shear waves are explained by a simple fact that the shear wave of interest is visualized by illumination from a “forbidden direction” and therefore a response from it is much weaker.

At the same time, *an analysis of optical visualization data has revealed an unexpected conversion of the shear horizontal wave radiated by the top transducer into a longitudinal one on its normal reflection from the (001) face of the crystal (section 8.4.3), which is inexplicable as far as the plane wave theory is concerned.* It can be thought that a possible reason for the observed phenomenon might be conversion of some plane-wave spectral components of the incident ultrasonic beam that propagate close to the [001] direction. For the time being, however, this is not more than an assumption therefore further research is necessary including both an experimental confirmation of the observed phenomenon and a theoretical analysis of spatial properties of the incident ultrasonic beam including calculation of 3D angular spectra of its wave and ray vectors.

11.5 Displacement of an Ultrasonic Beam

Optical visualisation of reflection of the SH-wave type pulse from the inclined face of the crystal has revealed a displacement of an ultrasonic beam on reflection (Fig. 8.4.5). Although such a phenomenon is widely known, it has never been observed on reflection from a free flat surface that takes place in the described experiment; therefore *this finding is of great importance*. For the time being, there is no satisfactory explanation of the observed phenomenon. Anyway, it requires further experimental studies to be confirmed.

The observed displacement of the ultrasonic beam on reflection might also contribute to the insertion loss of the studied TIRUS samples because in the TIRUS design this effect has not been taken into account and no correction of the transducers location has been done. How much loss is added due to this mechanism should be clarified in a specific research.

11.6 TIRUS as a Testing Instrument

First experiments demonstrating the TIRUS capability to detect a *subsurfac*e flaw is described in section 5. It has been shown that the insertion loss of the TIRUS increases significantly and the "waves" on its frequency response due to acoustic resonance of the crystal are suppressed when its sensitive surface is in contact with a tested specimen having a subsurface defect. The observed effects are the consequence of frustrated total internal reflection of the probing ultrasonic wave caused by a subsurface defect. In the experiment, it was an artificial defect, which was an epoxy layer of 28 µm in thickness under a 90 µm plate of fused quartz. The tested specimen was put in contact with the sensor using an optical contact technique.

Afterwards (sections 6) similar effects were observed invariably in experiments with three different TIRUS samples with no exclusion and with another defective specimen of the same "foreign inclusion type" in both the temperature controllable environment and under normal laboratory conditions, using both the continuous wave and time-gated techniques. In this case, another specimen was used in testing and the defect was an epoxy layer of 53 µm in thickness under a 60 µm plate of fused quartz. *This proves the TIRUS capability of sensing subsurface defects unambiguously*. In the most cases, the degree of the insertion loss increase because of the presence of a defect was significant, up to 7-9 dB (Table 6.3.1), that says about a high potential sensitivity of the sensor. It was also established in the experiments that its sensitivity is high enough to monitor aging of an optical contact (Figs. 6.2.1, 6.2.2, 6.3.3).

Special research into the testing procedure using a couplant between surfaces of the sensor and a tested object produced contradictory results. In the CW experiments, no meaningful change in the TIRUS response was detected when it moved across either a defective or a flawless part of the tested specimen (Fig. 7.2.1). With glycerin as a couplant, there was no reaction at all. With the Sonotech Shear Gel® there was no meaningful reaction as well, only common increase in the insertion loss was observed across all the surface of the tested specimen. On the contrary, in the time-gated experiments a response from the TIRUS was evident and unambiguous: insertion losses IL_{TG} in the defective area were by 10 dB greater than those in the flawless ones (Fig. 7.3.1). A similar reaction was observed in the phase channel as well. On the whole, results of the CW experiments show that the use of the Sonotech Shear Gel at the frequency of 27 MHz is fruitless and some positive results can be expected only at much lower frequencies, of the order of 5-10 MHz, whereas in the time-gated experiments positive results have been already obtained at the frequency of 27 MHz. The contradiction in the results obtained can at the moment be explained in different ways but it is obvious that only further experiments can lead to a proper answer for the reason for it.

11.7 Modeling of Ultrasonic Beams

Modeling of acoustic beams in the TIRUS has been an essential part of the project because not having an adequate model it is not possible, first, to calculate diffraction losses contributing to the total insertion loss of the TIRUS and, second, to have an estimation instrument for analysis of experimental results and comparison of them with the theory. The model and calculation technique developed in the project were verified by comparing calculation results with those known from literature (Figs.9.4.1-9.4.4)

It is worth noting that an implicit underlying assumption made initially that a real 3D structure of an ultrasonic beam could have been recovered from its 2D image projected onto the plane of observation proved to be overly simplistic to be realized in the frame of the current project. Nevertheless, it is obvious that spatial domains in the crystal with zero sound amplitude contribute nothing to recorded images and domains with small amplitudes contribute less than those with greater ones. Hence, some spatial structure of the ultrasonic beam can be revealed and the developed model is of help in establishing correlation between a real 3D distribution of an acoustic field in the crystal and its 2D image visualized in optical experiments. An illustration of this is demonstrated in Fig. 9.3.2.

11.8 Extraction of Reference Data from an Unstable TIRUS Output

In practice, applicability of the TIRUS as a sensor is determined by repeatability of data acquired from its output, which in reality is essentially unstable (Figs. 3.2.7, 6.2.4, 10.3.1) because of its strong dependence on temperature. Therefore, development of an approach to extraction of “reference data” that data acquired can be compared to is of importance. The idea behind the developed approach is to use an intrinsic periodicity of the TIRUS insertion loss frequency response from which a model can be built to extract essential features of this periodicity independent on external random factors (temperature) making the TIRUS output unstable. As a result, an estimator (eq. 10.2.6) has been built enabling to come to a decision on presence of a defect in the tested specimen on the base of a single individual measurement. Having been implemented into the testing procedure, it has shown a rather high probability of correct detection of a subsurface defect (Table 10.3.1).

Conclusions

The complex research into physical mechanisms underlying functionality of the Total Internal Reflection Ultrasonic Sensor (TIRUS) has been carried out. Both theoretical researches and experimental studies have produced a lot of interrelated data to be analyzed. The first includes building of models for simulation of ultrasonic beams and for post-processing of an unstable sensor output, the second embrace visualization of ultrasonic beams and investigations of the TIRUS operational characteristics.

An optical setup has been built allowing shear wave beams in the sensor body, which is a strongly anisotropic TeO_2 crystal, to be visualized while observed from the “forbidden” $[1\bar{1}0]$ direction. The field distribution of shear waves emitted by the transducer polarized along the same $[1\bar{1}0]$ direction and propagating in the [110] and [001] directions have been observed and recorded for the first time. Spurious ultrasonic pulses caused by imperfection of the TIRUS design were visualized that explained appearance of spurious pulse trains at the TIRUS output. Spurious radiation of a longitudinal wave emitted by a 163° Y-cut $LiNbO_3$ shear wave transducer was observed too. Although its intensity was estimated to be at least 26 dB less than that of the shear one, it could apparently be the reason for the QL and QSF waves observed in optical experiments in [1] because their effective photoelastic coefficients are much greater than that of the SSW. At the same time, there has been observed no direct conversion of the emitted shear wave into a longitudinal one on its reflection from the (110) 16.25° z-rotated surface of the crystal.

However, *two effects that have apparently never been observed before* have been discovered, *a displace-*

ment of an ultrasonic beam on its reflection from a free flat surface and conversion *of a shear-horizontal wave incident normally on the reflecting (001) face of the crystal into a longitudinal one*. These findings are the most important results obtained in optical visualization experiments. Therefore, the observed phenomena require further research into their nature including both experimental studies and a theoretical analysis of spatial properties of incident ultrasonic beams including calculation of their angular spectra to be verified and confirmed.

Comparative analysis of results obtained for two types of experimental samples, one having an inclined surface changing the ultrasonic beam propagation direction from [110] to [001] ("TIRUS samples") and another without it ("Loss samples"), has shown that the insertion losses of the former (~13-14 dB) is by 6-8 dB greater than those of the latter (~7-8 dB). This difference cannot be explained by the presence of the inclined reflecting plane because (1) the diffraction loss computed across the whole beam path using the developed calculation technique does not exceed 2.76 dB and (2) no conversion of the probing SSW on its reflection from the reflecting plane has been discovered in optical visualization experiments. Thus, an increase in the total insertion losses in the TIRUS samples compared to those in the Loss samples should be referred to the transduction losses of the transducer on the top surface of the crystal because in the loss samples such transducers are absent. At the same time, additional loss due to the displacement of an ultrasonic beam on its reflection from the inclined surface might also be significant.

Results of measurement of the insertion losses of the TIRUS samples in the temperature controllable environment have convincingly confirmed an assumption that the observed instability of the TIRUS CW output is completely connected with temperature influences on the resonance properties of the crystal. Therefore, in the NDT practice, a measurement system based on the time-gated technique is more preferable in most cases. At the same time, the CW technique can be more sensitive since resonance properties of the crystal changing because of frustrated total internal reflection may play a role of an informative factor. However, it requires the use of the developed post-processing procedure for extraction of proper information from an unstable TIRUS output. This procedure, although has been proved to be rather effective, was tested only on two TIRUS samples with significantly different characteristics and therefore needs itself further verification.

Testing defective and flawless specimens using optical contact technique has shown 100% detection of defects of a "foreign inclusion" type. The defects were thin (28 and 53 μm) epoxy layers under plates of fused quartz of 90 and 60 μm in thickness respectively. Thus, the TIRUS capability to detect *subsurface* inhomogeneities has been proved conclusively.

Testing a defective specimen with a TIRUS through a couplant has led to discrepancy in the results obtained. In the CW experiments no response from a defect was detected whereas in the time-gated experiments the insertion loss of the TIRUS grew by ~10 dB when the TIRUS passed through the defective area of the specimen that was an unambiguous indicator of the detected defect. Further thorough experiments are necessary to explain such a difference in results.

The accomplishment of the research has shown that:

– acousto-optic interaction "forbidden" theoretically can, in practice, be used to visualize spatial structure of ultrasonic beams;

– the TIRUS does sense *subsurface* defects, at least defects of a "foreign inclusion type", when its sensitive surface is in direct contact with a tested specimen. Its operational capability in the case of a couplant between those has to be proved yet;

- there is no conversion of a probing SSW into a longitudinal one on its reflection from the inclined surface of the crystal. Visualized QL and QSF acoustic waves are most probably caused by conversion of a spurious longitudinal wave emitted by the shear wave transducer;
- spurious pulse trains at the TIRUS output are caused by imperfection of the TIRUS design;
- large insertion loss of the TIRUS is not connected with conversion of a probing shear wave into other acoustic modes. Most probably they are determined by large transduction loss of the transducer located on the (001) surface of the crystal that requires special investigations. Additional loss due to the displacement of an ultrasonic beam might also be significant and should be studied;
- instability of the TIRUS output is caused exclusively by temperature influences;
- information on the presence of a defect in a tested specimen can be extracted from the unstable TIRUS output by means of post-processing of the output data;
- the plane wave decomposition of the surface displacement field in the restricted plane area together with the use of the Stroh formalism is an effective instrument for modeling transmission, propagation and reflection of bulk shear ultrasonic waves in anisotropic media;
- special researches are necessary to confirm two discovered effects, a displacement of an ultrasonic beam on its reflection from a free flat surface and conversion of a shear-horizontal wave incident normally on the reflecting (001) face of the crystal into a longitudinal one.

Acknowledgments

The authors are particularly grateful to Lt Col Randall Pollak and Maj Matthew Snyder of the EOARD who made it possible to discuss our most interesting research results at two conferences, 2013 IEEE Joint UFFC, EFTF and PFM Symposium and 2014 IEEE International Ultrasonics Symposium.

Appendix A. Development of a Phase Meter for Time-Gated Measurements

A.1 Time-Gated Measurement of a Transfer Function

An obvious way to avoid acoustic resonances in the sensor body is to apply pulse signals of duration less than the propagation time of ultrasonic waves between input and output transducers. In the current project, the sine burst waveforms, which are rectangular pulses with the continuous wave carrier of 27 MHz, are used for this purpose. Comparing parameters of the input and output signals of the sensor, one can detect a change in its output caused by a subsurface flaw to be detected with the sensor.

In the course of the work, a specific phase meter has been developed and built to realize such a procedure. It consists of the driving and measurement parts working together and provides comparison of both main parameters of the driving waveforms, the phase of the carrier and the amplitude of the pulse envelope.

The driving part of the phase meter is based on the programmed logic device Altera EPM7128SQC100 and has an interface to a personal computer. The controlling software allows to control the pulse duration, repetition rate and provides measurements of the phase of the carrier at the specified time points relative to that of the generated pulses. The driving part itself is depicted in Fig. A.1.

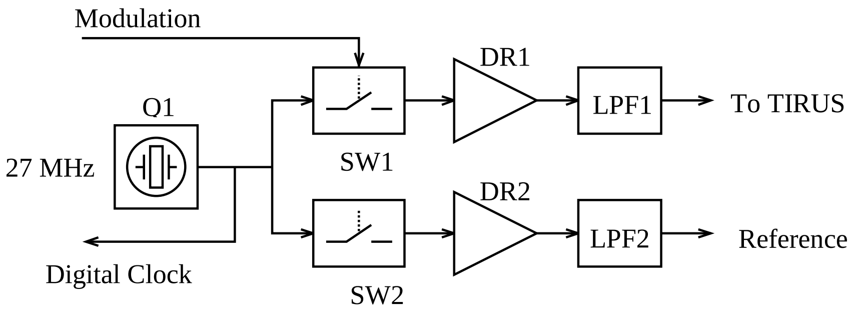

Fig. A.1. Block diagram of a driving part of the phase meter.

The carrier frequency of 27 MHz is generated by a programmable quartz oscillator Q1, which has the temperature stability 50 ppm/K. This frequency is applied to the fast switches SW1 and SW2. The switch SW1 is used to form a pulse of programmed duration and is controlled by the modulation signals from the controller board in a computer. Another switch SW2 included into the circuitry is meant to compensate a time delay and is always on. The frequency from Q1 is also used to clock the digital logic of the controller board to make all the modulation signals synchronous. Two outputs of the driver are driven by the amplifiers DR1 and DR2 with nominal output power of 5 dBm. The amplifiers are connected to the outputs via low-pass filters LPF1 and LPF2 with a cut-off frequency of 30 MHz. One of the outputs is applied directly to the TIRUS transducer, and another one is used as a reference channel for the measuring part of the phase meter, a phase detector.

A.2 Principle of Operation of the Phase Detector

The developed phase detector measures both the phase of the carrier of the TIRUS output relative to the reference signal and its strength. The strength is determined as logarithm of the signal amplitude that provides a high dynamic range of the measurement system. The outputs of the phase detector are converted into digital form and acquired by a personal computer. The diagram of the phase detector is shown in Fig. A.2.

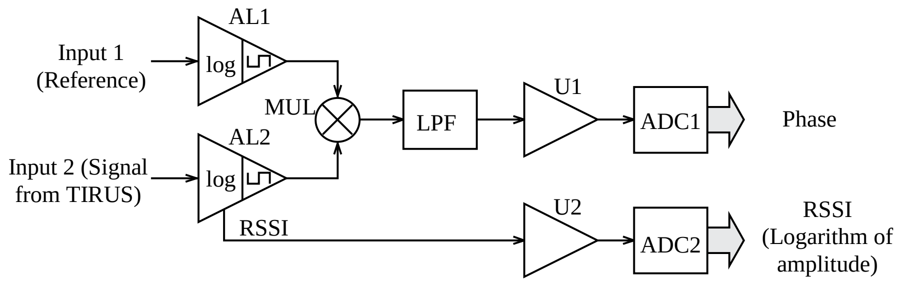

Fig. A.2. Block diagram of the phase detector.

It has two inputs, one for the reference frequency and another for the input signal. There are two identical logarithmic amplifiers AL1 and AL2 at the both inputs. Logarithmic amplifiers have limiters at their outputs and convert sine inputs into square waves. A special integrated circuit AD606 is used to build the device, which guarantees that the phase of an output square wave does not shift relative to the input signal phase. The phase difference between input signals is detected in the same manner as in analog electronics – the waves after the limiters are multiplied with the analog multiplier MUL. Voltage at the output of the low-pass filter LPF is proportional to the phase shift between the input signals. It is scaled by an amplifier U1 and sampled by the computer-controlled analog-to-digital converter ADC1. The logarithmic amplifier AL2 provides an additional output RSSI. Voltage at this output is proportional to the logarithm of the input signal amplitude. The RSSI signal is sampled by the second converter ADC2, so both the phase and the amplitude of the input 2 are acquired by the controlling computer.

A.3 Calibration of the Phase Detector

Linearity of the phase detector was checked by means of two different procedures. In the first case, the reference input was driven by the CW signal of 27 MHz and the signal input was driven by the slightly different frequency of 27.000000047 MHz. Due to the difference in frequencies, the phase between these signals changed linearly in time; the speed of this change was 16.76 degrees per second. Both the signals were generated by the computer-controlled two-channel frequency synthesizer built on the base of the Analog Devices integrated circuit AD9959. Both channels of the synthesizer were fed by the common clock signal of 200 MHz and were fully synchronized. The only factor affecting the stability of the frequencies was the stability of the clock generator. The clock generator was built on the VX7 module by Jauch Quartz GmbH, which had the temperature stability $2\cdot10^{-6}$ $Hz\cdot K^{-1}$. This led to instability of the calibration line slope of the order of 1 arcssec/s·K, which is negligible for the performed measurements. The speed of the phase difference change of 16.76°/s corresponds to the minimal frequency difference of 0.047 Hz allowed to be set with the used synthesizers.

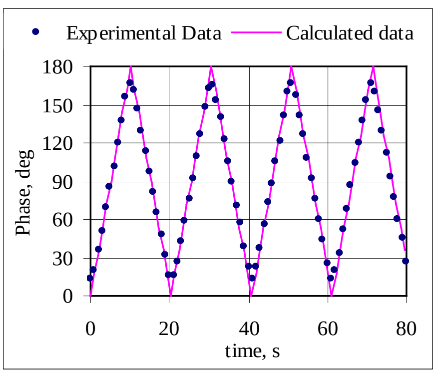

Fig. A.3. Calibration: the phase difference measured. The speed of the phase change is 16.76°/s.

The results of the phase measurements in the first calibration procedure are shown in Fig. A.3. Analysis of the obtained curve confirms that the examined detector has a high linearity region for values of the phase between 30° and 150°. A measured speed of the phase change was (16.89±0.17)°/s (averaged over the 8 linear sections). This is in a good agreement with the expected (calculated) value of the speed. The presence of nonlinear regions is due to a limited slew rate of the square waves which are applied to the analog multiplier device MUL.

The second calibration procedure was performed with the frequency of 27 MHz at both inputs with the simultaneous phase shift between the inputs. The test signals were generated by a two-channel synthesizer with a phase shift introduced into one of the channels. The synthesizer allowed to control the phase in each of the channels with great precision. At the same time, some constant phase shift between the channels appeared because of the delay of the signals in the analog circuitry. This unknown phase shift was compensated before applying the testing procedure to the phase detector. The phase of the reference signal was adjusted to match the second channel with a relative precision of 1-2% using an averaging procedure with the oscilloscope Tektronix TDS 201. After such a compensation the initial phase shift was assumed to be zero. A testing phase shift was introduced into the signal channel with a step of 5°. A starting phase value was assigned to be 90°, which is the center of the linear region of the phase detector. Calibration of the phase detector was performed by adjusting a scaling amplifier U1. After calibration, the output of the phase detector was in a good agreement with the phase difference set at the synthesizer output. The usable working range was 30÷150°, corresponding to the linear region of the phase detector. A drawing of the calibration curve is shown in Fig. A.4. The red line corresponds to a linear regression of the acquired data with a maximum deviation from the linear up to 2°.

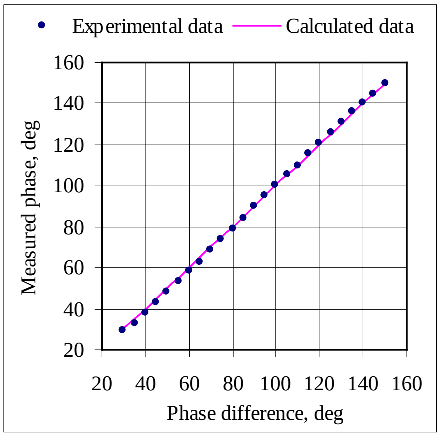

Fig. A.4. The calibration curve of the phase detector.

In addition to the applied calibration procedures, the long-term stability of the phase detector was also investigated. Experimental data show that after a 20-minute warming the subsequent drift of measured values was less than 1°/hour.

To check operation of the phase meter with pulse signals (sine wave bursts), measurements of the output transient time were performed. The input signal was modulated to get short sine burst waveforms by switching the synthesizer on and off with a timed controller. To determine a rise time, the measurements were started with the specified delay relative to the pulse beginning. A correct value of the phase appeared at the digital output of the phase detector only when a sample was taken at the time point set up at least 1μs after the pulse started and not more than 1μs before it finished. This demonstrates that the transient time of the phase detector including the measurement delay in its circuitry is of the order of 2 μs. The stability of phase measurements within this allowed interval of the pulse duration was about 1°.

The amplitude measurement channel (RSSI) allows estimation of the signal strength with precision of 0.1 dB. It was calibrated to represent the value of 0 dB when the external synthesizer output was connected directly to the input of the phase meter.

A.4 Testing of the Phase Meter Using an Ultrasonic Delay Line

All testing and calibration procedures in the previous section were performed almost in “virtual measurement environment” when there was no significant delay between the reference and measured signals. In reality, measurements are to be done with sine burst waveforms separated in time by tens microseconds. To test the phase meter in “real measurement environment” a special ultrasonic delay line (UDL) was developed and fabricated.

The requirements to the developed UDL were as follows. Firstly, it had to provide the delay time not less than 10 μs to operate reliably with pulses of 5 μs duration. Secondly, it had to have temperature stability good enough to not change its delay parameters at small temperature changes in ordinary laboratory environment. These requirements could be satisfied with fused quartz used as a UDL waveguide. It has an extremely small coefficient of thermal expansion $\alpha=5.5\times10^{-7}$ K^{-1} and small enough temperature coefficient of sound velocity equal to 1.1×10^{-4} K^{-1} for shear wave [50, p. 960]. Such a delay line was fabricated using a bar of fused quartz of 43.3 mm in length. The shear wave velocity in fused quartz is 3750 m/s, which with such a length of the UDL body provides delay of 11.6 μs. Two shear-wave transducers with resonance frequencies of 27 MHz were bonded to its opposite faces using technology of diffusion vacuum welding. Calculations made with the indicated values of temperature coefficients and the UDL body length gave dependence of the phase shift in the UDL of the order of $11°\cdot K^{-1}$.

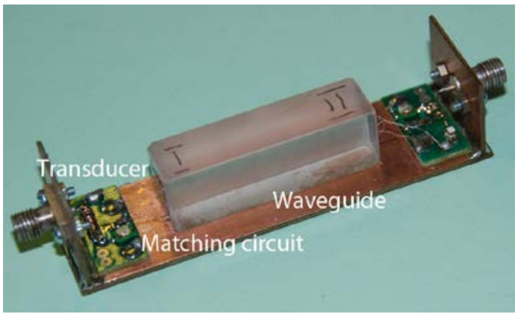

Fig. A.5. Appearance of an ultrasonic delay line fabricated for testing the phase meter.

The appearance of the fabricated UDL is shown in Fig. A.5. It was used as a testing device for the developed phase meter. A screenshot from a testing PC in Fig. A.6 represents results of a typical application of the testing procedure. Data displayed in the "Measurement results" window show that the phase meter produces stable enough results in ordinary laboratory environment.

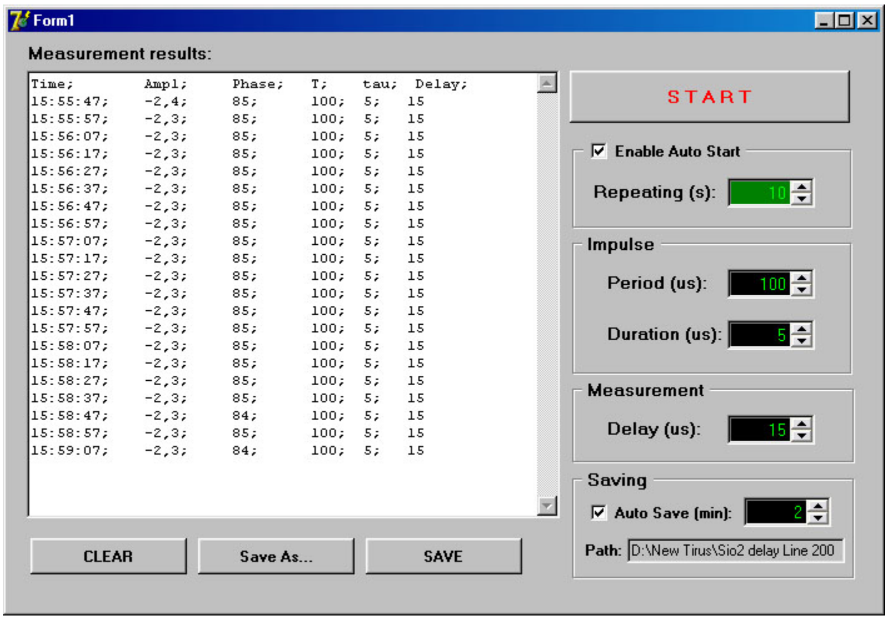

Fig. A.6. The phase meter interface representing measurement results.

References

[1] Project STCU P367-EOARD088002 "Total Internal Reflection Ultrasonic Sensor for Detection of Subsurface Flaws: Proof of Concept." Final Technical Report, Submitted to EOARD on March 31, 2010 http://www.dtic.mil/dtic/tr/fulltext/u2/a527212.pdf, Accessed 02 Oct., 2014.

[2] A. Yurchenko, V. Danilov, Yu. Pilgun, and E. Smirnov, "Detection of a Subsurface Flaw with the Total Internal Reflection Ultrasonic Sensor," 2013 IUS Proceedings of the 2013 Joint UFFC, EFTF and PFM Symposium, pp. 190-193.

[3] L.P. Voitenko, E.M. Smirnov, and A.V. Yurchenko, "Direct Observation of Slow Shear Wave Reflection in the Plane (110) of Paratellurite," Bulletin of Taras Shevchenko National University of Kyiv. Series: Radiophysics & Electronics, no. 11, pp.13-16, 2008 (in Ukrainian).

[4] Y. Ohmachi and N. Uchida, "Temperature Dependence of Elastic, Dielectric, and Piezoelectric Constants in TeO2 Single Crystals," J. Appl. Phys., vol. 41, no. 6, May 1970, pp. 2307–2311.

[5] D. Royer and E. Dieulesaint, Elastic Waves in Solids I: Free and Guided Propagation. Berlin: Springer, 2000.

[6] M. Consonni, Chen Fun Wee, and C. Schneider, "Manufacturing of welded joints with realistic defects," NDT 2011 - 50th annual conference of the British Institute of Non-Destructive Testing, 13-15 Sept. 2011. Telford, UK. http://www.twi-global.com/technical-knowledge/published-papers/manufacturing-of-welded-joints-with-realistic-defects/, Accessed 04 Oct., 2014.

[7] Ginzton E. L., Microwave measurements. McGraw-Hill Book Company, Inc., 1957.

[8] D. Royer and E. Dieulesaint, Elastic Waves in Solids II: Generation, Acousto-optic Interaction, Applications. Berlin: Springer, 2000.

[9] M.A. Breazeale, "From monochromatic light diffraction to colour schlieren photography," J. Opt. A: Pure Appl. Opt., vol. 3, no. 4, pp. S1-S7, 2001.

[10] T. Neumann and H. Ermert, "Schlieren visualization of ultrasonic wave fields with high spatial resolution," Ultrasonics, vol. 44, suppl., pp. e1561-e1566, 2006.

[11] C.F. Ying, S.Y. Zhang, and J.Z. Shen, "Scattering of Ultrasound in Solids as Visualized by the Photoelastic Technique," Journal of Nondestructive Evaluation, vol. 4, no. 2, pp. 65-73, 1984.

[12] E. Ginzel, "Photoelastic Visualisation of Ultrasonic Pulse Interactions, Part 2: Horizontally polarised shear mode in a solid," The e-Journal of Nondestructive Testing, vol. 18, no. 01, 4 pp., January 2013.

[13] V.I. Balakshy, V.N. Parygin, L.E. Chirkov, Physical Basics of Acousto-Optics. Moscow: Radio and Communication Publ., 1985 (in Russian).

[14] Yu.S. Dobrolenskiy, V.B. Voloshinov, and V. N. Parygin, "Collinear acousto-optic interaction of divergent beams in paratellurite crystal," Proc. SPIE Vol. 5828, Acousto-Optics and Applications V, pp. 16-24, 3 March 2005.

[15] O. Polishko, E. Smirnov, and A. Yurchenko, "Optical Imaging of Ultrasonic Pulses Using Forbidden Acousto-Optic Interaction," Proceedings of the IX International Conference "Electronics and Applied Physics". – Kyiv, Ukraine, 23-26 October, 2013, p. 19-20.

[16] O. Polishko, A. Yurchenko, Y. Pilgun, and E. Smirnov, "Real-Time Acousto-Optic Visualization of Ultrasonic Pulses in TeO_2," 12th International School on Acousto-Optics and Application. – Druskininkai, Lithuania, 29th June – 3 July, 2014, in press.

[17] A. Yurchenko, O. Polishko, Y. Pilgun, and E. Smirnov, "Visualization of Ultrasonic Pulses in the Total Internal Reflection Ultrasonic Sensor," 2014 IEEE International Ultrasonics Symposium Proceedings, pp. 749-752.

[18] O.Yu. Makarov and V.B. Voloshinov, "Visualization of back reflected acoustic waves in paratellurite single crystals by means of acousto-optics," Proc. of SPIE Vol. 5953, Acousto-optics and Photoacoustics, 59530X, pp. 1-10, 24 September 2005.

[19] N. Uchida, Y. Ohmachi, "Elastic and Photoelastic Properties of TeO_2 Single Crystal," J. Appl. Phys., vol. 40, pp. 4692–95 (1969).

[20] E. D. Guy, S. J. Radzevicius, "SH-wave Intromission Concept", Technical Physics Letters, vol. 30, no. 5, pp. 370–373, 2004.

[21] N.F. Declercq, "On the fascinating phenomenon of diffraction by periodic structures," Acoustics Today, vol. 9, no. 1, pp. 8-13, January 2013.

[22] L.M. Brekhovskikh, Waves in layered media, 2nd ed., New York: Academic Press, 1980.

[23] B. Collet and M. Destrade, "Explicit secular equations for piezoacoustic surface waves: Shear-horizontal modes," J. Acoust. Soc. Am., vol. 116, no. 6, pp. 3432-3442, December 2004.

[24] A.W. Warner, M. Onoe, and G.A. Coquin, "Determination of Elastic and Piezoelectric Constants for Crystals in Class (3m)," J. Acoust. Soc. Am., vol. 42, no. 6, pp. 1223-1231, December 1967.

[25] Review of Progress in Quantitative Nondestructive Evaluation, Vol. 16A, edited by D. O. Thompson and D. E. Chimenti, NY: Plenum Press, 1997.

[26] M. Rudolph. "Ultrasonic beam models in anisotropic media," Ph.D. Thesis, Iowa State University, Ames, Iowa, US, 1999.

[27] M. Spies and R. A. Roberts, “Modeling of transducer fields in weld material: a comparison of three generically different approaches,” in Review of Progress in Quantitative Nondestructive Evaluation, vol. 19, edited by D. O. Thompson and D. E. Chimenti, AIP Conference Proceedings, Volume 509, pp. 961-968, 2000.

[28] M. Spies, “Ultrasonic field modeling for immersed components using Gaussian beam superposition,” Ultrasonics, Vol. 46, No. 2, pp. 138–147, 2007.

[29] S. Marburg, “Discretization Requirements: How many Elements per Wavelength are Necessary?,” in book Computational acoustics of noise propagation in fluids: finite and boundary element methods, edited by Steffen Marburg, Bodo Nolte, Springer, 2008.

[30] T. Kundu, D. Placko, E. K. Rahani, T. Yanagita, and C. M. Dao, “Ultrasonic Field Modeling: A Comparison of Analytical, Semi-Analytical, and Numerical Techniques,” IEEE Transactions on Ultrasonics, Ferroelectrics and Frequency Control, Vol. 57, No. 12, pp. 2795–2807, 2010.

[31] M. Pluta, A. G. Every, W. Grill, and T. J. Kim, “Fourier inversion of acoustic wave fields in anisotropic solids,” Phys. Rev. B, Vol. 67, No. 9, 094117 [9 pages], 2003.

[32] D. J. Vezzetti, “Propagation of bounded ultrasonic beams in anisotropic media,” J. Acoust. Soc. Am., Vol. 78, Iss. 3, pp. 1103–1108, September 1985.

[33] B. E. O’Neill and R. Gr. Maev, “Integral approximation method for calculating ultrasonic beam propagation in anisotropic materials,” Phys. Rev. B, Vol. 58, No. 9, pp. 5479–5485, 1998.

[34] M. Spies, “Transducer-modeling in General Transversely Isotropic Media Via Point-Source-Synthesis: Theory,” Journal of Nondestructive Evaluation, Vol. 13, No. 2, pp. 85–99, 1994.

[35] B. P. Newberry and R. B. Thompson, “A paraxial theory for the propagation of ultrasonic beams in anisotropic solids,” J. Acoust. Soc. Am., Vol. 85, No. 6, pp. 2290–2300, 1989.

[36] C. T. J. Dodson, T. Poston, Tensor Geometry. The Geometric Viewpoint and its Uses, 2-nd edition. Berlin: Springer, 1991.

[37] T. C. T. Ting, Anisotropic Elasticity. Theory and Applications. New York, Oxford: Oxford University Press, 1996.

[38] A. N. Darinskii and G. A. Maugin, “The elastic wave resonance reflection from a thin solid layer in a crystal,” Wave Motion, Vol. 23, Iss. 4, pp. 363–385, June 1996.

[39] R. Truell, C. Elbaum and B. B. Chick. Ultrasonic Methods in Solid State Physics. New York, London: Academic Press, 1969.

[40] H. Seki, A. Granato and R. Truell, “Diffraction Effects in the Ultrasonic Field of a Piston Source and Their Importance in the Accurate Measurement of Attenuation,” J. Acoust. Soc. Am., Vol. 28, Iss. 2, pp. 230–238, March 1956.

[41] E. P. Papadakis, F. Margetan, and B. P. Newberry, “Diffraction loss in the [110] direction in cubic crystals,” J. Acoust. Soc. Am., Vol. 88, Iss. 2, pp. 945–950, August 1990.

[42] D. H. Green and H. F. Wang, “Shear wave diffraction loss for circular plane-polarized source and receiver,” J. Acoust. Soc. Am., Vol. 90, Iss. 5, pp. 2697–2704, November 1991.

[43] Y. Fujii and K. Yamada, “Acoustic Response of a Rectangular Receiver to a Rectangular Source,” J. Acoust. Soc. Am., Vol. 40, Iss. 1, pp. 249–251, 1966.

[44] K. Yamada and Y. Fujii, “Acoustic Response of a Circular Receiver to a Circular Source of Different Radius,” J. Acoust. Soc. Am., Vol. 40, Iss. 5, pp. 1193–1194, 1966.

[45] R. Golinske, M. Hoffmann, A. Gupta, and M. Kupnik, “Calculation of diffraction loss between non-co-axial ultrasonic transducer configurations,” IEEE International Ultrasonics Symposium (IUS), 21–25 July 2013, pp. 2171-2174.

[46] Alex Waibel, Kai-Fu Lee. Readings in Speech Recognition. – Morgan Kaufmann Publishers Inc., 1990 .

[47] NIST/SEMATECH e-Handbook of Statistical Methods, http://www.itl.nist.gov/div898/handbook/, Specifically: http://www.itl.nist.gov/div898/handbook/eda/section3/autocop4.htm, 14 June 2013.

[48] W. L. Briggs, Van E. Henson. The DFT: An Owners Manual for the Discrete Fourier Transform. – SIAM, 1995.

[49] Jolliffe, I. T. Principal component analysis (Second ed.). Springer, 2002.

[50] M. B. Gitis, “Disorder and order in long-wave high-temperature acoustics (II): monatomic liquids,” Sov. Phys. Usp., Vol. 35, No. 11, pp. 956–990, 1992 [Translated from Soviet Physics Uspekhi, Vol. 162, No. 11, pp. 111–181, 1992].

November 24, 2014 Oleksandr (Alexander) Yurchenko